Snapshots of Water

Orientational dynamics of hydrogen-bonded systems

Snapshots of Water

Orientational dynamics of hydrogen-bonded systems

ACADEMISCH PROEFSCHRIFT

ter verkrijging van de graad van doctor
aan de Universiteit van Amsterdam
op gezag van de Rector Magnificus
prof. dr. D. C. van den Boom
ten overstaan van een door het college voor promoties ingestelde
commissie, in het openbaar te verdedigen in de Agnietenkapel
op donderdag 10 januari 2008 te 14.00 uur

door

Yves-Laurent Ariel Rezuş

geboren te Genève, Zwitserland

Promotiecommissie

promotor:	prof. dr. H. J. Bakker
overige leden:	prof. dr. P. G. Bolhuis
	prof. dr. M. Bonn
	prof. dr. D. Frenkel
	prof. dr. J. T. Hynes
	prof. dr. L. D. Noordam
	prof. dr. W. J. van der Zande

Faculteit der Natuurwetenschappen, Wiskunde en Informatica

ISBN 978-90-77209-18-9

The work described in this thesis was performed at the FOM-*Institute for Atomic and Molecular Physics* (AMOLF), Kruislaan 407, 1098 SJ Amsterdam, The Netherlands. The work is part of the research programme of the *Stichting Fundamenteel Onderzoek der Materie* (FOM), which is financially supported by the *Nederlandse Organisatie voor Wetenschappelijk Onderzoek* (NWO).

Cover design: Elsje van Bergen

Pentru Zoia şi Adi
Voor Elsje

Publications covered in this thesis

Y. L. A. Rezus, D. Madsen and H. J. Bakker. Orientational dynamics of hydrogen-bonded phenol. *J. Chem. Phys. 121*, 10599–10604 (2004).

Y. L. A. Rezus and H. J. Bakker. On the orientational relaxation of HDO in liquid water. *J. Chem. Phys. 123*, 114502 (2005).

Y. L. A. Rezus and H. J. Bakker. Orientational dynamics of isotopically diluted H_2O and D_2O. *J. Chem. Phys. 125*, 144512 (2006).

Y. L. A. Rezus and H. J. Bakker. Effect of urea on the structural dynamics of water. *Proc. Natl. Acad. Sci. U.S.A. 103*, 18417-18420 (2006).

Y. L. A. Rezus and H. J. Bakker. Observation of immobilized water molecules around hydrophobic groups. *Phys. Rev. Lett. 99*, 148301 (2007).

Y. L. A. Rezus and H. J. Bakker. Strong slowing down of water reorientation in mixtures of water and tetramethylurea. *Submitted*.

Y. L. A. Rezus and H. J. Bakker. Destabilization of the hydrogen-bond structure of water by the osmolyte trimethylamine-N-oxide. *Submitted*.

Y. L. A. Rezus and H. J. Bakker. Femtosecond spectroscopic study of the solvation of amphiphilic molecules by water. *Submitted*.

Contents

1 Introduction **11**
- 1.1 Liquid water and hydrogen bonds . . . 11
- 1.2 Vibrational spectroscopy . . . 14
  - 1.2.1 Microscopic description: the harmonic oscillator . . . 14
  - 1.2.2 Macroscopic description: Lambert-Beer's law . . . 18
- 1.3 Vibrational pump-probe spectroscopy . . . 20
  - 1.3.1 Vibrational relaxation . . . 21
  - 1.3.2 Inhomogeneous broadening and spectral diffusion . . . 23
  - 1.3.3 Sample heating . . . 24
  - 1.3.4 Artifacts . . . 25
- 1.4 Intermezzo: amplitude of the transient spectrum . . . 28
- 1.5 Polarization properties . . . 30
  - 1.5.1 Isotropic signal . . . 31
  - 1.5.2 Anisotropy . . . 34

2 Nonlinear response theory **37**
- 2.1 Introduction . . . 37
- 2.2 Perturbation expansion of the polarization . . . 37
- 2.3 First order polarization . . . 40
- 2.4 Third order polarization . . . 43
- 2.5 Application to pump-probe spectroscopy . . . 46
  - 2.5.1 Detection . . . 50
- 2.6 Inhomogeneous broadening and spectral diffusion . . . 51

3 Experimental methods **53**
- 3.1 Light generation . . . 53
  - 3.1.1 Physical principle . . . 53
  - 3.1.2 Experimental realization . . . 56
- 3.2 Pump-probe setup . . . 57
- 3.3 Samples: isotopically diluted water . . . 60

4 Orientational dynamics of hydrogen-bonded phenol **61**
- 4.1 Introduction . . . 61
- 4.2 Experimental . . . 62
- 4.3 Results and Discussion . . . 62
- 4.4 Conclusion . . . 70

5 Orientational dynamics of HDO in liquid water 71
5.1 Introduction . . . 71
5.2 Experimental . . . 72
5.3 Results . . . 73
5.4 Discussion . . . 79
5.5 Conclusion . . . 81

6 Vibrational relaxation and orientational dynamics of HDO in heavy water 83
6.1 Introduction . . . 83
6.2 Experimental . . . 84
6.3 Results . . . 84
6.3.1 Vibrational relaxation . . . 84
6.3.2 Anisotropic dynamics . . . 85
6.4 Discussion . . . 94
6.5 Conclusion . . . 96
6.6 Appendix . . . 96
6.6.1 Equations for the orientational dynamics . . . 96

7 The effect of urea on the structural dynamics of water 99
7.1 Introduction . . . 99
7.2 Experimental . . . 100
7.3 Results . . . 100
7.4 Discussion . . . 103
7.5 Conclusions . . . 105

8 Observation of immobilized water molecules around hydrophobic groups 107
8.1 Introduction . . . 107
8.2 Experimental . . . 108
8.3 Results . . . 108
8.4 Conclusions . . . 113

9 Strong slowing down of water reorientation in mixtures of water and tetramethylurea 115
9.1 Introduction . . . 115
9.2 Experimental methods . . . 116
9.3 Results and Interpretation . . . 116
9.3.1 Linear spectra . . . 116
9.3.2 Isotropic transient spectra . . . 116
9.3.3 Anisotropy dynamics . . . 122
9.4 Discussion . . . 124
9.5 Conclusions . . . 126

10 Destabilization of the hydrogen-bond structure of water by the osmolyte trimethylamine-N-oxide **127**
10.1 Introduction 127
10.2 Experimental 128
10.3 Results and Discussion 128
10.4 Conclusions 133

Bibliography **135**

Summary **145**

Samenvatting **149**

Dankwoord **157**

1 Introduction

1.1 Liquid water and hydrogen bonds

Throughout the years liquid water has never ceased to fascinate scientists. Biologists and chemists see water as the solvent of life; it is the medium in which the biochemical reactions that constitute life take place. In these reactions water is not merely a passive solvent; it often acts actively as a reactant and, in addition, it plays a prominent role in the folding of proteins and other biological molecules. When comparing water to other substances, it becomes apparent that water has many anomalous properties, and these have drawn the attention of physicists and physical chemists. To name a few examples: water is a liquid at room temperature whereas other compounds of similar molecular weight are gaseous; water expands upon freezing, in contrast with most liquids, which shrink; and finally, no other liquid can dissolve salts as well as water can. It has been claimed that there are as many as sixty-three of these anomalies of water. One cannot help but wonder how a simple triatomic molecule can display so many uncommon properties. Upon closer inspection, however, it becomes clear that the peculiar properties of water, most of which are essential in making water suitable for life, find their origin in only one underlying property: the ability of water molecules to form a dense spatial network of hydrogen bonds.

Hydrogen bonds arise when hydrogen is covalently bound to an electronegative element, such as O, N or F. The binding electrons are drawn towards the electronegative atom, and this causes the hydrogen atom to acquire a small positive charge. As a result, the hydrogen atom is attracted to the lone pairs of other electronegative elements. The hydrogen bond is a motif that is encountered everywhere in living nature, not only in liquid water. The majority of biological macromolecules, such as DNA and proteins, are shaped by hydrogen bonds (figure 1.1), which, in addition to structuring these macromolecules, also provide them with the flexibility they need to function properly [102].

In liquid water hydrogen bonds of the type $\mathrm{OH}\cdots\mathrm{O}$ are responsible for the strong attraction between water molecules [25]. A water molecule can engage into a maximum of four hydrogen bonds; it can accept two hydrogen bonds and simultaneously donate two. In ice this maximum number of hydrogen bonds is indeed formed, which leads to a tetrahedral structure in which every water molecule is fourfold coordinated by other water molecules. In the liquid phase the ordered structure collapses and acquires some degree of disorder. Locally, however, the average tetrahedral coordination is retained (figure 1.1a) and liquid water is said to be a highly coordinated and structured liquid [73]. Other hydrogen bonded liquids than water exist, such as methanol, but water is unique

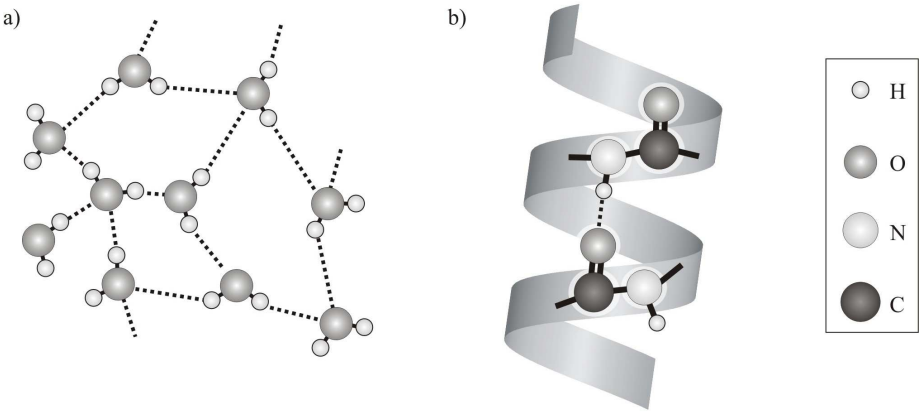

FIGURE 1.1. a) Tetrahedral structure of liquid water. The hydrogen bonds are represented as dotted lines. b) The alpha-helix, a structural motif in proteins, is held together by hydrogen bonds between the amide groups of different amino acids.

in its ability to form a three-dimensional network of hydrogen bonds. This three-dimensional hydrogen-bond network is highly dynamic: hydrogen bonds stretch, contract, break and reform on a picosecond timescale [26, 72, 76, 83].

Infrared spectroscopy can be used for studying water and other hydrogen-bonded systems. Figure 1.2 shows the mid-infrared spectrum of water. This region of the spectrum is sensitive to molecular vibrations [6, 41]. In the spectrum two resonances can be discerned: one around 1600 cm^{-1}, which is due to the HOH bending vibration, and one around 3400 cm^{-1} due to the two OH stretching vibrations. The OH stretching vibration is particularly well suited to study hydrogen bonding, as its frequency provides direct information about the hydrogen-bond strength: the stronger the hydrogen bonds, the lower the OH stretching frequency [60, 71, 83]. In liquid water many different conformations of water molecules exist, some of which are strongly hydrogen bonded, others which are weakly hydrogen bonded. These conformations absorb at different frequencies, which causes the large spectral width of the OH-stretching absorption. The band is said to be inhomogeneously broadened [59].[a] Because of the rapid interconversion of different hydrogen-bonded conformations, conventional (linear) infrared spectroscopy can only obtain time-averaged information about the structure of water. In order to obtain dynamic information one has to resort to nonlinear spectroscopic techniques, which use ultrashort laser pulses ($\sim$100 fs) to obtain instantaneous snapshots of the hydrogen bond structure. In this thesis we will use one of these techniques, mid-infrared pump-probe spec-

[a] An additional factor contributing to the width of the OH-stretching band is the coupling of the two OH vibrations of H_2O, which leads to a symmetric and antisymmetric combination which absorb at different frequencies.

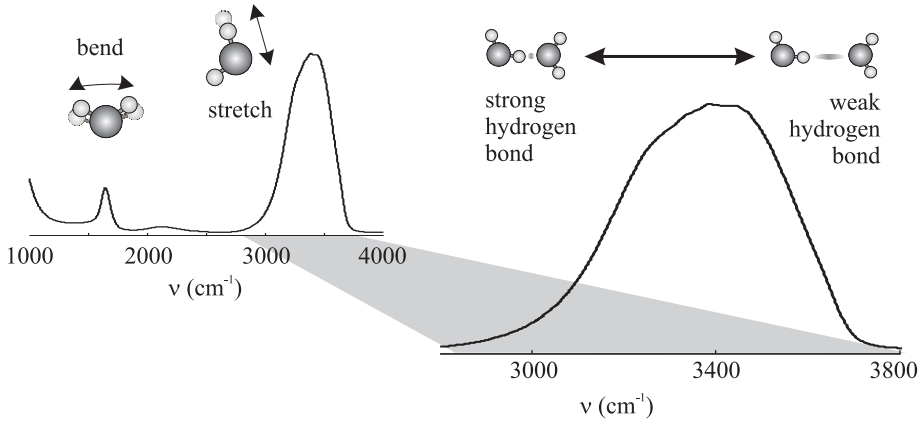

FIGURE 1.2. Mid-infrared spectrum of water which shows the absorption due to the bending and stretching vibrations of the water molecule. The OH-stretching vibration is strongly inhomogeneously broadened as a result of the hydrogen-bond interaction. There is a strong correlation between the hydrogen-bond strength of a water molecule and its OH-stretching frequency. Strongly bound water molecules absorb on the low-frequency side of the spectrum, and weakly bound water molecules absorb on the high-frequency side.

troscopy [20, 24, 27, 33, 34, 36, 43, 53, 57, 66, 68–70, 96–98, 112, 113], to study the dynamical aspects of hydrogen bonding in pure water and other systems. An advantage of mid-infrared pump-probe spectroscopy is that, when it is performed in a polarization-resolved manner, it also allows one to monitor the rotational *motion* of water molecules, and we will make extensive use of this property. In fact, the central question in this thesis is how the motion of water molecules is affected by hydrogen bonds and by the nearby presence of other molecules.

OUTLINE OF THIS THESIS The coming sections of this first chapter will introduce the theory behind the ultrafast spectroscopy of hydrogen-bonded systems. We will discuss various aspects of pump-probe spectroscopy and demonstrate how the method can be used to obtain information about the dynamical processes occurring in water. Chapter 2 takes a more theoretical approach and provides an alternative description of pump-probe spectroscopy, in terms of the nonlinear response formalism. The experimental aspects of the technique are presented in chapter 3. Chapters 4 through 10 describe the different experiments that have been performed. Chapter 4 is the only chapter that does not deal with water. It describes experiments performed on phenol that is hydrogen bonded to acetone. Chapters 5 and 6 deal with isotopically diluted water and form the basis for the next chapters (7 until 10) which treat the orientational dynamics of HDO molecules in different types of solutions.

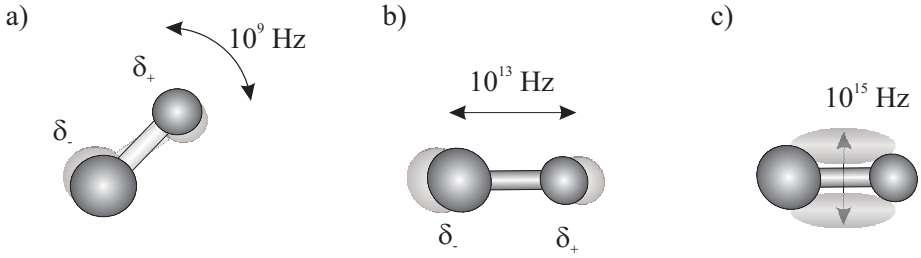

FIGURE 1.3. The three degrees of freedom of a diatomic molecule that form the basis for rotational, vibrational and electronic spectroscopy. For molecules that are composed of two different atoms the binding electrons will not be divided equally among the two atoms, which leads to partial charges on the two atoms (δ_+ and δ_-). a) The rotational motion of the molecule causes these two charges to oscillate, thus providing a coupling with microwave radiation. b) The vibrational motion of the nuclei occurs at higher frequencies and leads to a charge oscillation that is resonant with infrared radiation. c) The interaction of optical radiation with the electrons constituting the chemical bond between the two atoms forms the basis for electronic spectroscopy.

1.2 VIBRATIONAL SPECTROSCOPY

In this section we provide a theoretical description of vibrational spectroscopy. In particular we consider the formalism for describing the vibrations of molecules and their interaction with light. Before presenting this description, however, let us briefly consider the wavelength region used in vibrational spectroscopy and its position with respect to other types of spectroscopy. The part of the electromagnetic spectrum that is resonant with molecular vibrations is the infrared. It includes wavelengths ranging from 1 μm to 100 μm. At longer wavelengths (100 μm to 1 cm) lies the domain of rotational spectroscopy, which uses the microwave part of the spectrum to study rotational transitions in molecules. At shorter wavelengths (10 nm to 1 μm) the visible and ultraviolet regions of the spectrum can be found, which induce electronic transitions in molecules; hence comes the name electronic spectroscopy. Figure 1.3 illustrates the physical processes underlying these types of spectroscopy using the diatomic molecule as an example.

1.2.1 MICROSCOPIC DESCRIPTION: THE HARMONIC OSCILLATOR

The vibrations of molecules can be described as a collection of quantum mechanical harmonic oscillators [6, 14, 41]. Figure 1.4a displays the simplest possible example of a harmonic oscillator: a particle of mass m that is connected to a body of infinite mass by spring with spring constant k. This system has the following Hamiltonian

$$\hat{H}_0 = \frac{\hat{p}^2}{2m} + \frac{1}{2}k\hat{x}^2, \tag{1.1}$$

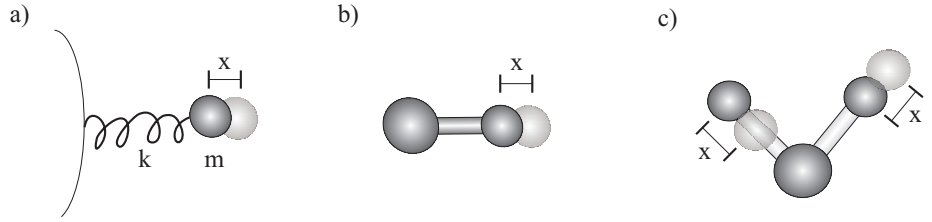

FIGURE 1.4. a) The harmonic oscillator. A particle of mass m is attached to a body of infinite mass by an ideal spring with spring constant k. The vibrations of molecules can be described by harmonic oscillators provided that certain substitutions are made. b) For the diatomic molecule the only change is that the mass m of the oscillator should be replaced by the reduced mass of the system $(m_1 m_2/(m_1 + m_2))$. c) Vibrations of polyatomic molecules are described in terms of normal modes. Here the antisymmetric mode of H_2O is shown. Such a vibration can still be described by a single coordinate, which represents a linear combination of the atomic displacements during the vibration.

where $\hat{p}$ and $\hat{x}$ are the momentum and position operators.[b] Of course, this is an idealized system that is very different from a real molecule; however, it is convenient because more complex systems, such as diatomic and polyatomic molecules, are described by Hamiltonians of the same form. Clearly for these systems the parameters in eqn. 1.1 have to be interpreted in a different way. For a diatomic molecule the mass m no longer represents the particle mass but rather the reduced mass of the two atoms (figure 1.4b). In the case of polyatomic molecules the situation is more complex because we have to take into account the fact that multiple atoms move at the same time. By working with normal mode coordinates, however, a vibration can still be described by a single displacement coordinate x [41]. A normal mode coordinate describes the synchronous displacement of all atoms during the course of a vibration. As an example figure 1.4c shows the antisymmetric vibration of H_2O. For polyatomic molecules the mass m in eqn. 1.1 represents the effective mass of the vibration, which is a measure for the amount of mass that moves around during the vibration and is generally a complicated expression of the atomic masses.

We now consider the solutions to the harmonic oscillator. The allowed states $|\phi\rangle$ follow from the time-independent Schrödinger equation

$$\hat{H}|\phi\rangle = E|\phi\rangle, \tag{1.2}$$

where E is the total energy. The eigenenergies turn out to be given by

$$E_v = \hbar\omega_0(v + \frac{1}{2}), \tag{1.3}$$

where $\omega_0 = \sqrt{k/m}$ represents the resonance frequency of the classical oscillator and v the vibrational quantum number. A wavefunction $|\phi_v\rangle$, which we will

[b] Quantum mechanical operators will be denoted by a hat ˆ.

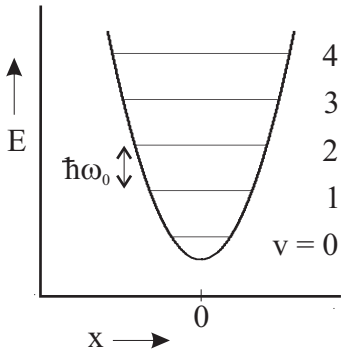

FIGURE 1.5. Energy level diagram of the harmonic oscillator.

also denote as $|v\rangle$, is associated with every eigenenergy E_v. We see that the energies are equally spaced, as shown in figure 1.5.

Transitions between the energy levels can be induced by applying a time-dependent perturbation to the Hamiltonian. In the case of a vibrating molecule, irradiation with infrared light provides such perturbation. The effect of such a perturbation can be described with the time-dependent Schrödinger equation,

$$i\hbar\frac{\partial}{\partial t}|\phi\rangle = \hat{H}|\phi\rangle. \tag{1.4}$$

The Hamiltonian is the sum of the unperturbed Hamiltonian $\hat{H}_0$ and the time-dependent perturbation $\hat{V}_{\rm int}(t)$,

$$\hat{H} = \hat{H}_0 + \hat{V}_{\rm int}(t). \tag{1.5}$$

We will assume that the perturbation varies harmonically with time,

$$\hat{V}_{\rm int} = \hat{V}(e^{i\omega t} + e^{-i\omega t}), \tag{1.6}$$

as this is the form of the light-matter interaction if the coupling $\hat{V}$ is written as

$$\hat{V} = -\frac{1}{2}\vec{\hat{\mu}}\cdot\vec{E}_0. \tag{1.7}$$

Here $\vec{\hat{\mu}}$ is the dipole moment operator. In the above equation we have used the electric-dipole approximation and assumed the following expression for the oscillating electric field

$$\vec{E}(t) = \vec{E}_0\cos\omega t, \tag{1.8}$$

$$= \frac{1}{2}\vec{E}_0(e^{i\omega t} + e^{-i\omega t}). \tag{1.9}$$

Fermi's golden rule gives the rate W_{kl} at which transitions occur from state $|l\rangle$ to $|k\rangle$

$$W_{kl} = \frac{2\pi}{\hbar^2}|\langle k|\hat{V}|l\rangle|^2\left[\delta(\omega_{kl}-\omega)+\delta(\omega_{kl}+\omega)\right], \tag{1.10}$$

where $\omega_{kl} = (E_k - E_l)/\hbar$. The delta functions ensure that transitions occur only when the photon energy $\hbar\omega$ matches the energy difference between the states. A result of Fermi's golden rule is that the probability of light absorption equals the probability of stimulated emission.

If we explicitly write out the coupling term in the above equation, we obtain

$$W_{kl} = \frac{\pi}{2\hbar^2}|\langle k|\vec{E}_0 \cdot \vec{\hat{\mu}}|l\rangle|^2, \tag{1.11}$$

$$= \frac{\pi E_0^2}{2\hbar^2}\cos^2(\theta)\mu_{kl}^2, \tag{1.12}$$

where we have assumed resonant excitation. The quantity $\vec{\mu}_{kl} = |\langle k|\vec{\hat{\mu}}|l\rangle|$ is called the transition dipole moment; it is the molecular quantity that determines the strength of an absorption. θ is the angle between the transition dipole moment and the electric field polarization. We see that transitions are most likely to occur if the radiation is polarized parallel to the transition dipole moment.

As it stands the above equation can refer to any type of dipolar transition. In order to have it refer to a vibrational transition we need to specify the form of the dipole moment operator. This operator depends on the electronic wave function but we can obtain a useful phenomenological expression by expanding it as a function of the vibrational coordinate x

$$\vec{\hat{\mu}} \approx \vec{\mu}_0 + \hat{x}\frac{\partial\vec{\mu}}{\partial x}. \tag{1.13}$$

Note that the operator character has been switched from $\vec{\hat{\mu}}$ to $\hat{x}$. If we use this expression for the dipole moment, we arrive at

$$W_{kl} = \frac{\pi E_0^2}{2\hbar^2}\cos^2\theta\left(\frac{\partial\vec{\mu}}{\partial x}\right)^2|\langle k|\hat{x}|l\rangle|^2. \tag{1.14}$$

This expression contains a number of factors, each of which represents a selection rule in vibrational spectroscopy. Below we summarize these selection rules:

- $W_{kl} \propto (\frac{\partial\vec{\mu}}{\partial x})^2$

  A vibration is only infrared active if the vibrational motion leads to a change in the dipole moment. As a consequence symmetric vibrations, such as the vibrations of O_2 and N_2 and the symmetric stretching vibration of CH_4 are not observed in infrared spectroscopy.

- $W_{kl} \propto |\langle k|\hat{x}|l\rangle|^2$

  In the harmonic approximation the matrix element $\langle k|\hat{x}|l\rangle$ is only non-zero for $l = k \pm 1$. As a consequence the only allowed transitions are those that change the excitation of the oscillator by one quantum of energy. There are two effects that can lead to a relaxation of this selection rule. The first is an anharmonicity in the potential energy of the oscillator (i.e. the presence of higher order terms in the potential energy: $\sim x^3$, $\sim x^4$, etc.).

This mechanical anharmonicity leads to the coupling of wave functions for which $|l-k| > 1$. A second possibility is the presence of quadratic and higher order terms in the expansion of the dipole moment (eqn. 1.13). Higher order coupling terms of the form $\hat{x}^n$ lead to the coupling of states for which $|l-k| = n$. This kind of anharmonicity is known as electrical anharmonicity. In general multiple-quantum transitions are much weaker than single-quantum transitions.

- $W_{kl} \propto \cos^2(\theta)$

  Only the electric field component parallel to the transition dipole moment (i.e. in the direction of change of the dipole moment) can induce transitions. No transitions can occur if the radiation is polarized perpendicular to the transition dipole.

1.2.2 Macroscopic description: Lambert-Beer's law

Fermi's golden rule provides a microscopic expression for the rate at which energy is absorbed from a beam of light. In this section we relate this equation to a macroscopic expression for the attenuation of the light beam. We begin with the expression for the intensity I in terms of the amplitude of the electric field (eqn. 1.8)

$$I(\omega) = \frac{1}{2} c\epsilon_0 E_0^2(\omega). \tag{1.15}$$

Here c is the speed of light and ϵ_0 is the permittivity of free space. In terms of the intensity we can write the transition rate from eqn. 1.12 as

$$W_{kl} = \frac{\pi I(\omega_{kl})}{3\hbar^2 c\epsilon_0} \mu_{kl}^2, \tag{1.16}$$

where we have assumed that the sample is isotropic so that we can replace $\cos^2\theta$ by its average value of $\frac{1}{3}$. The rate at which energy is absorbed from a beam of light by a single molecule is found by multiplying the transition rate by the photon energy

$$P(\omega_{kl}) = \hbar\omega_{kl} W_{kl}. \tag{1.17}$$

In writing this equation we have assumed that the population of the excited state is negligible compared to the ground state population. Since the absorbed power is proportional to the intensity of the light beam, we can define a new molecular quantity, the absorption cross section σ, as the absorbed power scaled to the intensity of the light,

$$\sigma(\omega_{kl}) \quad = \quad \frac{P(\omega_{kl})}{I(\omega_{kl})}. \tag{1.18}$$

We would now like to relate the power absorbed by a single molecule to the attenuation of the light because this is a quantity that can be straightforwardly determined. For this purpose we consider a volume V through which a beam of light propagates (figure 1.6). This volume contains absorbing molecules at

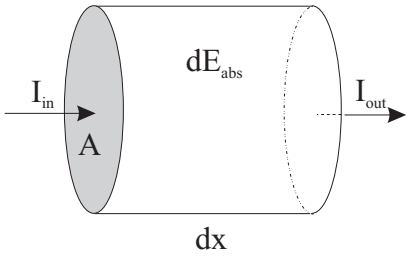

FIGURE 1.6. Cylindrical region of space through which a beam passes. The absorption in this region equals the difference between the flux entering and leaving the region.

a concentration C and has a cross-sectional area A. The amount of energy ($dE_{\rm abs}$) that is absorbed in this volume during the time dt is given by

$$\begin{aligned} dE_{\rm abs}(\omega_{kl}) &= P_{\rm tot}(\omega_{kl})\,dt, & (1.19)\\ &= CV\sigma(\omega_{kl})I(\omega_{kl})\,dt, & (1.20)\\ &= C\sigma(\omega_{kl})I(\omega_{kl})A\,dx\,dt. & (1.21) \end{aligned}$$

In the upper equation $P_{\rm tot}$ stands for the power absorbed by all molecules in the volume; in the second equation we have used eqn. 1.18 and the fact that the number of molecules in the volume is given by CV. d$E_{\rm abs}$ can also be obtained by considering the incoming and outgoing intensities (figure 1.6)

$$\begin{aligned} dE_{\rm abs}(\omega_{kl}) &= (I_{\rm in}(\omega_{kl}) - I_{\rm out}(\omega_{kl}))A\,dt, & (1.22)\\ &= -A\,dI\,dt. & (1.23) \end{aligned}$$

Equating these two we obtain

$$dI(\omega_{kl}) = -\sigma(\omega_{kl})CI(\omega_{kl})\,dx. \tag{1.24}$$

This is Lambert-Beer's law in differential form; integration leads to the familiar result

$$T(\omega_{kl}) = \frac{I(\omega_{kl})}{I_0(\omega_{kl})} = e^{-\sigma(\omega_{kl})Cl}, \tag{1.25}$$

where I_0 is the light intensity before the entering the sample, T is the transmission and l is the sample length. In general one works with the absorbance, which is the natural logarithm of the transmission and has the advantage that it depends linearly on all parameters

$$\alpha(\omega_{kl}) = -\ln\left(T(\omega_{kl})\right) = \sigma(\omega_{kl})Cl. \tag{1.26}$$

Lambert-Beer's law provides the connection between the absorption cross section, which is a molecular property, and the attenuation of a beam of light, which can be easily determined experimentally. Finally by combining equations 1.16 to 1.18, we see that the absorption cross-section is related to the

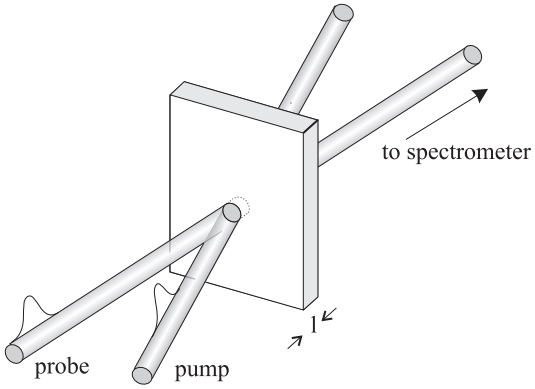

FIGURE 1.7. Schematic representation of the pump-probe experiment. A sample of thickness l is illuminated by a pump pulse, which excites a significant fraction of the molecules. Next a time-delayed probe pulse is used to monitor the spectral changes induced by the first pulse.

transition dipole moment in the following manner

$$\sigma(\omega_{kl}) = \frac{\pi\omega_{kl}}{3\hbar c\epsilon_0}\mu_{kl}^2. \tag{1.27}$$

We remark that the cross section is a quantity that is averaged over all molecular orientations, whereas the transition dipole moment is linked to the molecular frame.

1.3 VIBRATIONAL PUMP-PROBE SPECTROSCOPY

Up to now we have dealt with linear absorption, which mainly provides information about the *static* properties of molecules. In some cases *dynamical* information can also be obtained from a linear spectrum. This is because the spectral widths of transitions contain information about the equilibrium fluctuations experienced by molecules. However, often there are additional (inhomogeneous) broadening mechanisms at play which obscure the dynamical information contained in the absorption lineshape. Nonlinear spectroscopies, such as pump-probe spectroscopy, overcome this problem by directly probing non-equilibrium properties of a sample. In particular, the sample is first brought into a non-equilibrium state by an intense pump pulse, after which the relaxation to the equilibrium state is monitored by a weak, time-delayed probe pulse (figure 1.7).

Here we will discuss the general principles that underlie the pump-probe experiment, focusing in particular on those aspects that are observed in the vibrational pump-probe spectroscopy of water. We first consider the absorption

α_0 experienced by a weak probe pulse in the absence of a pump pulse

$$\alpha_0(\omega) = \sigma_{01}(\omega)Cl, \tag{1.28}$$
$$= \sigma_{01}(\omega)n, \tag{1.29}$$

where we have introduced the symbol n to denote the concentration per unit surface. After excitation by the pump pulse the sample will exhibit a modified absorption due to three effects (figure 1.8). First, after excitation there are less molecules in the ground state, so that the sample shows a decreased absorption at the fundamental frequency. A second effect leading to a decreased absorption at this frequency is stimulated emission from the excited state. Finally, the excited molecules can be further excited to the $v = 2$ state, which causes an increased absorption at the frequency of the $1 \rightarrow 2$ transition. These effects lead to the following expression for the absorption

$$\alpha(\omega) = \sigma_{01}(\omega)(n - 2N_1) + \sigma_{12}(\omega)N_1, \tag{1.30}$$

where N_1 is the concentration of excited molecules. The factor 2 enters because ground state depletion and stimulated emission contribute equally to the absorption change. In a pump-probe experiment we usually record the absorption spectrum of the probe beam in the presence and absence of the pump pulse. The transient absorption $\Delta\alpha$ is defined as the difference between these two spectra

$$\Delta\alpha(\omega) = \alpha(\omega) - \alpha_0(\omega) = (-2\sigma_{01}(\omega) + \sigma_{12}(\omega))N_1. \tag{1.31}$$

The transient spectrum consists of two contributions; the negative contribution, arising from the ground state depletion and stimulated emission, is called the bleaching signal; the positive contribution is called the induced absorption or excited state absorption.

1.3.1 Vibrational relaxation

After excitation the transient spectrum will decay because excited molecules relax to the ground state. In general the excited state population decays exponentially with time. If relaxation proceeds immediately to the ground state (figure 1.9a) this leads to an exponential decay of both the induced absorption and the bleach,

$$\Delta\alpha(\omega, t) = (-2\sigma_{01}(\omega) + \sigma_{12}(\omega))N_1(t), \tag{1.32}$$
$$= (-2\sigma_{01}(\omega) + \sigma_{12}(\omega))N_1(0)e^{-t/\tau_1}, \tag{1.33}$$

where τ_1 is the lifetime of the vibration. The lifetime of a vibration depends strongly on its surroundings; in solution it can vary from hundreds of picoseconds to less than a picosecond. For example, the vibrational lifetime of the OD vibration of HDO in H_2O is 1.8 ± 0.2 ps [85], while the surface OD groups of deuterated zeolites can have lifetimes of 70 ps [12].

In general vibrational relaxation proceeds through complicated mechanisms that may involve a number of intermediate states. An example is shown in

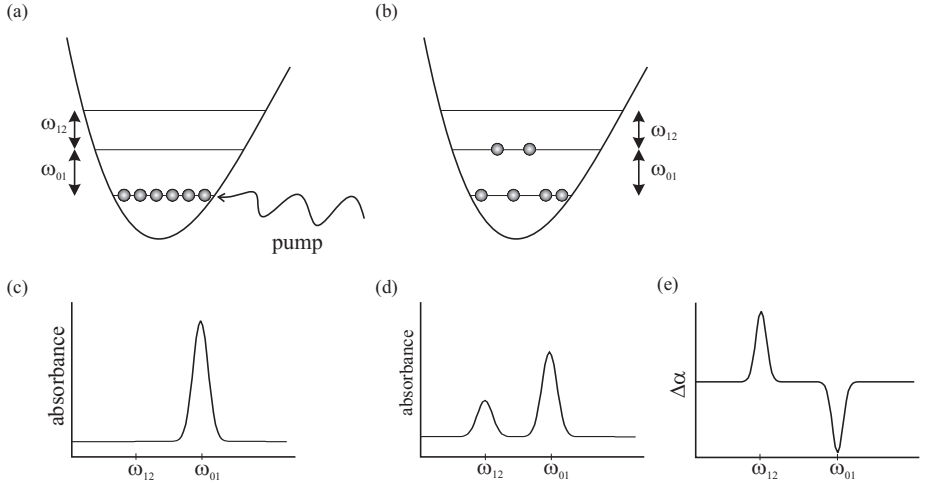

FIGURE 1.8. Principle of vibrational pump-probe spectroscopy. a,c) Potential energy diagram of a typical vibration. In thermal equilibrium all molecules are in the ground state, which leads to an absorption at ω_{01}. b,d) A pump pulse promotes a significant fraction of the molecules to the first excited state. This leads to a decreased absorption at ω_{01} and an increased absorption at ω_{12}. e) The transient spectrum is the difference between the spectra in the presence and absence of the pump pulse.

figure 1.9b. Here the intermediate levels represent states in which the original vibration has relaxed and excited a low-frequency inter- or intramolecular vibration. If the two vibrations are coupled via an anharmonic interaction, excitation of the low-frequency mode will result in a frequency shift of the high-frequency vibration. Figure 1.10 illustrates this effect for the H_2O molecule. We will describe this effect by assigning different spectra to the intermediate states than to the excited state. The relaxation mechanism in figure 1.9b also shows that excited molecules do not necessarily relax to the original ground state. This is a way of describing irreversible changes induced by the pump pulse. For pump pulses in the visible or ultraviolet the irreversible change often consists in a chemical reaction. In the infrared it is generally only heating of the sample, although a few examples of infrared-induced chemical reactions are known. For the relaxation mechanism shown in figure 1.9b we can write the following expression for the transient signal

$$\begin{aligned}\Delta\alpha(\omega,t) &= \sigma_{12}(\omega)N_1(t) - \sigma_{01}N_1(0) - \sigma_{01}(\omega)N_1(t) \\ &\quad +\sigma^*_{01}(\omega)N^*_0(t) + \sigma'_{01}(\omega)N'_0(t),\end{aligned} \tag{1.34}$$

where $\sigma^*_{01}(\omega)$ and $\sigma'_{01}(\omega)$ represent the cross section spectra of the intermediate state and of the modified ground state. The expression consists of five terms. The first term represents the excited state absorption. The second and third term arise from ground state depletion and stimulated emission, respectively. Finally the fourth and the fifth term are due to the absorption of the interme-

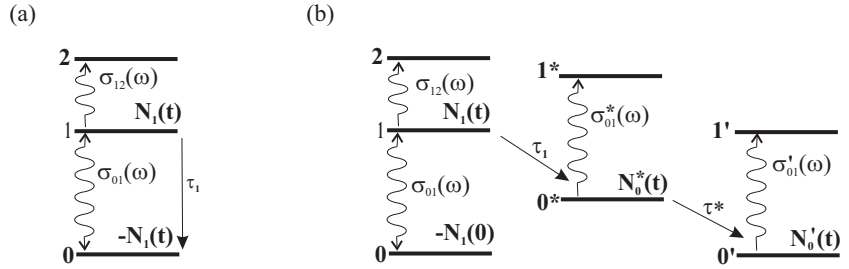

FIGURE 1.9. a) Example of a relaxation mechanism in which an excited vibration relaxes directly to the ground state. b) Example of a relaxation mechanism that involves an intermediate state. In this example the molecules do not relax to the original ground state. This accounts for an irreversible change induced by the pump pulse, such as a chemical reaction or sample heating. In this figure wiggly lines denote radiative transitions, while the arrows represent non-radiative transitions.

diate state and the modified ground state.

1.3.2 INHOMOGENEOUS BROADENING AND SPECTRAL DIFFUSION

In the foregoing discussions it was implicitly assumed that infrared absorption lines are homogeneously broadened. This means that every molecule has essentially the same absorption spectrum. The bandwidth over which a single molecule absorbs radiation is referred to as the homogeneous linewidth of the particular transition. However, infrared absorption bands can also be inhomogeneously broadened, an example of which is the OH stretching vibration in liquid water. In this case the broadening of the absorption arises because different molecules absorb at different center frequencies. In linear spectroscopy homogeneous and inhomogeneous broadening cannot be distinguished; in pump-probe spectroscopy, on the other hand, the difference is immediately clear.

Figure 1.11 exemplifies this issue. We investigate the effect of using a pump-pulse that has a narrower frequency distribution than the (inhomogeneously broadened) absorption band. Since the absorption band consists of species that absorb at different center frequencies, rather than of a single species that absorbs over a wide frequency interval, not all molecules are resonant with the pump pulse. As a result only part of the absorption band is bleached (figure 1.11a) and the spectrum after excitation by the pump will have a hole in it. As a consequence of this effect the transient spectrum can be narrower than the linear spectrum. In this case pump-probe spectroscopy is sometimes also referred to as hole-burning spectroscopy.

The variation in the center frequencies is due to the different environments of the various molecules. In a liquid these environments interconvert on a characteristic timescale and this causes the absorption frequency of a particular

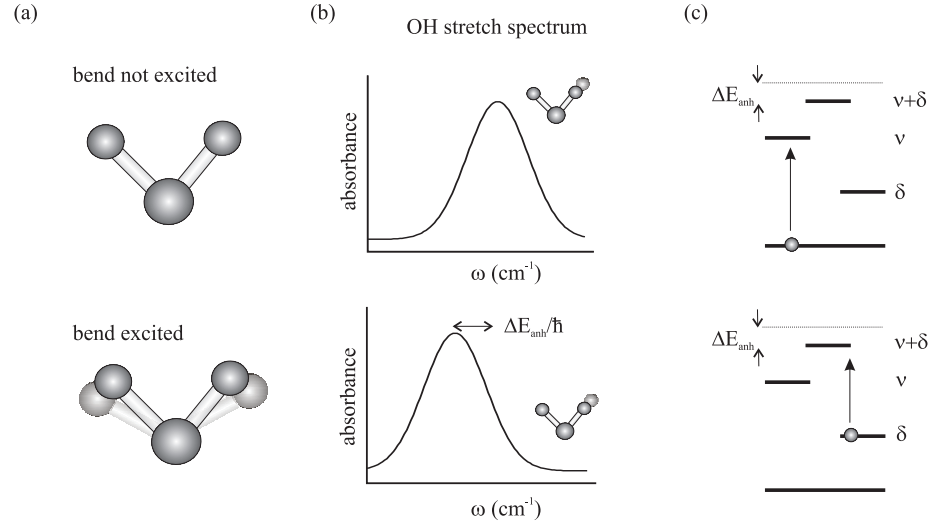

FIGURE 1.10. Effect of the anharmonic interaction between the OH stretching vibration (ν) and the bending vibration (δ) of H_2O. a) An H_2O molecule in its vibrational ground state and an H_2O molecule with one excitation quantum in the bending vibration. b) Absorption spectrum of the OH-stretching vibration of H_2O for the vibrational ground state and for the first excited state of the bending vibration. The OH stretching spectrum shifts to lower frequencies if the bending vibration is excited. c) Energy level diagram of H_2O taking into account only the first excited states of the stretching (ν) and bending vibrations (δ). Due to the anharmonic interaction (ΔE_{anh}) the doubly excited state lies lower in energy than the sum of the two singly excited states.

molecule to fluctuate in time. If a narrow-band pulse is used to excite the sample, this will lead to the excitation of a non-equilibrium distribution of transition frequencies. The transient spectrum will therefore broaden upon increasing the pump-probe delay until it reaches the equilibrium shape. The rate at which the transient spectrum broadens provides a way to determine the timescale of the frequency fluctuations.

Finally we point out that in the case of inhomogeneous broadening the width of absorption bands can be so large that ground state bleach and induced absorption overlap. This is the case for the OH stretch vibration of water. Figure 1.11c displays the characteristic lineshape that this leads to.

1.3.3 SAMPLE HEATING

In section 1.3.1 it was mentioned that an infrared pump pulse will eventually heat the sample. In particular, the pumped volume will show an increase in temperature after every pump pulse. Subsequently the temperature decreases on a microsecond to millisecond timescale as heat diffuses out of the pumped region. However, with respect to the picosecond timescale of a pump-probe

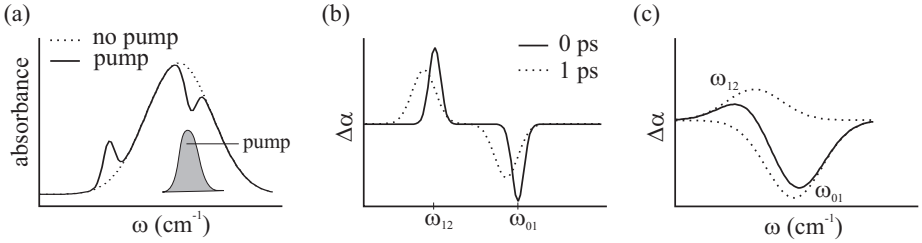

FIGURE 1.11. Inhomogeneous broadening and spectral diffusion. a) A pump pulse that is narrower than the width of an inhomgeneously broadened absorption band will burn a hole in it. b) At zero delay the transient spectrum will show bleaching and induced absorption features, the widths of which are determined by the pump pulse. As the pump-probe delay is increased frequency fluctuations will lead to the broadening and shifting of the transient spectrum until it reaches its equilibrium shape. c) Typical shape of the transient spectrum of water. The bleaching and induced absorption (dotted lines) are broadened to such extent that they overlap. The solid line represents the sum of the bleaching and induced absorption.

experiment, we can consider the temperature jump to be permanent. As the shapes of many spectral bands are sensitive to temperature, the effect of the temperature jump becomes visible in the transient spectrum (figure 1.12a). The transient spectrum represents the difference in absorption between a pumped and an unpumped sample. Therefore, when all excitation dynamics have decayed, the transient spectrum will not have decayed to zero, but will rather be identical to the temperature difference spectrum of the initial and final temperature (figure 1.12b).

Figure 1.13 shows the dynamics of a typical transient spectrum of water including the effects of inhomogeneous broadening and heating. At short delays the bleaching and induced absorption are discerned, which decay to the temperature difference spectrum.

1.3.4 ARTIFACTS

When the pump and probe pulses overlap in time specific effects occur that are not directly related to the dynamics of the vibrational excitation. These effects are known as artifacts. There are two types of artifacts that need to be considered: the coherent artifact and the cross-phase modulation artifact.

COHERENT ARTIFACT The coherent artifact is a consequence of the interference of the pump and probe fields. Writing the total field as

$$E(t) = E_{\text{pump}} e^{i\omega t - i\vec{k}_1 \cdot \vec{r}} + E_{\text{probe}} e^{i\omega t - i\vec{k}_2 \cdot \vec{r}} + \text{ c.c.}, \tag{1.35}$$

it is readily seen that the intensity distribution ($\propto E^2(t)$) contains an interference term of the form

$$E_{\text{pump}} E_{\text{probe}} \cos(\vec{k}_1 - \vec{k}_2) \cdot \vec{r}. \tag{1.36}$$

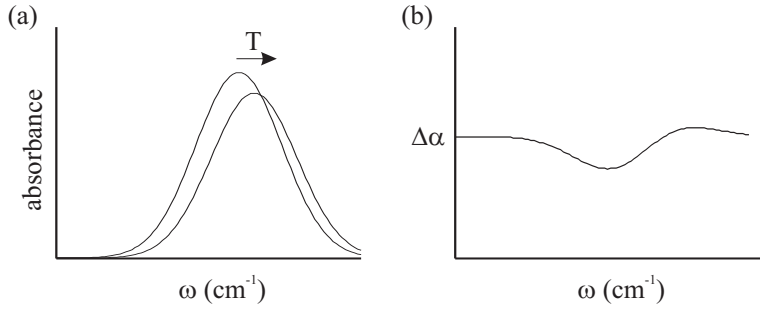

FIGURE 1.12. a) The effect of temperature on the OH stretching band of water. The band shifts to higher frequencies and decreases in intensity as the temperature is increased. b) Once all excitation dynamics have decayed In a transient spectrum we observe the difference between the spectra at the two different temperature.

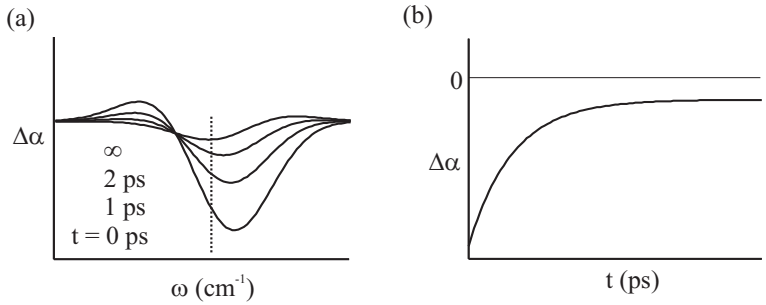

FIGURE 1.13. a) Typical transient spectrum of water, including the effects of inhomogeneous broadening and heating. At short delays ground state bleaching and induced absorption are observed. These decay to a constant temperature difference spectrum that shows no dynamics on the timescale of a pump-probe experiment. b) Time trace along the dotted line in the data from a).

This distribution creates a spatial modulation of the excited state population in the sample (figure 1.14), which will act as a grating. As a result pump light is diffracted in the direction of the probe beam. Because more light reaches the detector in the presence of the pump than in its absence, this effect may be mistaken for a bleaching signal. The coherent artifact is only observed when the pump and probe pulses overlap in time.

CROSS-PHASE MODULATION The cross-phase modulation artifact arises due to the modification of the index of refraction of the sample by the high intensity of the pump pulse. A phenomenological expression for this intensity-dependent refractive index is

$$n(t) = n_0 + n_2 I(t), \tag{1.37}$$

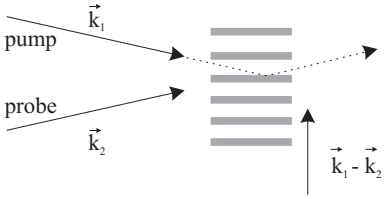

FIGURE 1.14. The coherent artifact. The pump and probe pulses create an interference pattern in the sample, which leads to a fringe pattern in the excited state population. This pattern acts as a grating that can diffract pump light in the direction of the probe.

where n_0 is the usual refractive index, n_2 is the intensity-dependent part, and $I(t)$ is the light intensity in the material. The probe is generally too weak to modify the refractive index, so that we can identify $I(t)$ with the pump intensity. According to eqn 1.37, a pump pulse that traverses a sample causes a temporal variation in the index of refraction. Let us consider the effect of this time-dependent refractive index on a probe pulse that traverses the sample at the same time as the pump. For the electric field variation of a probe pulse of frequency ω_0 we can write

$$E = E_{\text{probe}} e^{i(\omega_0 t - n k_0 x)}, \tag{1.38}$$

where $k_0 = \omega_0/c$. Substituting the time-dependent expression for n we obtain

$$E = E_{\text{probe}} e^{i(\omega_0 t - n_0 k_0 x - n_2 k_0 x I(t))}. \tag{1.39}$$

To understand what this electric field variation means, we consider its instantaneous frequency $\omega(t)$. This is defined as the time-derivative of the phase,

$$\omega(t) = \frac{d\phi}{dt}, \tag{1.40}$$

$$= \omega_0 - n_2 k_0 x \frac{dI}{dt}. \tag{1.41}$$

We see that the effect of the pump pulse is to either increase or decrease the frequency of the probe, depending on the sign of dI/dt. This is determined by the delay between the pump and probe pulse. For negative delays the probe comes before the pump, and the probe therefore primarily sees the rising edge of the pump pulse ($dI/dt > 0$). For positive delays, the probe sees the trailing edge of the pump pulse, resulting in a negative value for dI/dt. For most materials n_2 is positive; in our example x is positive too, since the wave travels in the positive x-direction. As a consequence the probe frequency decreases if the probe comes before the pump, and it increases if the probe comes after the pump. When a delay scan is taken, this effect leads to a 'wiggle' in the transient absorption around delay zero, as is illustrated in figure 1.15.

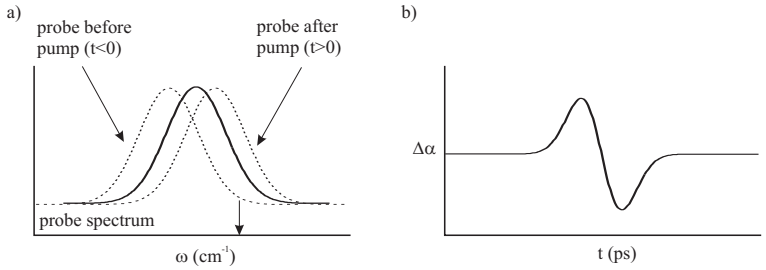

FIGURE 1.15. The cross-phase modulation artifact. a) If the probe pulse precedes the pump pulse, its spectrum is shifted to lower frequency; if it comes after the pump, it is shifted to higher frequency. b) In a delay scan the cross-phase modulation artifact leads to a wiggle. The frequency corresponds to the arrow in a).

1.4 INTERMEZZO: AMPLITUDE OF THE TRANSIENT SPECTRUM

The present section aims at creating some intuition for the factors that determine the magnitude of the pump-probe response. For simplicity we will only regard the bleaching part of the pump-probe response but the same arguments hold for the induced absorption. Let us start by considering a probe pulse that is focused down to a cross-sectional area A. As an approximation we will assume that the probe has a flat spatial intensity profile, so that we may imagine that we are really probing a cylindrical region of the sample. In the previous section we have seen that the bleaching signal induced by the pump pulse is given by

$$\Delta\alpha(\omega) = -2\sigma_{01}(\omega)N_1, \tag{1.42}$$

where N_1 is the concentration (per unit surface) of excited molecules *in the probe volume*. The concentration of excited molecules is of course determined by the intensity of the pump pulse. Since every pump photon can excite one molecule we arrive at

$$N_1 = \frac{E'_{\text{pump}}/\hbar\omega}{A}(1-T). \tag{1.43}$$

In this equation T is the integrated transmission of the sample. E'_{pump} is the pump energy that falls on the probe surface; E'_{pump} can therefore be smaller than the total pump energy. By combining the previous two equations we obtain

$$\Delta\alpha(\omega) = -\frac{2\sigma_{01}(\omega)}{A}\frac{E'_{\text{pump}}}{\hbar\omega}(1-T). \tag{1.44}$$

We see that every photon absorbed within the probe volume gives rise to an absorption change $-2\sigma_{01}(\omega)/A$. If we wish to increase the pump-probe signal, one of the options is to increase the absorption of the sample, either by increasing its thickness or by increasing the concentration. However, once a certain

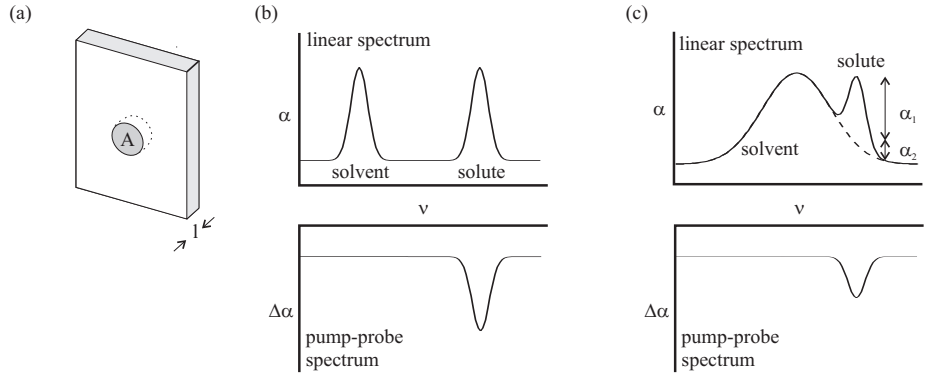

FIGURE 1.16. a) Sample used in pump-probe spectroscopy. The probe beam has a cross-sectional area A, the diameter of which is typically 100 μm. b) Solvent bands that have intensities that are equal to a solute band in the linear spectrum are not observed in a pump-probe spectrum. c) When the solute band overlaps with a solvent band in the linear spectrum, we still only observe the solute band. However, its amplitude is lower since part of the pump photons are absorbed by the solvent.

absorbance is reached, any further increase in the concentration will lead to relatively little gain in the pump-probe signal. For example, if we increase the optical density[c] of the sample from 1 to 2 by doubling the concentration, this will increase the percentage of absorbed pump photons from 90% to 99%. Therefore the pump-probe signal only increases by 10% even though the concentration has been doubled. In practice a transmission of approximately 10% is chosen so that relatively few pump photons are wasted, while there is still sufficient probe light passing through the sample.

We will define the maximum pump-probe signal as the theoretical signal when all pump photons are absorbed. This is the magnitude of the pump-probe response in the optically dense limit,

$$\Delta\alpha_{\max}(\omega) = -\frac{2\sigma_{01}(\omega)}{A}\frac{E'_{\text{pump}}}{\hbar\omega}. \tag{1.45}$$

We see that in this limit the signal is limited by the total number of available pump photons per unit probe surface and, ultimately, by the cross section of the vibration.[d] This means that, once we have reached the optically dense limit, we can only increase the signal by increasing the amount of pump light or by

[c] The optical density is defined as the ^{10} log of the transmission.

[d] Sometimes it is necessary to work at a low optical density. In this case we can write $T = \exp(-\sigma_{01}(\omega)Cl) \approx 1 - \sigma_{01}(\omega)Cl$ for the transmission and we arrive at

$$\Delta\alpha(\omega) = -\frac{2\sigma_{01}(\omega)^2 Cl}{A}\frac{E'_{\text{pump}}}{\hbar\omega}. \tag{1.46}$$

Here we have assumed that the cross-section does not vary over the frequency spectrum of pump. We see that in this limit the pump-probe signal depends linearly on the concentration and quadratically on the cross section.

focusing it more tightly. Since the signal scales quadratically with the diameter of the pump focus, it pays to invest in achieving a focus that is as tight as possible.

The fact that ultimately the pump-probe response depends on only the cross section has an interesting consequence. It explains why solvent bands are generally not observed in the pump-probe spectrum. The situation depicted in figure 1.16b is often encountered in pump-probe spectroscopy. In the linear spectrum two bands appear with equal intensity, one due to the solvent and one due to the solute; in the transient spectrum, however, only the solute band is observed. This is because the pump-probe response scales with the cross-section, which is much larger for the solute than for the solvent. In the linear spectrum the lower cross-section of the solvent is compensated by the higher concentration.

When the solute and solvent bands overlap a different situation occurs, as is shown in figure 1.16c. One must now take into account the fact that part of the pump photons do not contribute to the pump-probe response as they are absorbed by the solvent rather than by the solute. It can be shown that the relative number of photons absorbed by each band is given by the ratio of the absorptions. Incorporating this in the expression for the pump-probe signal we arrive at

$$\Delta\alpha_{\max}(\omega) = -\frac{2\sigma(\omega)}{A}\frac{E'_{\text{pump}}}{\hbar\omega}\frac{\alpha_1(\omega)}{\alpha_1(\omega)+\alpha_2(\omega)}, \tag{1.47}$$

where α_1 and α_2 are the absorbances due to the solute and solvent, respectively. We see that in order to optimize the pump-probe signal we have to minimize the fraction of the photons that is absorbed by the solvent. This can be done by using a more concentrated sample.

1.5 Polarization properties of the pump-probe response: anisotropy

Until now it was silently assumed that the excited molecules are distributed isotropically. However, in reality the distribution of excited molecules is anisotropic because molecules that have their transition dipole moments aligned parallel to the pump polarization are excited preferentially (figure 1.17a). As a consequence the amplitude of the pump-probe response depends on the relative polarizations of the pump and probe pulses (figure 1.17b). For parallel pump and probe polarizations the response is initially larger than for perpendicular polarizations (because the concentration of excited molecules is zero for molecules that have their transition dipole moments perpendicular to the pump polarization). The orientational motion of the excited molecules scrambles their orientations and eventually causes their distribution to become isotropic. As a consequence the parallel signal decays faster than the perpendicular signal and this continues until the two signals are identical. At this point the excited molecules have lost all memory of their initial orientations. It is clear that

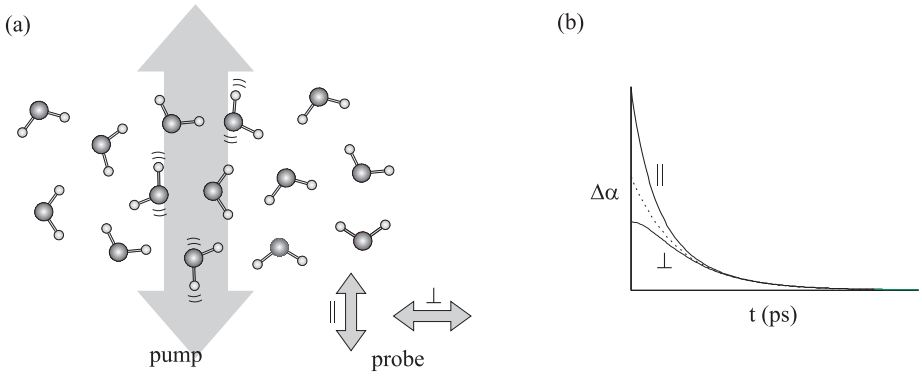

FIGURE 1.17. a) Preferential excitation of molecules that have their transition dipole moments parallel to the pump pulse polarization. b) Delay scan of the parallel and perpendicular signals. The dotted line shows the signal if the orientations of the excited molecules were distributed isotropically. The parallel signal is initially higher than the isotropic signal but decays faster; the perpendicular signal is initially lower than the isotropic signal but decays more slowly.

the rate at which the difference between the parallel and perpendicular signals decays is determined by the orientational motion of the molecules [11, 58].

1.5.1 Isotropic signal

Both the parallel and perpendicular response shown in figure 1.17b are affected by the orientational motion of the molecules, which is inconvenient if one wants to study vibrational relaxation. It would be more convenient to dispose of a response such as the dotted line in figure 1.17 which depends only on the total concentration of excited molecules. This response is referred to as the isotropic response. It may seem that averaging the parallel and perpendicular responses would yield the isotropic response. However, it turns out that this is only correct if molecules rotate in two dimensions. In three dimensions the isotropic response is found by weighing the perpendicular response more heavily,

$$\Delta\alpha_{\text{iso}} = \frac{\Delta\alpha_{||} + 2\Delta\alpha_{\perp}}{3}, \tag{1.48}$$

where $\Delta\alpha_{||}$ and $\Delta\alpha_{\perp}$ are the absorption changes when the pump and probe beams are polarized parallel and perpendicular to each other, respectively. This equation can be rationalized with the help of figure 1.18. We first consider the two dimensional situation. A single excited dipole $\vec{\mu}$ contributes to the induced absorptions of both the parallel and perpendicular responses according to

$$\Delta\alpha_{||} \quad \propto \quad \cos^2\theta, \tag{1.49}$$

$$\Delta\alpha_{\perp} \quad \propto \quad \cos^2\chi. \tag{1.50}$$

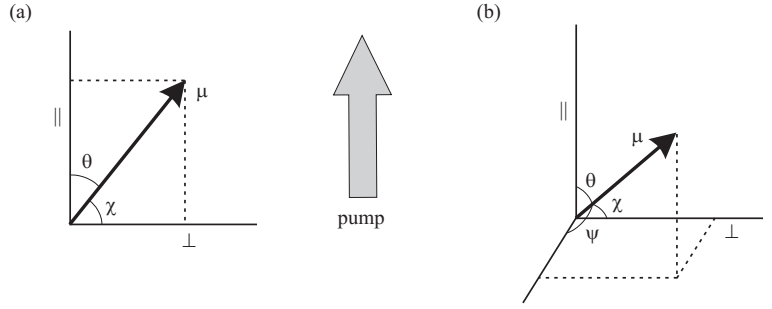

FIGURE 1.18. Contribution of a single dipole to the parallel and perpendicular pump-probe signals in two dimensions (a) and in three dimensions (b).

It is directly clear that the sum of these two signals does not depend on the orientation of the dipole. Therefore in two dimensions the isotropic signal is given by the simple average of the parallel and perpendicular signals.

In three dimensions the quantity that is independent of orientation is $\cos^2\theta + \cos^2\chi + \cos^2\psi$ (figure 1.18b) so that the absorption needs to be probed in three orthogonal directions to obtain the isotropic response. Experimentally this would not be very straightforward but fortunately matters are simplified by the cylindrical symmetry of the sample after excitation. As a result of this symmetry the *average* responses are equal for the two perpendicular probe directions, so that $\langle \cos^2\theta + 2\cos^2\chi \rangle$ is the quantity that is independent of orientation. This explains the form of eqn. 1.48.

In order to prepare for the coming discussion we also show how the above conclusion can be reached by considering the distribution of excited molecules $N(\theta, \phi, t)$. Immediately after excitation this distribution is given by

$$N(\theta, \phi, t) = g(\theta, \phi, t) N_1, \tag{1.51}$$

where N_1 represents the total concentration of excited molecules as it did in the previous sections and $g(\theta, \phi, t)$ is the function that represents the orientational distribution of excited molecules. $g(\theta, \phi, t)$ has a number of properties:

- Being a distribution function it is normalized at all times

$$\int g(\theta, \phi, t)\, d\Omega = 1, \tag{1.52}$$

  where the integral runs over the unit sphere and $d\Omega = \sin\theta\, d\theta\, d\phi$ is the surface element in spherical coordinates.

- At zero delay its functional forms is determined by the excitation probability

$$g(\theta, \phi, 0) = \frac{3}{4\pi} \cos^2\theta. \tag{1.53}$$

- In the limit of long delay times it evolves to an isotropic distribution

$$\lim_{t\to\infty} g(\theta,\phi,t) = \frac{1}{4\pi}. \tag{1.54}$$

- Finally, in an isotropic sample $g(\theta,\phi,t)$ is a function of only the polar angle

$$g(\theta,\phi,t) = \frac{g_\theta(\theta,t)}{2\pi}, \tag{1.55}$$

  where $g_\theta(\theta,t)$ is the distribution function of the polar coordinate. The factor 2π enters to ensure its normalization

$$\int_0^\pi g_\theta(\theta,t)\sin\theta\, d\theta = 1. \tag{1.56}$$

The parallel and perpendicular absorption changes can be expressed in terms of integrals over the distribution function

$$\Delta\alpha_{||}(t) = 3\sigma_{12}N_1 \int g(\theta,\phi,t)\cos^2\theta\, d\Omega, \tag{1.57}$$

$$\Delta\alpha_{\perp}(t) = 3\sigma_{12}N_1 \int g(\theta,\phi,t)\sin^2\theta\sin^2\phi\, d\Omega, \tag{1.58}$$

where in the second equation we have used the fact that $\cos^2\chi = \sin^2\phi\sin^2\theta$. The factor of 3 enters because the cross section is defined as the average (i.e. isotropic) cross section, which is three times as small as its maximum value. The independence of the isotropic signal on the distribution function can be shown as follows

$$\Delta\alpha_{\rm iso}(t) = \frac{1}{3}(\Delta\alpha_{||}(t) + 2\Delta\alpha_{\perp}(t)), \tag{1.59}$$

$$= \sigma_{12}N_1 \int g(\theta,\phi,t)(\cos^2\theta + 2\sin^2\theta\sin^2\phi)\, d\Omega. \tag{1.60}$$

We use the fact that the sample is isotropic and integrate over the azimuthal coordinate,

$$\Delta\alpha_{\rm iso}(t) = \sigma_{12}N_1 \int \frac{g_\theta(\theta,t)}{2\pi}(\cos^2\theta + 2\sin^2\theta\sin^2\phi)\, d\Omega, \tag{1.61}$$

$$= \sigma_{12}N_1 \int_0^\pi g_\theta(\theta,t)\sin\theta\, d\theta, \tag{1.62}$$

$$= \sigma_{12}N_1. \tag{1.63}$$

This definition of the isotropic signal ensures that all the equations introduced in the previous paragraphs remain valid if $\Delta\alpha$ denotes the isotropic signal. The isotropic signal reflects the dynamics due to vibrational relaxation and spectral diffusion but is independent of any orientational processes.

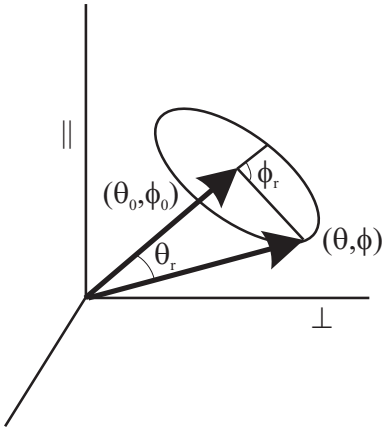

FIGURE 1.19. Polar coordinates used to define the initial and final orientations of a dipole. The coordinates (θ_r, ϕ_r) are defined relative to the initial coordinates (θ_0, ϕ_0).

1.5.2 ANISOTROPY

It has been demonstrated that the difference between the parallel and perpendicular absorption changes contains information about the orientational dynamics of molecules. A quantity that depends *exclusively* on the orientational dynamics is obtained by normalizing this difference to the total signal

$$R(t) = \frac{\Delta\alpha_{||} - \Delta\alpha_{\perp}}{\Delta\alpha_{||} + 2\Delta\alpha_{\perp}}. \tag{1.64}$$

This is the anisotropy, which we shall employ frequently throughout this thesis to study the orientational motion of water molecules.

In terms of the orientational distribution function $g(\theta, \phi, t)$ the anisotropy reads

$$R(t) = \int g(\theta, \phi, t)(\cos^2\theta - \sin^2\theta \sin^2\phi)\, d\Omega. \tag{1.65}$$

This expression shows that the anisotropy does indeed only reflect the orientational motion of molecules, as required. However, as it stands the expression is not very convenient. In the following we will rewrite the expression for the anisotropy in such a way that it reflects the motion of individual molecules. The time-dependence of $g(\theta, \phi, t)$ can be most generally expressed as [11]

$$g(\theta, \phi, t) = \int p(\theta, \phi, t|\theta_0, \phi_0) g(\theta_0, \phi_0, 0)\, d\Omega_0, \tag{1.66}$$

$$= \int p(\theta, \phi, t|\theta_0, \phi_0) \frac{3\cos^2\theta_0}{4\pi}\, d\Omega_0, \tag{1.67}$$

where $p(\theta, \phi, t|\theta_0, \phi_0)$ is the probability that a dipole that had an initial orientation (θ_0, ϕ_0) will have an orientation (θ, ϕ) at time t. $p(\theta, \phi, t|\theta_0, \phi_0)$ is actually

the Green's function solution to the differential equation that describes the orientational motion of the molecules. Substitution into equation 1.65 leads to the complicated expression,

$$R(t) = \int\int p(\theta, \phi, t|\theta_0, \phi_0) \frac{3\cos^2\theta_0}{4\pi} (\cos^2\theta - \sin^2\theta \sin^2\phi)\, d\Omega\, d\Omega_0, \quad (1.68)$$

so that it seems that everything has only become more complex. In an isotropic sample, however, matters simplify because the probability of an angular displacement depends only on the relative angle between the initial and final orientations. To exploit this symmetry we use a new set of polar coordinates (θ_r, ϕ_r) that are defined relative to the initial orientation (θ_0, ϕ_0) (figure 1.19). We change the integration variable from $d\Omega$ to $d\Omega_r$ and obtain

$$R(t) = \int\int p(\theta_r, 0, t|0, 0) f(\theta_0, \phi_0, \theta_r, \phi_r)\, d\Omega_0\, d\Omega_r, \quad (1.69)$$

where $f(\theta_0, \phi_0, \theta_r, \phi_r)$ is the trigonometric function from the previous equation but now expressed in terms of Ω_0 and Ω_r. Because $p(\theta_r, \phi_r, t|0, 0)$ is independent of ϕ_r, we have replaced this variable with 0. Integration over three of the polar coordinates leads to

$$R(t) = \int p(\theta_r) h(\theta_r) \sin\theta_r\, d\theta_r, \quad (1.70)$$

where

$$h(\theta_r) = \int\int\int f(\theta_0, \phi_0, \theta_r, \phi_r)\, d\phi_r\, d\phi_0\, d\theta_0. \quad (1.71)$$

By explicitly carrying out the integration it can be shown that

$$h(\theta_r) = \frac{2}{5} P_2(\cos(\theta_r)), \quad (1.72)$$

where $P_2(x) = (3x^2 - 1)/2$ is the second order Legendre polynomial. We see that the anisotropy can be written as the average over a function of the angular displacement

$$\begin{aligned} R(t) &= \frac{2}{5}\langle P_2(\cos\theta_r)\rangle, & (1.73)\\ &= \frac{2}{5}\langle P_2(\vec{\mu}(0)\cdot\vec{\mu}(t))\rangle, & (1.74)\\ &= \frac{2}{5}\langle(3\cos^2\theta_r - 1)/2\rangle, & (1.75)\\ &= \frac{2}{5} C(t). & (1.76) \end{aligned}$$

Here $C(t)$ is usually referred to as the second order orientational correlation function.[e] We have now shown that the anisotropy is indeed a measure for

[e] It should be noted that different experiments determine different types of correlation functions. NMR and pump-probe spectroscopy provide the second order correlation function, while dielectric relaxation measures the first order correlation function, which is given by $\langle P_1(\cos\theta_r)\rangle = \langle\cos\theta_r\rangle$

the angular displacement of a molecule during the pump-probe delay, as was expected intuitively. It is easy to see that the maximum value of the anisotropy occurs at $t = 0$ and equals $2/5$. For long delays we can write $\langle \cos^2 \theta_r \rangle = 1/3$, which is the isotropic value and we see that the anisotropy vanishes as expected. The importance of the above equations lies in the fact that they relate a macroscopic experimental observable, the anisotropy, to specific microscopic information, in the form of a correlation function.

2 Nonlinear response theory

2.1 Introduction

In the previous chapter the physical principles that form the basis of pump-probe spectroscopy were introduced. Here we provide an alternative description of pump-probe spectroscopy, which is based on the nonlinear response formalism. An advantage of this formalism is that it provides a unified description of all types of nonlinear optical spectroscopy (e.g., pump-probe, photon echo spectroscopy, CARS, etc.); the disadvantage, however, is that it requires the use of rather complex mathematics. In the following a self-contained derivation of the nonlinear response formalism is provided and applied to pump-probe spectroscopy. This derivation is based on the treatments by Boyd [13] and Mukamel [74]. Additional information about nonlinear response theory can be found in refs. [16, 91, 104].

Nonlinear response theory describes the interaction of light with matter by considering the induced optical polarization. As an example, let us consider figure 2.1, in which the linear absorption of light is explained using the optical polarization. The figure depicts an electromagnetic wave that impinges on a material, in which it induces an oscillating polarization. This polarization radiates a new electromagnetic wave that runs out of phase with the original wave. The result is that the two waves interfere destructively, which is an alternative way of expressing the absorption of the radiation by the material. We point out that the radiated field is not merely a mathematical construct but a true field that can be observed by itself. In photon echo spectroscopy, for example, two or three non-colinear optical pulses are used to create a polarization that radiates in a background-free direction.

2.2 Perturbation expansion of the polarization

Nonlinear response theory starts by expanding the induced polarization in powers of the electric field of the incident radiation

$$P(t) = P^{(1)}(t) + P^{(2)}(t) + P^{(3)}(t) + \dots \tag{2.1}$$

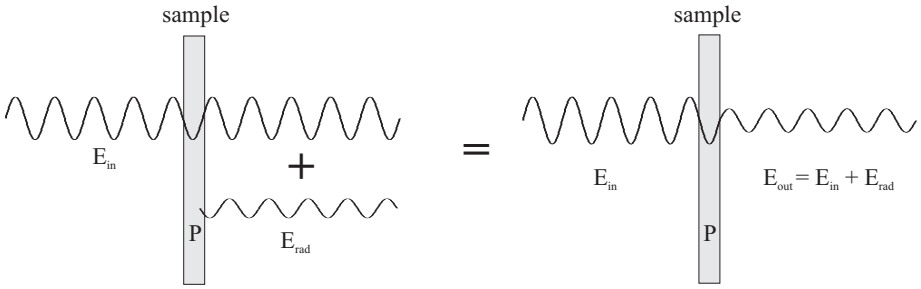

FIGURE 2.1. Linear absorption of light described through the induced polarization. An electromagnetic wave induces an oscillating polarization in a material. The polarization radiates a secondary wave that is out of phase with the original wave. Absorption arises due to the destructive interference of the two waves.

were $P^{(1)}(t)$ depends linearly on E, $P^{(2)}(t)$ quadratically, etc.[a] It turns out that $P^{(1)}(t)$ is responsible for linear absorption and that $P^{(3)}(t)$ is the term that describes the pump-probe response. The polarization is calculated quantum mechanically using the density matrix formalism [13, 14, 74]. Once the density matrix $\hat{\rho}(t)$ of the system is known the polarization is obtained by

$$P(t) = \mathrm{Tr}\left(\hat{\mu}\hat{\rho}(t)\right), \tag{2.2}$$

where Tr denotes the trace operation. The density matrix is partitioned in the same way as the polarization

$$\hat{\rho}(t) = \hat{\rho}^{(1)}(t) + \hat{\rho}^{(2)}(t) + \hat{\rho}^{(3)}(t) + \ldots, \tag{2.3}$$

so that the n^{th} order polarization is given by

$$P^{(n)}(t) = \mathrm{Tr}\left(\hat{\mu}\hat{\rho}^{(n)}(t)\right). \tag{2.4}$$

The evolution of the density matrix is governed by the Liouville equation

$$\frac{d}{dt}\hat{\rho} = -\frac{i}{\hbar}\left[\hat{H}, \hat{\rho}\right], \tag{2.5}$$

where the Hamiltonian $\hat{H}$ is given by the sum of the unperturbed Hamiltonian $\hat{H}_0$ and the perturbation due to the incident radiation

$$\hat{H} = \hat{H}_0 + \hat{V}(t), \tag{2.6}$$

$$= \hat{H}_0 - \hat{\mu}E(t). \tag{2.7}$$

The effects of relaxation are not yet described by eqn. 2.5; it is common to incorporate these effects phenomenologically. To this end we write out the

[a] It is incorrect to write $P^{(1)}(t) \propto E(t)$, $P^{(2)}(t) \propto E^2(t)$, etc., because the polarization at time t does not only depend on the electric field at time t but also on the electric field at times prior to t.

Liouville equation for a single density matrix element, in the absence of any perturbation,

$$\frac{d}{dt}\rho_{nm} = -i\omega_{nm}\rho_{nm}. \tag{2.8}$$

This equation leads to oscillatory solutions for the off-diagonal matrix elements (coherences) and to time-independent solutions for the diagonal elements (populations). The populations and coherences are generally assumed to decay exponentially and this can be incorporated into the Liouville equation by modifying it to

$$\frac{d}{dt}\rho_{nm} = -i\omega_{nm}\rho_{nm} - \gamma_{nm}(\rho_{nm} - \rho_{nm}^{(\mathrm{eq})}) - \frac{i}{\hbar}\left[\hat{V},\hat{\rho}\right]_{nm}, \tag{2.9}$$

where $\rho_{nm}^{(\mathrm{eq})}$ is the equilibrium value of ρ_{nm}, γ_{nn} is the population relaxation rate of state n and γ_{nm} $(n \neq m)$ is the dephasing rate of the $n \rightarrow m$ transition. In equilibrium the off-diagonal density matrix elements vanish

$$\rho_{nm}^{(\mathrm{eq})} = 0 \text{ for } n \neq m. \tag{2.10}$$

Eqn. 2.9 can be solved by inserting the expansion from eqn. 2.3 into it and collecting terms that depend on the same order of E. We thus obtain the following set of coupled differential equations

$$\begin{aligned}
\frac{d}{dt}\rho_{nm}^{(0)} &= -i\omega_{nm}\rho_{nm}^{(0)} - \gamma_{nm}(\rho_{nm}^{(0)} - \rho_{nm}^{(\mathrm{eq})}),\\
\frac{d}{dt}\rho_{nm}^{(1)} &= (-i\omega_{nm} - \gamma_{nm})\rho_{nm}^{(1)} - \frac{i}{\hbar}\left[\hat{V},\hat{\rho}^{(0)}\right]_{nm},\\
\frac{d}{dt}\rho_{nm}^{(2)} &= (-i\omega_{nm} - \gamma_{nm})\rho_{nm}^{(2)} - \frac{i}{\hbar}\left[\hat{V},\hat{\rho}^{(1)}\right]_{nm},\\
&\vdots \qquad\qquad\qquad \vdots\\
\frac{d}{dt}\rho_{nm}^{(q)} &= (-i\omega_{nm} - \gamma_{nm})\rho_{nm}^{(q)} - \frac{i}{\hbar}\left[\hat{V},\hat{\rho}^{(q-1)}\right]_{nm}.
\end{aligned}$$

These equations can be solved successively if we start with $\rho_{nm}^{(0)} = \rho_{nm}^{(\mathrm{eq})}$. Using the method of variation of constants $\rho^{(q)}(t)$ can be expressed in terms of $\rho^{(q-1)}(t)$,

$$\begin{aligned}
\rho_{nm}^{(q)}(t) &= \frac{i}{\hbar}\int_{-\infty}^{t} dt' e^{(-i\omega_{nm}-\gamma_{nm})(t-t')}E(t')\left[\hat{\mu},\hat{\rho}^{(q-1)}(t')\right]_{nm},\\
&= \frac{i}{\hbar}\int_{-\infty}^{t} dt' I_{nm}(t-t')E(t')\left[\hat{\mu},\hat{\rho}^{(q-1)}(t')\right]_{nm},
\end{aligned} \tag{2.11}$$

where we have used $\hat{V} = -\hat{\mu}E$ and introduced the auxiliary functions $I_{nm}(t)$,

$$I_{nm}(t) = e^{-i\omega_{nm}t-\gamma_{nm}t}. \tag{2.12}$$

Our goal is to obtain an expression for $P^{(3)}(t)$, as this is the term that describes the pump-probe response; to do this we need the expression for $\rho^{(3)}(t)$.

The simplest way to obtain this expression is to start out with eqn. 2.11 with $q = 3$ and to successively substitute the expressions for the lower order density matrix elements. It is clear that this procedure will lead to a very complex expression. Fortunately, it turns out that there is a systematic method for deriving this expression that yields more insight. Before applying the method to higher order polarizations we first start by illustrating it for the first order polarization.

2.3 First order polarization

Definition of the response function By expanding the commutator in eqn. 2.11 we obtain the following expression for the first order density matrix elements

$$\rho^{(1)}_{nm}(t) = \frac{i}{\hbar}\int_{-\infty}^{t} dt' I_{nm}(t-t')E(t')\sum_a \left(\mu_{na}\rho^{(0)}_{am} - \rho^{(0)}_{na}\mu_{am}\right), \tag{2.13}$$

where we have dropped the explicit time-dependence of $\hat{\rho}^{(0)}$ as it is time-independent. Because $\hat{\rho}^{(0)}$ is diagonal the summation reduces to a single term

$$\rho^{(1)}_{nm}(t) = \frac{i}{\hbar}\int_{-\infty}^{t} dt' I_{nm}(t-t')E(t')\left(\mu_{nm}\rho^{(0)}_{mm} - \rho^{(0)}_{nn}\mu_{nm}\right). \tag{2.14}$$

Eqns 2.2 and 2.14 lead to the following expression for the linear polarization

$$\begin{aligned} P^{(1)}(t) &= \sum_{nm}\mu_{mn}\rho^{(1)}_{nm}(t), & (2.15)\\ &= \frac{i}{\hbar}\int_{-\infty}^{t} d\tau_1 E(\tau_1)\sum_{nm} I_{nm}(t-\tau_1)|\mu_{nm}|^2\left(\rho^{(0)}_{mm} - \rho^{(0)}_{nn}\right), \\ &= \frac{i}{\hbar}\int_{-\infty}^{t} d\tau_1 E(\tau_1)\mathcal{S}^{(1)}(t,\tau_1). & (2.16) \end{aligned}$$

For future convenience, we have changed the integration variable from t' to τ_1. The first order response function has been defined as

$$\mathcal{S}^{(1)}(t,\tau_1) = \sum_{nm} I_{nm}(t-\tau_1)|\mu_{nm}|^2\left(\rho^{(0)}_{mm} - \rho^{(0)}_{nn}\right). \tag{2.17}$$

This function contains all information that is needed to compute any linear optical property of a material system, such as one-photon absorption and refraction. Higher order response functions also exist and these describe nonlinear optical phenomena, for instance two photon absorption and second harmonic generation. Since all information about a material is contained in its response functions, they play a central role in (non)linear spectroscopy.

DIAGRAMMATIC NOTATION FOR THE RESPONSE FUNCTION Eqn 2.17 has a relatively simple form but we will see that the higher order response functions increase in complexity. It will be convenient to introduce a systematic method to derive these functions. Below we demonstrate this method for the first order response function. In the following section the method will be generalized for the higher order response functions.

We begin by shifting the summation in eqn. 2.13 to the front to obtain

$$\begin{aligned}\rho^{(1)}_{nm}(t) &= \sum_a \frac{i}{\hbar}\int_{-\infty}^{t} dt' I_{nm}(t-t')E(t')\mu_{na}\rho^{(0)}_{am} \qquad (2.18)\\ &\quad -\sum_a \frac{i}{\hbar}\int_{-\infty}^{t} dt' I_{nm}(t-t')E(t')\rho^{(0)}_{na}\mu_{am},\\ &= \sum_a \rho^{(1)}_{nm\leftarrow am}(t) + \sum_a \rho^{(1)}_{nm\leftarrow na}(t). \qquad (2.19)\end{aligned}$$

In the last line we have separated the expression for $\rho^{(1)}_{nm}$ into contributions originating in the different elements of $\hat{\rho}^{(0)}$. The subscript $nm \leftarrow am$ refers to the contribution to $\rho^{(1)}_{nm}$ that is due to $\rho^{(0)}_{am}$. An important observation is that an element of $\hat{\rho}^{(0)}$ only contributes to an element of $\hat{\rho}^{(1)}$ if both elements have at least one index in common. In other words, the two elements must lie in either the same row or in the same column. Since $\rho^{(0)}$ is diagonal the previous expression simplifies to

$$\rho^{(1)}_{nm}(t) = \rho^{(1)}_{nm\leftarrow mm}(t) + \rho^{(1)}_{nm\leftarrow nn}(t), \qquad (2.20)$$

which is another way of writing eqn. 2.14.

Up to now we have been working downward in the perturbation expansion of $\hat{\rho}(t)$. That is, we have started with $\rho^{(1)}_{nm}(t)$ and considered the lower order elements that contribute to this element. It turns out that, especially when working with higher order response functions, it is convenient start at the other end and work upward in the perturbation expansion. This means that we start with a specific zeroth order element, $\rho^{(0)}_{aa}$, and consider the higher order elements to which this element contributes. As $\rho^{(0)}_{aa}$ only contributes to elements in the same row or column, we obtain the following expressions

$$\rho^{(1)}_{ba\leftarrow aa}(t) = \frac{i}{\hbar}\int_{-\infty}^{t} d\tau_1 I_{ba}(t-\tau_1)E(\tau_1)\mu_{ba}\rho^{(0)}_{aa}, \qquad (2.21)$$

$$\rho^{(1)}_{ab\leftarrow aa}(t) = -\frac{i}{\hbar}\int_{-\infty}^{t} d\tau_1 I_{ab}(t-\tau_1)E(\tau_1)\rho^{(0)}_{aa}\mu_{ab}. \qquad (2.22)$$

In figure 2.2 we have illustrated these coherence pathways graphically. We see that there are two types of pathways: those that connect elements in the horizontal direction and those that connect in the vertical direction. Let us

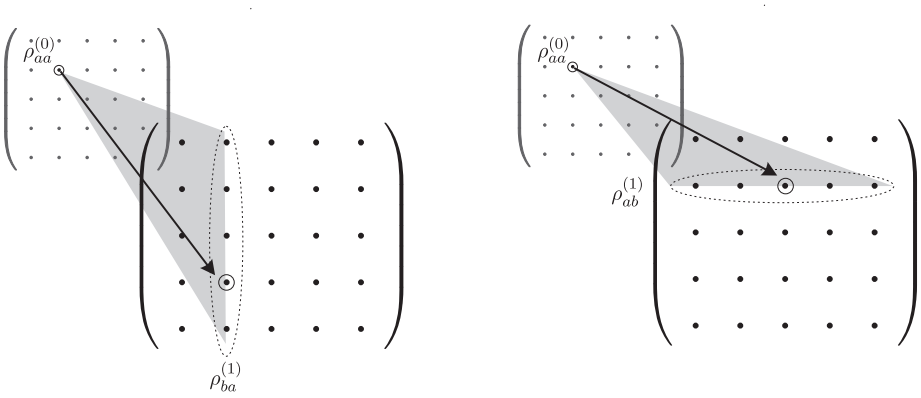

FIGURE 2.2. The two types of coherence pathways that contribute to the first order response function.

consider how these pathways contribute to the response function,

$$\mathcal{S}^{(1)}_{ba\leftarrow aa}(t,\tau_1) = I_{ba}(t-\tau_1)|\mu_{ba}|^2\rho^{(0)}_{aa}, \tag{2.23}$$

$$\mathcal{S}^{(1)}_{ab\leftarrow aa}(t,\tau_1) = -I_{ab}(t-\tau_1)|\mu_{ba}|^2\rho^{(0)}_{aa}, \tag{2.24}$$

where the subscripts are used to denote a specific part of the response function. In order to obtain the full response function we have to sum over all possible initial states $\rho^{(0)}_{aa}$ and final states $\rho^{(1)}_{ab}$,

$$\begin{aligned}\mathcal{S}(t,\tau_1) &= \sum_{ab} \mathcal{S}^{(1)}_{ba\leftarrow aa}(t,\tau_1) + \mathcal{S}^{(1)}_{ab\leftarrow aa}(t,\tau_1) \\ &= \sum_{ab} I_{ba}(t-\tau_1)|\mu_{ba}|^2\rho^{(0)}_{aa} - \sum_{ab} I_{ab}(t-\tau_1)|\mu_{ba}|^2\rho^{(0)}_{aa}.\end{aligned} \tag{2.25}$$

The two terms appearing in this equation have been represented graphically in figure 2.3. We will refer to these diagrams as response diagrams, to distinguish them from double-sided Feynman diagrams, which are extensively used in the literature on nonlinear optics and which will be introduced in the next section. Our response diagrams are in fact simplified Feynman diagrams that do not yet take into account the electric field. Two response diagrams are needed to represent the first order response function, four for the second order response function, eight for the third order response function, etc. The diagrams represent the perturbation expansion going from the bottom to the top. Every set of indices represents a density matrix element, except for upper set. As an illustration of the use of these diagrams, the figure demonstrates how the response function can be constructed with the help of these diagrams. At this point, this merely serves as an example; in the next section we will provide a set of systematic rules for converting response diagrams to equations.

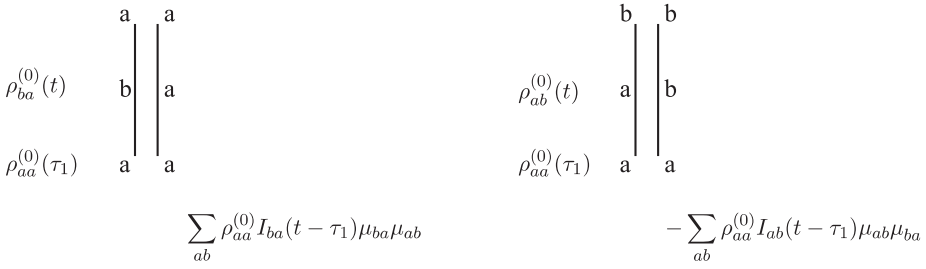

FIGURE 2.3. Response diagrams for the first order response function. The mathematical expressions corresponding to these diagrams are also given.

2.4 THIRD ORDER POLARIZATION

DEFINITION OF THE THIRD ORDER RESPONSE FUNCTION We can use the expression obtained for $\hat{\rho}^{(1)}(t)$ to continue the perturbation expansion and obtain expressions for $\hat{\rho}^{(2)}(t)$ and $\hat{\rho}^{(3)}(t)$. We note that when successively inserting the expressions for the different orders of the density matrix into eqn. 2.11, the integrals can be shifted to the end. For the third order polarization an equation of the following form is obtained

$$P^{(3)}(t) = \left(\frac{i}{\hbar}\right)^3 \int_{-\infty}^{t} d\tau_3 \int_{-\infty}^{\tau_3} d\tau_2 \int_{-\infty}^{\tau_2} d\tau_1 \mathcal{S}^{(3)}(t,\tau_3,\tau_2,\tau_1) E(\tau_3) E(\tau_2) E(\tau_1), \quad (2.26)$$

where $\mathcal{S}^{(3)}(t,\tau_3,\tau_2,\tau_1)$ is the third order response function. In writing this equation we have used the following integration variables for the different orders of the density matrix

$$\rho^{(3)}(t), \qquad \rho^{(2)}(\tau_3), \qquad \rho^{(1)}(\tau_2), \qquad \rho^{(0)}(\tau_1). \quad (2.27)$$

DIAGRAMMATIC NOTATION We now proceed in the same way as we did for the first order response function and separate the third order response function into its constituent coherence pathways. Since every time we move up one order in the perturbation expansion we either make a vertical or a horizontal transition in the density matrix, there are eight coherence pathways that contribute to the third order response function. Figure 2.4 gives a graphic example of one of these pathways.

In order to derive the expression for the coherence pathway shown in this figure, we continue the perturbation expansion where we left off in the previous section and consider the elements to which $\rho^{(1)}_{ab}$ contributes. It is readily seen

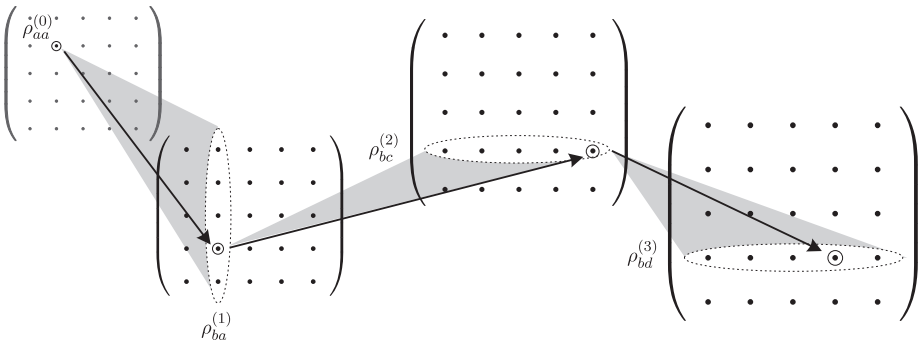

FIGURE 2.4. One of the pathways contributing to the third order response function.

that there are again two types of elements,

$$\rho_{cb\leftarrow ab}^{(2)}(\tau_3) = \frac{i}{\hbar}\int_{-\infty}^{\tau_2} d\tau_2 I_{cb}(\tau_3-\tau_2)E(\tau_2)\mu_{ca}\rho_{ab}^{(1)}(\tau_2), \tag{2.28}$$

$$\rho_{ac\leftarrow ab}^{(2)}(\tau_3) = -\frac{i}{\hbar}\int_{-\infty}^{\tau_2} d\tau_2 I_{ac}(\tau_3-\tau_2)E(\tau_2)\rho_{ab}^{(1)}(\tau_2)\mu_{bc}. \tag{2.29}$$

At this point one should realize that all factors appearing in these expressions will, later on, also appear in the expression for the third order response function. Therefore it is possible to generally state that the transition $\rho_{ab}^{(1)} \rightarrow \rho_{cb}^{(2)}$ adds a factor $I_{cb}(\tau_3-\tau_2)\mu_{ca}$ to the response function. Similarly, the transition $\rho_{ab}^{(1)} \rightarrow \rho_{ac}^{(2)}$ adds a factor $-I_{ac}(\tau_3-\tau_2)\mu_{bc}$. Continuing along this line we can identify all factors that appear in the third order response function and obtain the full expressions for the eight coherence pathways that make up this response function. Figure 2.5 represents four of the eight coherence pathways graphically. The first diagram is used as an example to demonstrate how these diagrams can converted into mathematical expressions. The remaining four diagrams are not displayed since they correspond to the complex conjugate of the diagrams that are shown.

As an example we demonstrate below how the response function for the first diagram is derived:

1. The first index pair adds the factor $\rho_{aa}^{(0)}$ to the response function.

2. The next three index pairs add the factors $I_{ba}(t_1)$, $I_{bc}(t_2)$ and $I_{bd}(t_3)$. Here t_n stands for $\tau_{n+1}-\tau_n$. Note that the last set of indices does not add any factor to the response function.

3. Generally, the transition $\rho_{pq}^{(n-1)} \rightarrow \rho_{rq}^{(n)}$, in which the left-hand index is permuted, adds a factor μ_{rp}. Similarly, the transition $\rho_{pq}^{(n-1)} \rightarrow \rho_{pr}^{(n)}$, in

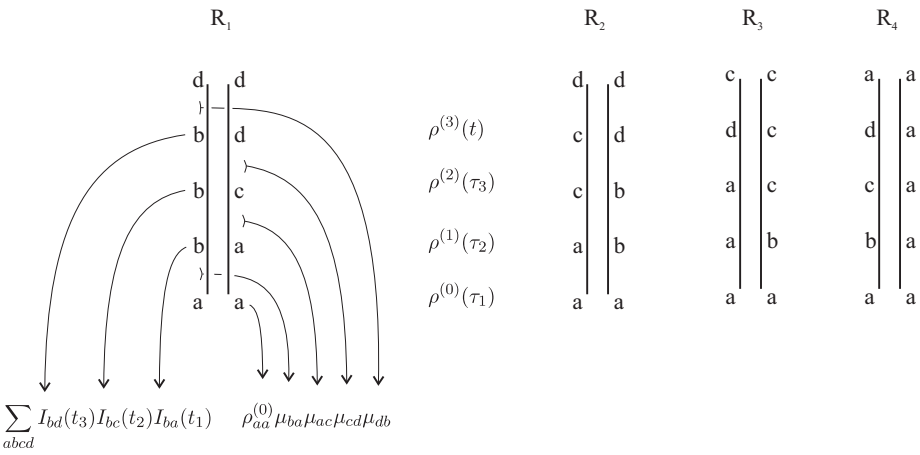

FIGURE 2.5. Response diagrams that contribute to the third order response function. The first diagram illustrates how one can obtain the mathematical expression for the response function.

which the right-hand index is permuted, adds a factor μ_{qr}.[b] In the example above the first transition thus adds a factor μ_{ba}, the second a factor μ_{ac}, and the third a factor μ_{cd}.

4. The upper index pair is different from the other pairs because it does not represent a density matrix element in the perturbation expansion. It is added to account for the trace operation, which adds a factor μ_{db}. The advantage of this notation is that, in the diagram, μ_{db} is represented as arising from the transition $bd \rightarrow dd$.

5. Every interaction that permutes a right-hand index adds a factor of -1 to the response function. In this example this leads to an overall multiplication by 1 as there are two such interactions.

6. In the end the sum over all indices is taken.

TRANSFORMATION OF THE TIME VARIABLES The integral in eqn. 2.26 is called a time-ordered integral because the integration variables are ordered according to

$$\tau_1 \leq \tau_2 \leq \tau_3 \leq t \tag{2.30}$$

Because $\mathcal{S}^{(3)}(t, \tau_3, \tau_2, \tau_1)$ depends only on the time intervals $\tau_n - \tau_{n-1}$ it is sometimes more convenient to make a change of variables and use the intervals t_n,

$$t_3 = t - \tau_3, \qquad t_2 = \tau_3 - \tau_2, \qquad t_1 = \tau_2 - \tau_1. \tag{2.31}$$

[b] This is reminiscent of the contraction of indices as it is encountered in matrix multiplication: $\mu_{rp}\rho^{(n-1)}_{pq} \rightarrow \rho^{(n)}_{rq}$ and $\rho^{(n-1)}_{pq}\mu_{qr} \rightarrow \rho^{(n)}_{pr}$.

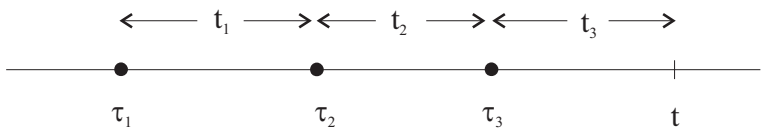

FIGURE 2.6. Transformation between the time variables (τ_1, τ_2, τ_3) and the time intervals (t_1, t_2, t_3).

This transformation is illustrated in figure 2.6. In terms of these variables the third order polarization reads

$$P^{(3)}(t) = \left(\frac{i}{\hbar}\right)^3 \int_0^\infty dt_3 \int_0^\infty dt_2 \int_0^\infty dt_1 S^{(3)}(t_3, t_2, t_1) \\ E(t - t_3)E(t - t_3 - t_2)E(t - t_3 - t_2 - t_1), \quad (2.32)$$

in which $S^{(3)}(t_3, t_2, t_1)$ can be written as a sum over the four response functions from figure 2.5 and their complex conjugates,

$$S^{(3)}(t_3, t_2, t_1) = \left(\frac{i}{\hbar}\right)^3 \sum_{\alpha=1}^{4} [R_\alpha(t_3, t_2, t_1) - R_\alpha^*(t_3, t_2, t_1)]. \quad (2.33)$$

The expressions for these response functions are given by

$$R_1(t_3, t_2, t_1) = \sum_{abcd} \rho_{aa}^{(0)} \mu_{db}\mu_{cd}\mu_{ac}\mu_{ba} I_{bd}(t_3) I_{bc}(t_2) I_{ba}(t_1), \quad (2.34)$$

$$R_2(t_3, t_2, t_1) = \sum_{abcd} \rho_{aa}^{(0)} \mu_{dc}\mu_{bd}\mu_{ca}\mu_{ab} I_{cd}(t_3) I_{cb}(t_2) I_{ab}(t_1), \quad (2.35)$$

$$R_3(t_3, t_2, t_1) = \sum_{abcd} \rho_{aa}^{(0)} \mu_{cd}\mu_{da}\mu_{bc}\mu_{ab} I_{dc}(t_3) I_{ac}(t_2) I_{ab}(t_1), \quad (2.36)$$

$$R_4(t_3, t_2, t_1) = \sum_{abcd} \rho_{aa}^{(0)} \mu_{ad}\mu_{dc}\mu_{cb}\mu_{ba} I_{da}(t_3) I_{ca}(t_2) I_{ba}(t_1). \quad (2.37)$$

2.5 RESPONSE FUNCTIONS APPLIED TO PUMP-PROBE SPECTROSCOPY

Eqns 2.32-2.37 provide all information necessary to compute the third order response of a system that is exposed to an arbitrary electric field; one only needs to know the transition frequencies ω_{nm} and the transition dipole moments μ_{nm}. In the case of pump-probe spectroscopy the field consists of two pulses separated by a delay τ,

$$E(t) = E_1(t) + E_2(t), \quad (2.38)$$

$$= \mathcal{E}_1(t) e^{-i\omega_1 t + i\vec{k}_1 \cdot \vec{r}} + \mathcal{E}_2(t) e^{-i\omega_2 t + i\vec{k}_2 \cdot \vec{r}} + c.c., \quad (2.39)$$

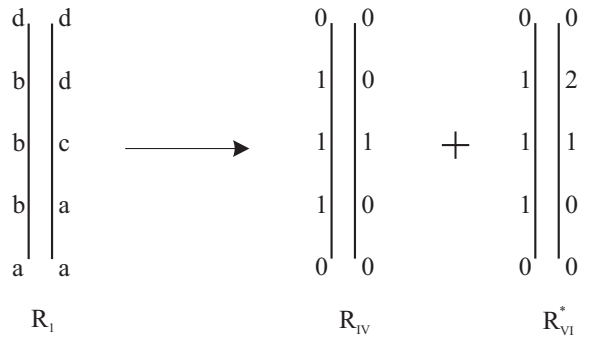

FIGURE 2.7. The result of carrying out the summation for response diagram R_1. The labeling of the resulting diagrams is done for future convenience.

where $E_1(t)$ represents the pump field and $E_2(t)$ the probe field. $\mathcal{E}_1(t)$ and $\mathcal{E}_2(t)$ are the electric field envelopes.

Above it was shown that the third order response function contains eight terms. The electric field, in addition, contains four terms, so that the most general expression for the pump-probe response will contain $8 \times 4^3 = 256$ terms, each of which is composed of a large number of terms due to the dimension of the density matrix. Fortunately the majority of the terms can be disregarded because of a number of approximations that will be made.

HARMONIC APPROXIMATION FOR A THREE-LEVEL SYSTEM The first simplification occurs if we consider only three levels, i.e. the system's ground state, the first excited state and the second excited state. In the harmonic approximation μ_{nm} is only non-zero for $n = m \pm 1$, so that the summations in eqns. 2.34-2.37 reduce to only a few terms. Figure 2.7 illustrates this for R_1.

DIRECTIONS OF THE RADIATED FIELD Next we consider combinations of the fields with the response functions. Many of these combinations lead to polarizations that radiate in directions other than that of the probe. For example, the combination $E_2^*(t-t_3)E_1(t-t_3-t_2)E_1(t-t_3-t_2-t_1)$ has a position dependence of the form $\exp[i(2\vec{k}_1 - \vec{k}_2)\cdot\vec{r}]$, and therefore generates an electromagnetic wave in the direction $2\vec{k}_1 - \vec{k}_2$. This type of field combination does not contribute to the pump-probe response but rather generates a signal that is known as a photon echo. Clearly, in the case of pump-probe spectroscopy we only need to consider combinations that radiate in the direction $\vec{k}_2$. These only arise due the field combinations $E_1E_1^*E_2$ and $E_2E_2^*E_2$. Since the probe intensity is much lower than the pump-intensity, the latter field combination is generally not considered.

ROTATING WAVE APPROXIMATION (RWA) As a final step we make the rotating wave approximation. In this approximation all combinations of fields and diagrams are neglected that lead to rapidly oscillating terms in the in-

tegrand of eqn. 2.32. As an example let us consider the field permutation $E_2(t-t_3)E_1(t-t_3-t_2)E_1^*(t-t_3-t_2-t_1)$ combined with the response function R_{IV} (figure 2.7). By writing out this term it can be seen that it contributes the following factors to the integrand[c]

$$\exp[i(\omega_1-\omega_{10})t_1], \tag{2.40}$$
$$\exp[i(\omega_1-\omega_1-\omega_{11})t_2] = 1, \tag{2.41}$$
$$\exp[i(\omega_1-\omega_1-\omega_2+\omega_{10})]t_3 = \exp[-i(\omega_2-\omega_{10})t_3]. \tag{2.42}$$

We see that all of these terms oscillate slowly, and therefore they survive the RWA. The combination $E_1(t-t_3)E_1^*(t-t_3-t_2)E_2(t-t_3-t_2-t_1)$, on the other hand, leads to the following terms

$$\exp[-i(\omega_2+\omega_{10})t_1], \tag{2.43}$$
$$\exp[-i(\omega_2-\omega_1-\omega_{11})t_2] = \exp[-i(\omega_2-\omega_1)t_2], \tag{2.44}$$
$$\exp[-i(\omega_2-\omega_1+\omega_1+\omega_{10})t_3] = \exp[-i(\omega_2-\omega_{10})t_3]. \tag{2.45}$$

Clearly the t_1 term is a rapidly oscillating term, and therefore we disregard the combination of this field permutation and response function R_{IV}. Continuing in this way we can find all permitted combinations of response diagrams and field permutations that survive the RWA. These are displayed in figure 2.8. Such combinations of response diagrams and fields are known as double-sided Feynman diagrams. In these diagrams wavy arrows represent field components. A solid arrow to the right represents a field $\mathcal{E}_j(t)\exp[-i\omega_j t+i\vec{k}_j\cdot\vec{r}]$ and one to the left represents a field $\mathcal{E}_j^*(t)\exp[i\omega_j t-i\vec{k}_j\cdot\vec{r}]$. The dashed arrow represents the radiated field. On the left hand of the diagrams the explicit field permutations are given for each group of diagrams. The mathematical expressions for the response diagrams from figure 2.8 are given below

$$\begin{aligned}
R_{\mathrm{I}}(t_3,t_2,t_1) &= |\mu_{01}|^4 I_{10}(t_3)I_{11}(t_2)I_{01}(t_1),\\
R_{\mathrm{II}}(t_3,t_2,t_1) &= R_{\mathrm{I}}(t_3,t_2,t_1),\\
R_{\mathrm{III}}(t_3,t_2,t_1) &= -|\mu_{01}|^2|\mu_{12}|^2 I_{21}(t_3)I_{11}(t_2)I_{01}(t_1),\\
R_{\mathrm{IV}}(t_3,t_2,t_1) &= |\mu_{01}|^4 I_{10}(t_3)I_{11}(t_2)I_{10}(t_1),\\
R_{\mathrm{V}}(t_3,t_2,t_1) &= R_{\mathrm{IV}}(t_3,t_2,t_1),\\
R_{\mathrm{VI}}(t_3,t_2,t_1) &= -|\mu_{01}|^2|\mu_{12}|^2 I_{21}(t_3)I_{11}(t_2)I_{10}(t_1),\\
R_{\mathrm{VII}}(t_3,t_2,t_1) &= |\mu_{01}|^2|\mu_{12}|^2 I_{10}(t_3)I_{20}(t_2)I_{10}(t_1),\\
R_{\mathrm{VIII}}(t_3,t_2,t_1) &= -|\mu_{01}|^2|\mu_{12}|^2 I_{21}(t_3)I_{20}(t_2)I_{10}(t_1).
\end{aligned}$$

These diagrams describe the full pump-probe signal, including coherent artifacts. Since each response function can be combined with two field permutations, there are a total of 16 terms contributing to the pump-probe signal. Ten of these correspond to coherent artifacts; that is, all terms in which the probe

[c]This can be seen by using eqn. 2.34 with $a=0$, $b=1$, $c=1$ and $d=0$, and the expressions for E_1 and E_2 from eqn. 2.39.

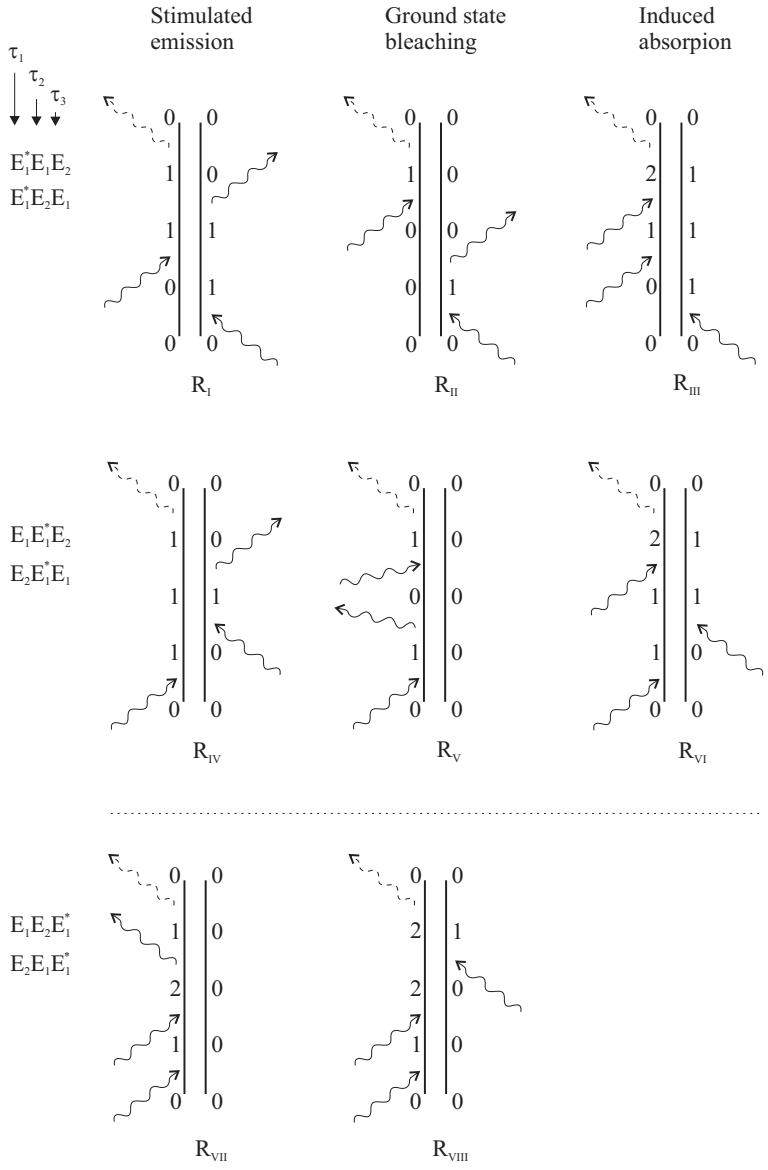

FIGURE 2.8. Feynman diagrams relevant for the pump-probe spectroscopy of a three-level system.

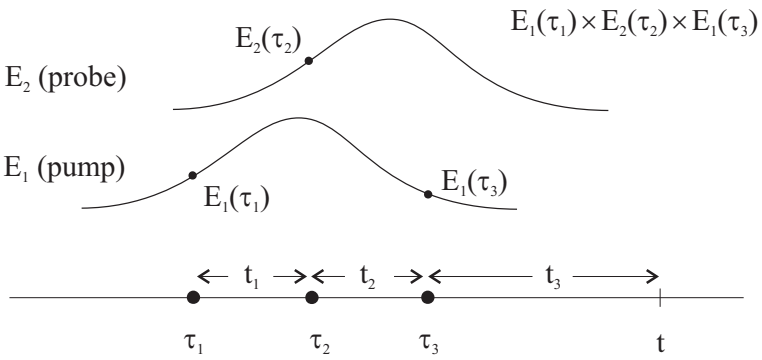

FIGURE 2.9. Field permutations in which the probe interaction comes before the pump interaction can only contribute to the integral in eqn. 2.32 when the pump and probe pulses overlap.

interaction comes before at least one of the two pump interactions. These terms only have a non-vanishing contribution when pump and probe overlap as is explained in figure 2.9. The six remaining terms represent the stimulated emission ($R_{\mathrm{I}}, R_{\mathrm{IV}}$), the ground state bleaching ($R_{\mathrm{II}}, R_{\mathrm{V}}$) and the induced absorption ($R_{\mathrm{III}}, R_{\mathrm{VI}}$). Finally we see that there are two diagrams ($R_{\mathrm{VII}}, R_{\mathrm{VIII}}$) that do contribute to the pump-probe signal but that were not identified in the previous sections. These describe contributions to the third order polarization via a $0 \rightarrow 2$ coherence.

The coherent artifacts referred to above arise due to the part of the density matrix that is resonant with the radiation. The cross-phase modulation artifact, which was described in section 1.3.4, is a different type of artifact that arises due to the non-resonant part of the density matrix (which we have neglected here since we are only considering a three-level system). The non-resonant part of the response function, which can be used to calculate this artifact is, to first approximation instantaneous, and is described by

$$S^{(3)}_{\mathrm{nonres}}(t_3, t_2, t_1) \propto \delta(t_3)\delta(t_2)\delta(t_1). \tag{2.46}$$

2.5.1 DETECTION

In order to be able to simulate a pump-probe response from the third order polarization, we need to know how the radiated field depends on the polarization. It can be shown [74] that the oscillating polarization $P^{(3)}(t)$ radiates an electric field of the form

$$E_{\mathrm{rad}}(t) \propto iP^{(3)}(t). \tag{2.47}$$

In pump-probe spectroscopy the experimental conditions are such that the signal field interferes with the probe beam. If we spectrally disperse the probe beam and divide the transmitted probe intensity by the original intensity we

obtain

$$\frac{I}{I_0} = \frac{|\tilde{E}_2(\omega) + i\tilde{P}^{(3)}(\omega)|^2}{|\tilde{E}_2(\omega)|^2}, \tag{2.48}$$

$$\approx 1 - \frac{2\mathrm{Im}(\tilde{P}^{(3)}(\omega)\tilde{E}_2^*(\omega))}{|\tilde{E}_2(\omega)|^2}, \tag{2.49}$$

where $\tilde{E}_2(\omega)$ and $\tilde{P}^{(3)}(\omega)$ are the Fourier transforms of $E_2(t)$ and $P^{(3)}(t)$, respectively. For the absorption change we obtain

$$\Delta\alpha(\omega) = \frac{2\mathrm{Im}\left(\tilde{P}^{(3)}(\omega)\tilde{E}_2^*(\omega)\right)}{|\tilde{E}_2(\omega)|^2}. \tag{2.50}$$

2.6 Inhomogeneous broadening and spectral diffusion

The expression for the third order polarization refers to a single, homogeneously broadened transition. We can include inhomogeneous broadening in the expression by integrating the response function over different transition frequencies. We can, for example, imagine the transition frequencies to depend on an external coordinate Γ, so that we write $\omega_{nm} = \omega_{nm}(\Gamma)$. The inhomogeneous response function can be obtained by integrating over the distribution function $W(\Gamma)$

$$S_{\mathrm{inhom}}(t_3, t_2, t_1) = \int d\Gamma S_\Gamma(t_3, t_2, t_1) W(\Gamma). \tag{2.51}$$

In this approach, both homogeneous and inhomogeneous broadening are treated phenomenologically. A different, more elegant method exist that treats homogeneous and inhomogeneous broadening on the same footing, i.e. both as being the consequence of spectral diffusion. According to this picture rapid fluctuations of the transition frequencies (with respect to the lifetime of a level) are responsible for homogeneous broadening and slow fluctuations for inhomogeneous broadening. The expression for the first order response remains very similar to the expression we have already obtained. We only need to replace the time-independent ω_{nm} by a stochastic function of time

$$\omega_{nm} \rightarrow \omega_{nm}(t) = \langle\omega_{nm}\rangle + \delta\omega_{nm}(t). \tag{2.52}$$

Because the auxiliary functions $I_{nm}(t-\tau_1)$ depend on ω_{nm} (eqn. 2.2), they are also modified

$$I_{nm}(t-\tau_1) \rightarrow \langle J_{nm}(t-\tau_1)\rangle = \left\langle e^{-i\int_{\tau_1}^{t}\omega_{nm}(t')\,dt'}\right\rangle, \tag{2.53}$$

where J_{nm} is the stochastic version of I_{nm} and $\langle\cdots\rangle$ denotes an ensemble average.[d] A useful approximation of this expression can be obtained by making

[d] Because ω_{nm} is a stationary function, J_{nm} depends only on the time difference $t-\tau_1$.

use of the cumulant expansion[e]

$$\langle J_{nm}(t-\tau_1)\rangle = e^{-i\langle\omega_{nm}\rangle(t-\tau_1)-g(t-\tau_1)}, \tag{2.56}$$

where $g(t)$ is given by

$$g(t) = \frac{1}{2}\int_0^t dt' \int_0^t dt'' \langle\delta\omega_{nm}(t')\delta\omega_{nm}(t'')\rangle. \tag{2.57}$$

This expression can be rewritten by making a substitution of the time variables,

$$g(t) = \int_0^t dt' \int_0^{t'} d\tau \langle\delta\omega_{nm}(0)\delta\omega_{nm}(\tau)\rangle, \tag{2.58}$$

$$= \int_0^t dt' \int_0^{t'} d\tau C(\tau), \tag{2.59}$$

where the frequency correlation function is defined as

$$C(\tau) = \langle\delta\omega_{nm}(0)\delta\omega_{nm}(\tau)\rangle. \tag{2.60}$$

This result shows that the first order response, and therefore the linear spectrum, is fully determined by the frequency correlation function. If the frequency fluctuations follow gaussian statistics, eqn. 2.56 is an exact result; otherwise it is a first-order approximation [54]. For the higher order response functions a similar approach can be followed; however, the expressions become more complex as one is forced to evaluate the averages of the products of different auxiliary functions J_{nm}(t). For example, in order to calculate $R_1(t_3,t_2,t_1)$ we need to evaluate the following average

$$\langle J_{bd}(t_3)J_{bc}(t_2)J_{ba}(t_1)\rangle, \tag{2.61}$$

which does not only contain the auto-correlations of the frequencies ω_{bd}, ω_{bc} and ω_{ba} but also their cross-correlations. It is possible to obtain approximate expressions for these ensemble average by using the cumulant expansion. The calculation, however, becomes rather complex; the reader is referred to ref. [74] for additional information.

[e] According to the cumulant expansion the average $\langle\exp[ikx]\rangle$ of the stochastic variable x can be written as

$$\exp\left[ikC_1 + \frac{(ik)^2}{2!}C_2 + \frac{(ik)^3}{3!}C_3 + ...\right], \tag{2.54}$$

where the cumulants C_i are given by

$$C_1 = \langle x\rangle, \qquad C_2 = \langle x^2\rangle - \langle x\rangle^2, \qquad C_3 = \langle x^3\rangle - 3\langle x^2\rangle\langle x\rangle + 2\langle x\rangle^3. \tag{2.55}$$

Using this result truncated to second order with $x = \int_{\tau_1}^t \delta\omega_{nm}(t')\,dt'$ and $k=-1$ we obtain eqn. 2.56.

3 Experimental methods

3.1 Light generation

3.1.1 Physical principle

Pump-probe experiments on water require femtosecond mid-infrared pulses that are intense enough to saturate a vibrational transition. Because there are no lasers that can produce such pulses, the approach is to convert the visible output of a femtosecond laser to the infrared using nonlinear crystals.

The mixing of light in nonlinear crystals can be described by nonlinear response theory. As was shown in chapter 2 the induced polarization is expressed as an expansion in the electric field,

$$P(t) = P^{(1)}(t) + P^{(2)}(t) + P^{(3)}(t) + \dots \tag{3.1}$$

The terms in this equation represent different physical processes: $P^{(1)}(t)$ describes the absorption and refraction of light; $P^{(2)}(t)$ governs three-wave mixing processes, of which second harmonic generation and difference frequency mixing are examples; finally, $P^{(3)}(t)$ is responsible for a variety of phenomena, such as two-photon absorption, self-phase modulation, and, of course, the pump-probe response. Light intensities encountered in everyday life are generally so weak that only the first term in the expansion needs to be considered. With the light intensities delivered by femtosecond lasers the second and third terms in the expansion become appreciable.

Here we shall consider the effects of the second order response. Because the nonlinear crystals used in three-wave mixing are transparent in the wavelength region of interest, the expression for $P^{(2)}(t)$ is considerably simpler than the expressions encountered in the previous chapter. One can essentially consider the polarization response to be instantaneous (see eqn. 2.46), which leads to

$$P^{(2)}(t) = \chi^{(2)} E^2(t), \tag{3.2}$$

with the constant $\chi^{(2)}$ known as the 2^{nd} order susceptibility. We now consider the effect of illuminating a material that has a non-zero $\chi^{(2)}$ by two beams of light of different frequencies, such that the electric field variation is given by

$$E(t) = E_1 e^{i\omega_1 t} + E_2 e^{i\omega_2 t} + \text{c.c.} \tag{3.3}$$

The $\chi^{(2)}$-response leads to the appearance of new frequency components in the

polarization

$$P^{(2)}(t) \propto \begin{array}{lll} 2E_1E_2e^{i(\omega_1+\omega_2)t} & + \text{c.c.} + & \text{(SFG)} \\ 2E_1E_2^*e^{i(\omega_1-\omega_2)t} & + \text{c.c.} + & \text{(DFG)} \\ E_1^2e^{i2\omega_1 t} & + \text{c.c.} + & \text{(SHG)} \\ E_2^2e^{i2\omega_2 t} & + \text{c.c.} + & \text{(SHG)} \\ 2(E_1^2+E_2^2) & & \text{(OR).} \end{array} \tag{3.4}$$

Since an oscillating polarization is a source of radiation, the material emits electromagnetic waves at these frequencies. Each of the terms in the equation represents a specific nonlinear process: sum frequency generation (SFG), second harmonic generation (SHG), difference frequency generation (DFG) and optical rectification (OR).

PHASE MATCHING Because of destructive interference between the electromagnetic waves that are emitted from different regions in the material, the intensity of the generated light is in general very low. We can understand this by considering the spatial variation of the nonlinear polarization. For simplicity we focus on difference frequency mixing but the same arguments hold for the other nonlinear processes. The spatial variation of the two fields in Eqn. (3.3) is given by $e^{in_1k_1x}$ and $e^{in_2k_2x}$, where k_1 and k_2 are the vacuum wave vectors and n_1 and n_2 are the corresponding indices of refraction in the nonlinear material. The nonlinear polarization follows the two generating fields and consequently it varies according to $e^{i(n_1k_1-n_2k_2)x}$. The generated radiation, however, which oscillates at a frequency $\omega_3 = \omega_1 - \omega_2$, has a spatial variation that is given by $e^{in_3k_3x}$. In general, the change in the index of refraction with frequency causes the generated wave to have a different wavelength than the polarization that is responsible for its generation. The result is that electromagnetic waves that originate from points in the crystal that are farther apart than a certain distance are out of phase with each other (figure 3.1). As a consequence radiation cannot build up coherently over distances longer than the coherence length L_c, which is typically between 10-100 μm.

The efficiency of nonlinear processes can be improved by increasing the coherence length. It is clear that efficient build-up of radiation can only occur if the wave vector of the nonlinear polarization matches the wave vector of the generated light. For the difference-frequency process this means that

$$n_3k_3 = n_1k_1 - n_2k_2. \tag{3.5}$$

This is the so-called phase matching condition for difference-frequency generation. In three-wave mixing it is customary to rename the fields, so that the same phase-matching condition applies to the five processes from eqn. 3.4. The high-frequency field is called the pump (p), the low-frequency field the idler (i) and the intermediate field the signal (s). In terms of these new names the phase matching condition is

$$n_\mathrm{p}k_\mathrm{p} = n_\mathrm{s}k_\mathrm{s} + n_\mathrm{i}k_\mathrm{i}. \tag{3.6}$$

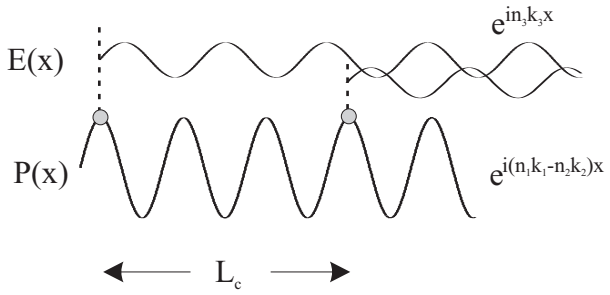

FIGURE 3.1. Phase mismatch between the polarization and the generated electric field due to dispersion in a nonlinear crystal. The two dots represent two point in the crystal that radiate an electromagnetic wave. Because the wavelength of the polarization does not match that of the radiated light, the two waves are out of phase and interfere destructively. The length over which radiation can build up coherently is called the coherence length L_c. Two waves that are generated a distance L_c from each other have a phase difference of 180 degrees.

Using $k = \omega/c$ this is expressed in terms of the frequencies

$$n_{\mathrm{p}}\omega_{\mathrm{p}} = n_{\mathrm{s}}\omega_{\mathrm{s}} + n_{\mathrm{i}}\omega_{\mathrm{i}}. \tag{3.7}$$

Finally, using $\omega_{\mathrm{p}} = \omega_{\mathrm{s}} + \omega_{\mathrm{i}}$, which ensures energy conservation, this leads to

$$\frac{n_{\mathrm{i}} - n_{\mathrm{p}}}{n_{\mathrm{p}} - n_{\mathrm{s}}} = \frac{\omega_{\mathrm{s}}}{\omega_{\mathrm{i}}}. \tag{3.8}$$

In materials with normal dispersion the index of refraction increases with frequency, so that the left-hand side of this equation is negative. Since the right-hand side is always positive, the phase-matching condition is not directly fulfilled in these materials. For phase matching to occur n_{p} needs to lie in between n_{i} and n_{s} as can be seen by inspecting eqn. 3.8. One method to achieve phase matching is based on the use of birefringent materials as the nonlinear medium; these materials have different refractive indices for different polarization directions. This method takes advantage of the tensor properties of the $\chi^{(2)}$ response; that is, the incoming fields can be polarized in a different direction than the generated field. Together, these two features make it possible to independently adjust one of the refractive indices in eqn. 3.8, as is explained below.

In order to understand the way phase matching is achieved in birefringent materials, one must study the propagation of light in these materials [16,30,115]. Figure 3.2a provides an illustration. Uniaxial birefringent crystals are characterized by two indices of refraction: the ordinary index (n_o) for light polarized along the x or y-axis and the extraordinary index (n_e) for light polarized along the z-axis. The z-axis is usually called the optical axis of the crystal. Let us now consider a beam of light that travels at an angle θ with respect to the optical axis. Because of the cylindrical symmetry, we can draw this beam in

the yz-plane without loss of generality. The index of refraction experienced by the light depends on the polarization direction. For light polarized in the xy-plane the index of refraction is n_o; this beam is called the ordinary wave. Light that is polarized in the yz-plane is referred to as the extraordinary wave and experiences an angle-dependent refractive index $n_e(\theta)$

$$\frac{1}{n_e^2(\theta)} = \frac{\cos^2\theta}{n_o^2} + \frac{\sin^2\theta}{n_e^2}, \tag{3.9}$$

which is a combination of n_o and n_e. The angle-dependence of this refractive index allows one to achieve phase matching in a three-wave mixing process. One generally chooses one or two of the three beams involved to be extraordinary waves; as a result their index of refraction can be adjusted by turning the nonlinear crystal to change the angle θ (figure 3.2b).

Another way to increase the coherence length is by periodically poling the nonlinear material. In this case the nonlinear material is grown in such a way that one of its crystal axes is periodically flipped over every distance that corresponds to one coherence length. Reversing the crystal axis has the effect of reversing the sign of $\chi^{(2)}$. As a consequence, every time the polarization and the generated electric field become out of phase, the sign of $\chi^{(2)}$ is reversed and the two are in phase again. This is called quasi phase matching.

OPTICAL PARAMETRIC AMPLIFICATION Optical parametric amplification (OPA) is a special case of difference frequency generation in which the low-frequency input field ω_2 is very weak. The OPA process starts at the front end of the nonlinear crystal where the difference frequency ω_3 is generated. As this newly created wave propagates through the crystal, it interacts with the pump field ω_1 to generate the difference frequency ω_2, which in turn interacts with ω_1 to generate more of the ω_3 field, etc, etc. This results in the amplification of the ω_2 and ω_3 fields at the cost of ω_1, so that effectively ω_1 pump photons are split into ω_2 and ω_3 photons. The low-frequency input field is called a seed and can be broadband. The wavelength region of the seed that is actually amplified is determined by phase matching. There are a few ways to generate a femtosecond seed. In our experiments this is done through continuum generation; this process consists in the generation of ultra-broadband light by focusing a femtosecond pulse inside a transparent material.

3.1.2 EXPERIMENTAL REALIZATION

The starting point in the generation of intense mid-infrared femtosecond pulses is a commercially available regenerative amplifier (Hurricane, manufactured by Spectra-Physics). This is a 'one-box' laser system that generates light pulses with a duration of 100 fs, a wavelength of 800 nm, and a pulse energy of 1 mJ. The repetition rate of the system is 1 kHz. For our experiments we have generated infrared light with a wavelength of 3 μm and 4 μm. Figure 3.3 shows the experimental setup used to generate the 4-μm pulses. Approximately 70 % of

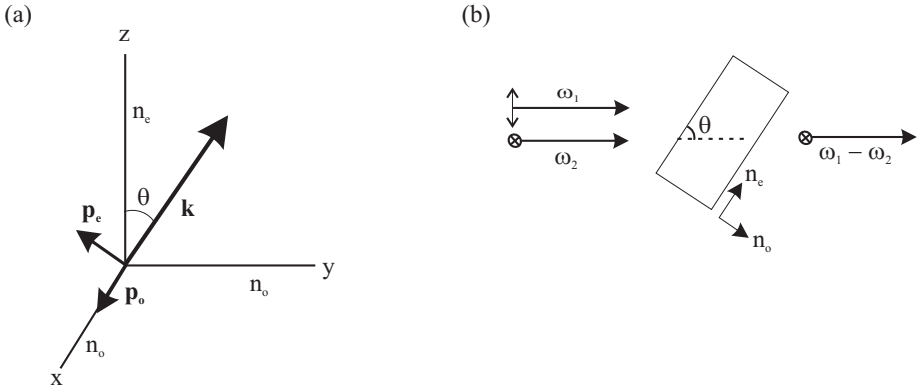

FIGURE 3.2. a) Light propagation through a uniaxial crystal. A beam of light propagating along the yz-plane can experience different refractive indices, depending on its polarization. If it is polarized in the xy-plane the refractive index is n_o. For polarization in the yz-plane the index of refraction is $n_e(\theta)$ which is a function of θ. The z-axis is called the optical axis of the crystal because for propagation in this direction the index of refraction does not depend on the polarization. b) Type I phase matching geometry for difference frequency generation. The index of refraction ω_1 can be varied by turning the crystal.

the output of the Hurricane is used to pump a Spectra-Physics optical parametric amplifier (OPA) that uses β-barium borate (BBO) as the nonlinear medium. The OPA process is seeded by a white-light continuum that is generated by focusing a small fraction of the 800 nm light into a sapphire plate. The BBO crystal in the OPA is tuned such that the 800 nm pump light is divided into photons of 1300 nm and 2000 nm. A second BBO crystal is used generate the second harmonic of the 2000 nm light. Finally, the generated light at 1000 nm is difference frequency mixed with 800 nm light to yield light at 4000 nm. For this last step a potassium niobate crystal (KNB) is used. The thus generated mid-infrared light is resonant with the OD-stretching vibration of HDO, on which most of the experiments described in this thesis have been conducted. To study the OH vibration light with a wavelength of 3000 nm is required, which is generated similarly except that the OPA is tuned to produce pulses of 2200 nm and 1200 nm and that a potassium titanyl phosphate (KTP) crystal is used in the final step. The mid-infrared light generally has a duration of 100-200 fs and an energy of a few μJ.

3.2 PUMP-PROBE SETUP

The aim of pump-probe (saturation) spectroscopy is to determine the absorption change of a sample, as it is induced by an intense pump pulse. This is done by measuring the transmission of a probe: once in the presence of the pump

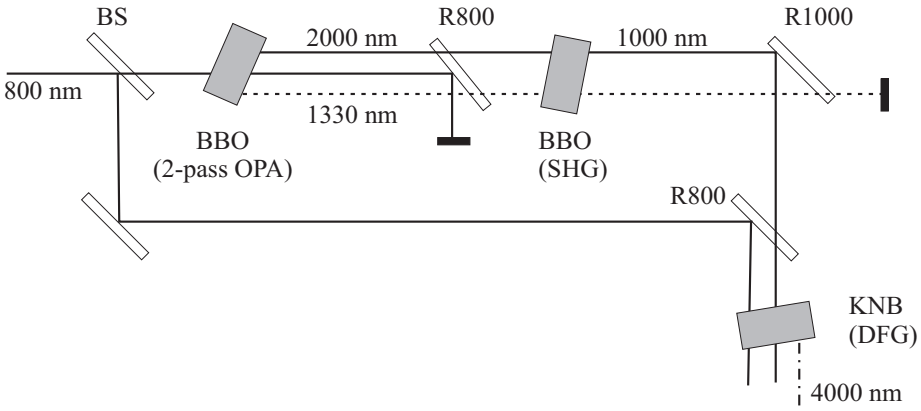

FIGURE 3.3. Setup for generating mid-infrared femtosecond pulses. Abbreviations: BS: beam splitter; BBO: BBO crystal; R800: dielectric 800 nm mirror; R1000: dielectric 1000 nm mirror; KNB: KNB crystal.

pulse (T) and once in its absence (T_0). The absorption change is related to the *relative* transmission change T/T_0,

$$\Delta\alpha(\omega) = -\ln\left(\frac{T(\omega)}{T_0(\omega)}\right). \tag{3.10}$$

Our laser system runs at a repetition frequency of 1 kHz; the transmissions T and T_0 are recorded during two consecutive laser shots. This is achieved by placing a chopper in the pump beam which block every other pump pulse. Thus the absorption change $\Delta\alpha$ is determined 500 times per second. In our experiments we do not measure the absolute probe transmissions (i.e. relative to the intensity before the sample). Instead we monitor the intensity of a reference beam, which passes through the sample but is not overlapped with the pump beam. This allows us to compensate for fluctuations in the probe intensity. The absorption change is determined from the intensities of the probe and reference pulses in the following manner

$$\Delta\alpha(\omega) = -\ln\left(\frac{I(\omega)I_{\mathrm{r},0}(\omega)}{I_0(\omega)I_{\mathrm{r}}(\omega)}\right), \tag{3.11}$$

where $I_{\mathrm{r}}(\omega)$ and $I_{\mathrm{r},0}(\omega)$ are the reference spectra in the presence and absence of the pump pulse.

Figure 3.4 shows the setup used in our experiments. The mid-infrared light enters the setup and passes a wedged CaF_2 window. The two reflections that are obtained serve as probe and reference pulses; the transmitted light forms the pump beam. The probe light is directed onto a retroreflector which is mounted on a computer controlled delay stage. The length of the probe path can thus be adjusted, which allows us to change the relative delay between the

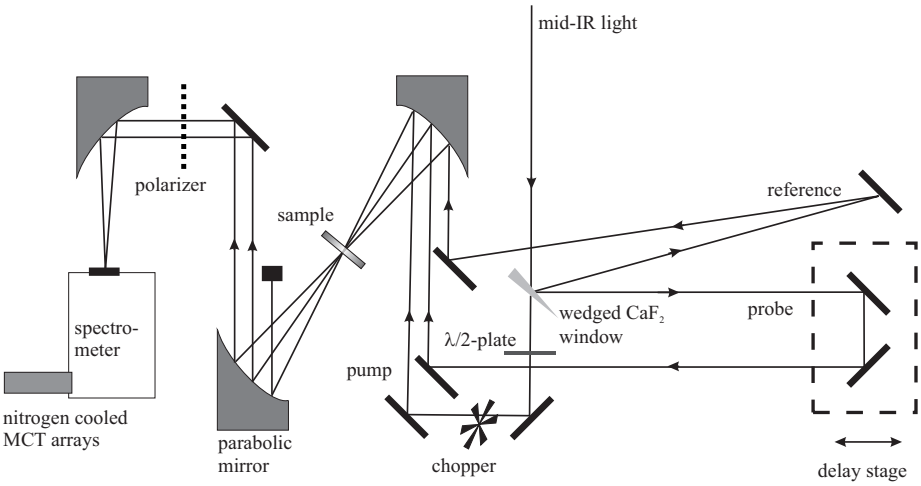

FIGURE 3.4. Pump-probe setup

pump and probe pulses. The pump, probe and reference pulses are focused onto the sample by an off-axis parabolic mirror. The pump and probe foci have a diameter of approximately 200 μm and are overlapped in the sample; the reference beam crosses the sample at another point. Behind the sample an identical parabolic mirror recollimates the three beams. Using a third parabolic mirror the probe and reference beams are focussed onto the entrance slit of an imaging spectrometer, which disperses the beams onto a 2x32 liquid-nitrogen-cooled mercury-cadmium-telluride (MCT) array. This array allows us to record the probe and reference spectra at a rate of 1 kHz, so that we can perform a shot-to-shot normalization of the transmission change.

For the polarization-resolved measurements a $\lambda/2$-plate is placed in the pump beam which sets the pump polarization at 45 degrees with respect to that of the probe beam. Behind the sample a polarizer is placed which allows us to select either the parallel or perpendicular polarization component of the probe with respect to the pump polarization. The polarizer is rotated using a motorized rotational stage. The polarization selection results in the transient absorptions $\Delta\alpha_{\parallel}(\omega, t)$ and $\Delta\alpha_{\perp}(\omega, t)$. From these signals we construct the isotropic signal which is independent of orientational processes

$$\Delta\alpha_{\mathrm{iso}}(t) = \frac{1}{3}(\Delta\alpha_{||}(t) + 2\Delta\alpha_{\perp}(t)). \tag{3.12}$$

Another combination of these signals yields the anisotropy

$$R(t) = \frac{\Delta\alpha_{||}(t) - \Delta\alpha_{\perp}(t)}{\Delta\alpha_{||}(t) + 2\Delta\alpha_{\perp}(t)}, \tag{3.13}$$

the decay of which is independent of vibrational relaxation and only reflects molecular reorientation.

3.3 SAMPLES: ISOTOPICALLY DILUTED WATER

In the experiments on water we shall study partly deuterated water molecules (HDO), rather than normal water molecules (H_2O). The water in the sample consists of normal water to which a few percent of heavy water (D_2O) has been added. This leads to the creation of HDO molecules, of which we probe the OD stretching vibration. This vibration absorbs around 4 μm. Figure 3.5 shows the infrared spectrum of H_2O with 8% HDO. Compared to neat water the spectrum shows additional resonances due to the OD-stretching vibration and the HOD bending vibration. There are a number of reasons for studying isotopically diluted water rather than neat water:

- In H_2O the two OH stretch vibrations are coupled, leading to a symmetric and an antisymmetric stretching mode. These two modes absorb at different frequencies. As the frequency of these modes depends on the hydrogen-bond strength of both OH groups there is no direct one-to-one mapping of the hydrogen-bond strength and the OH-frequency. In HDO the OH and OD-stretching modes absorb at different frequencies, so that they are effectively decoupled. As a result the OD frequency is directly correlated to the hydrogen bond strength of the OD group.

- Pure H_2O and D_2O have a very strong absorption in the OH and OD region, necessitating the use of samples of only a few microns thick. In such thin samples the effects of heating are very large and pose serious problems. The solution is to dope the water (H_2O) with HDO molecules and to study these HDO molecules instead of the normal water molecules. In this way it is possible to use thicker samples that have a relatively low absorption in the OD region.

- In pure water the excitation of the OH group is not localized on a single H_2O molecule. Instead it can hop non-radiatively from one OH group to another via a mechanism called Förster energy transfer [29,112]. This leads to a rapid decay of the anisotropy that is not related to reorientation. By studying isolated HDO molecules the excitation remains localized on one HDO molecule.

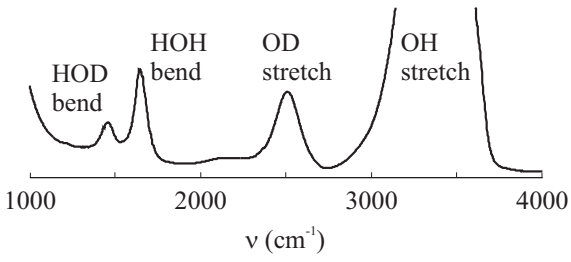

FIGURE 3.5. Infrared spectrum of HDO in H_2O.

4 Orientational dynamics of hydrogen-bonded phenol

We use femtosecond mid-infrared pump-probe spectroscopy to study the effects of hydrogen bonding on the orientational dynamics of the OD-group of phenol-*d*. We study two samples: phenol-*d* in chloroform and phenol-*d* in chloroform with an excess concentration of acetone added. For phenol-*d* in chloroform, we observe the rotational motion of the OD group around the CO bond, with a correlation time of 3.7 ps. For phenol-*d* hydrogen bonded to acetone, the reorientation time is strongly dependent on the probe frequency, varying from 3 ps on the blue side of the spectrum to more than 30 ps on the red side.

4.1 Introduction

In chapter 1 the hydrogen bond was introduced as an important structural element that is encountered in many complex systems. Examples of these systems are proteins, nucleic acids and, of course, liquid water. An important property of the hydrogen bond is that, unlike a covalent bond, it can easily break and reform. As a result hydrogen-bonded structures often exhibit a degree of flexibility. For biological systems this flexibility is essential [102]. For example, when an enzyme catalyzes a chemical reaction, it must continuously adapt to the changing chemical structure of its substrate. Another example of the flexibility provided by hydrogen bonds is the unzipping of DNA during replication.

Hydrogen-bonded systems are often very heterogeneous; as a result hydrogen bonds of greatly varying strength can be encountered within a single system. An interesting question regards the relation between the strength of an individual hydrogen bond and its ability to restrict the motion of the hydrogen-bonded chemical group. Rephrasing this: are the most tightly hydrogen-bonded groups also the least flexible? Here we study this question for hydrogen-bonded complexes of phenol-*d* and acetone, which serve as a model system. In the experiment we monitor the mobility of the OD group of phenol by polarization-resolved mid-infrared pump-probe spectroscopy; this technique was explained in chapters 1 and 2 of this thesis. The strength of the hydrogen-bond is the other parameter of relevance. It can be obtained from the linear infrared spectrum, by virtue of the correlation between the frequency of OD vibration and the strength of the hydrogen bond: the stronger the hydrogen bond, the lower the OD-stretching frequency [71, 78, 81].

As a sample we use a solution of phenol and acetone in chloroform; such a solution contains a large variety of hydrogen-bonded phenol-acetone complexes,

ranging from loosely hydrogen-bonded to very strongly bound. This inhomogeneity allows us to use a single sample to obtain information about complexes that vary strongly in their binding strength.

4.2 EXPERIMENTAL

We performed polarization-resolved mid-infrared pump-probe measurements on the OD-stretching vibration of deuterated phenol in chloroform. The pump-probe setup used in the experiment is described in chapter 2.

In order to study the effect of hydrogen bonding on the orientational dynamics of the OD group of phenol-*d* we compared two samples: a solution of phenol-*d* in chloroform (0.4 M) and a solution of phenol-*d* in chloroform (0.6 M) to which a high concentration of acetone was added (∼3 M). Phenol-*d* was obtained by dissolving 2 g of phenol-*h* (Aldrich) in 10 ml of D_2O and boiling the solution until all D_2O had evaporated. Chloroform (HPLC grade) was used as received. All measurements were performed in a static cell with an optical path length of 500 μm.

4.3 RESULTS AND DISCUSSION

LINEAR INFRARED SPECTRA Figure 4.1 shows the linear IR absorption spectra of the two samples. Two OD-stretch absorption bands can be observed in the spectrum of phenol in chloroform: a narrow band at 2650 cm^{-1} (FWHM $\simeq$ 20 cm^{-1}) and a broad band at 2500 cm^{-1} (FWHM $\simeq$ 200 cm^{-1}), where FWHM stands for full width at half maximum. The narrow band is due to monomeric phenol molecules, whereas the broad band is caused by clusters of hydrogen-bonded phenol molecules [65]. In the gas phase the OD stretching frequency of phenol-*d* lies at 2699 cm^{-1} [49]. Apparently the interaction with the solvent chloroform molecules causes a redshift of the OD-stretching frequency of approximately 50 cm^{-1}. When an excess of acetone (∼ 3M) is added, the band at 2650 cm^{-1} disappears while the band at 2500 cm^{-1} grows in intensity, which leads us to the conclusion that all phenol molecules in this sample are hydrogen bonded. As an excess of acetone is present, we can safely assume that acetone acts as the hydrogen bond acceptor, rather than other phenol molecules.

TRANSIENT SPECTRA AND VIBRATIONAL RELAXATION Figure 4.2 shows the transient spectrum of phenol in chloroform. The ground state bleach (2650 cm^{-1}) and the excited state absorption (2550 cm^{-1}) are clearly separated. Apparently the OD potential has an anharmonicity of 100 cm^{-1}. In addition to the bleach and the excited state absorption, a rather broad shoulder is observed on the red side of the bleach (∼2625 cm^{-1}). This shoulder decays much faster (∼1 ps) than the bleach and the excited state absorption (∼10 ps), and can be attributed to clusters of hydrogen-bonded phenol molecules. This assignment is supported by the linear spectrum, which shows that the tail of the cluster band lies in the region where the shoulder is observed.

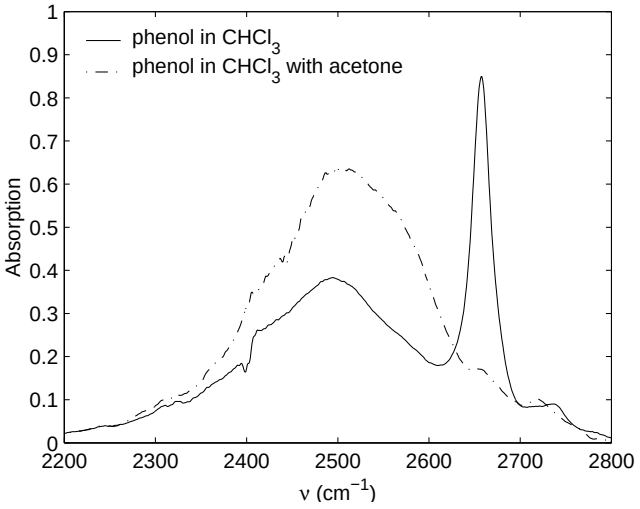

FIGURE 4.1. Linear IR absorption spectra of phenol-d in chloroform (0.4 M) and phenol-d in chloroform (0.4 M) with acetone ($\sim$ 3 M). The sample thickness was 500 μm.

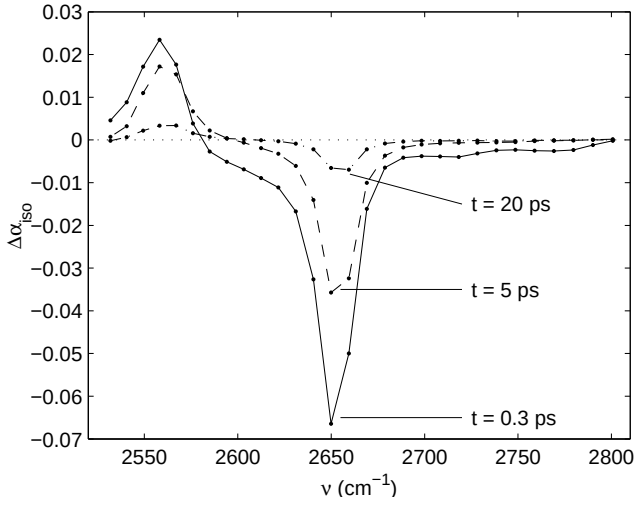

FIGURE 4.2. Transient spectra of phenol in chloroform (0.4 M) at delays of 0.3 ps, 5 ps and 20 ps. The pump pulse was centered at 2650 cm^{-1}.

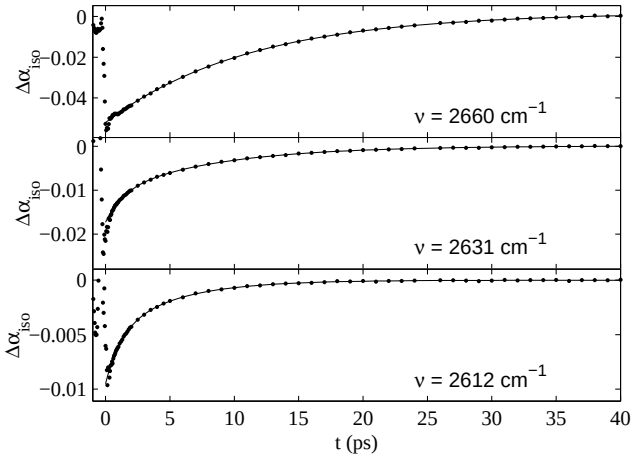

FIGURE 4.3. Delay scans at three different probe frequencies in the bleaching region of the transient spectrum of phenol-d in chloroform ($\nu_{\mathrm{pump}} = 2650$ cm^{-1}).

The decay of the transient absorption (figure 4.3) is faster on the red side of the spectrum than on the blue side. We have used biexponentials to fit these measurements, thereby accounting for the transient bleaching of the tail of the cluster band, which overlaps with the monomer band and contributes weakly to the total transient signal ($\sim 15\%$ at 2650 cm^{-1}). In figure 4.4 the two derived time constants are plotted as a function of the probe wavelength. The slow decay time, which we interpret as the lifetime of the OD-stretch vibration of monomeric phenol, varies smoothly from about 5 ps to 11 ps going from the red to the blue side of the spectrum. This behavior contrasts with that of the cluster band, which shows a remarkably constant lifetime of about 1 ps over the entire probe range.

The strong variation in vibrational lifetime as a function of frequency suggests that the (monomeric) phenol molecules are hydrogen bonded to the solvent chloroform molecules. Furthermore it suggests that the phenol-chloroform conformations do not interconvert within $\sim$10 ps (for else a frequency independent lifetime would have been observed).

Figure 4.5 shows the transient spectra of phenol in chloroform with excess acetone. We observe a broad bleaching signal and the high-frequency wing of the excited state absorption on the red side of the probe spectrum. The bleach decays monoexponentially with a time constant of about 1 ps, which is an order of magnitude faster than for phenol hydrogen-bonded to chloroform. This time constant is very similar however, to that of phenol clusters. Figure 4.6 shows a plot of the lifetime of phenol hydrogen-bonded to acetone as a function of the probe wavelength. Remarkably, hardly any variation in lifetime can be observed; only at the very blue edge does the lifetime increase.

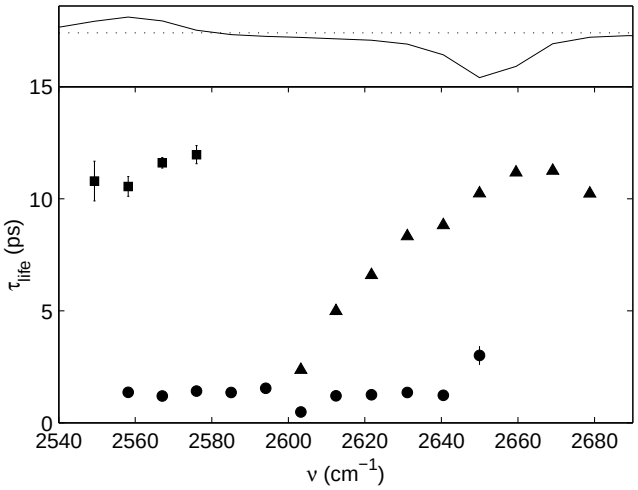

FIGURE 4.4. Time constants obtained from biexponential fits to the transient spectrum (top panel) of phenol-d in chloroform as a function of the probe wavelength ($\nu_{\text{pump}} = 2650$ cm^{-1}). The triangles correspond to the bleaching of the isolated OD band, the squares to its induced absorption and the circles to the bleaching of the cluster band.

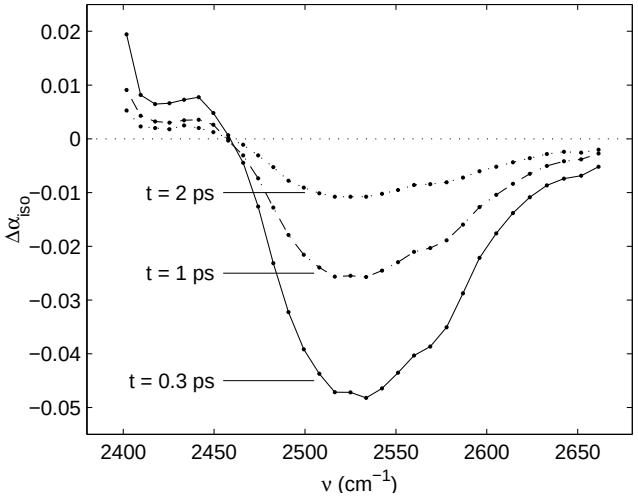

FIGURE 4.5. Transient spectra of phenol-d hydrogen-bonded to acetone in chloroform measured at 0.3 ps, 1 ps and 2 ps. The pump pulse was centered at 2525 cm^{-1}.

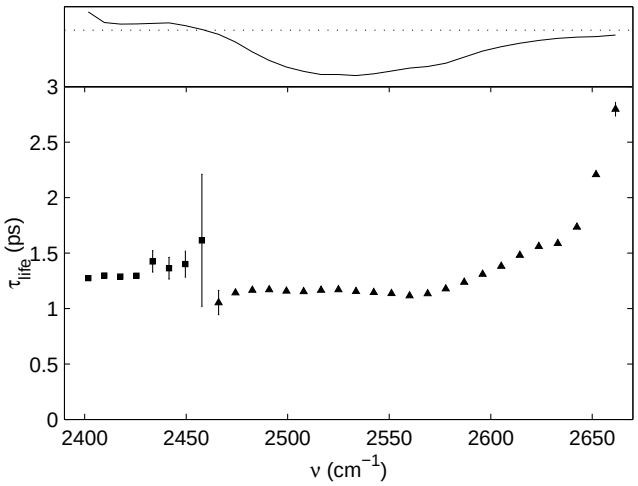

FIGURE 4.6. Lifetime of the OD vibration of phenol-*d* hydrogen-bonded to acetone as a function of probe wavelength ($\nu_{\text{pump}} = 2525$ cm^{-1}). The transient spectrum is shown in the top panel. The triangles correspond to the bleaching region of the spectrum, the squares to the excited state absorption.

THE ROLE OF THE HYDROGEN BOND IN VIBRATIONAL RELAXATION The above results show that the hydrogen bond provides, either directly or indirectly, a very efficient vibrational relaxation pathway [38]. For weakly hydrogen-bonded phenol, we observe that the lifetime decreases from 11 ps to 5 ps as the hydrogen-bond strength increases. When the hydrogen-bond strength is further increased, i.e. by adding the strong hydrogen-bond acceptor acetone, the lifetime decreases down to 1 ps. At this point the lifetime seems to reach its minimum value, and a further increase in hydrogen-bond strength no longer results in a decrease of the lifetime.

When seeking an explanation for the frequency-independence of the lifetime of phenol hydrogen-bonded to acetone, the first thing that comes to mind is that the strongly hydrogen-bonded conformations may interconvert rapidly, so that in fact, an average lifetime is observed. However we will see below that there is no rapid spectral diffusion, which means that this explanation cannot be correct. Therefore we conclude that the relaxation involves a mechanism that speeds up with increasing strength of the hydrogen bond, but only up to a certain limiting rate. Of course this leads to the question what the exact nature of this relaxation channel could be. Even though it is impossible to provide a conclusive answer based on the experiments described in this chapter, it is unlikely that the hydrogen bond is one of the accepting modes; in that case one would expect the relaxation rate to keep increasing as the hydrogen-bond becomes stronger. Instead, the role of the hydrogen bond may be indirect in matching the energy of the excited OD-stretch vibration to that of the combination of (other) accepting

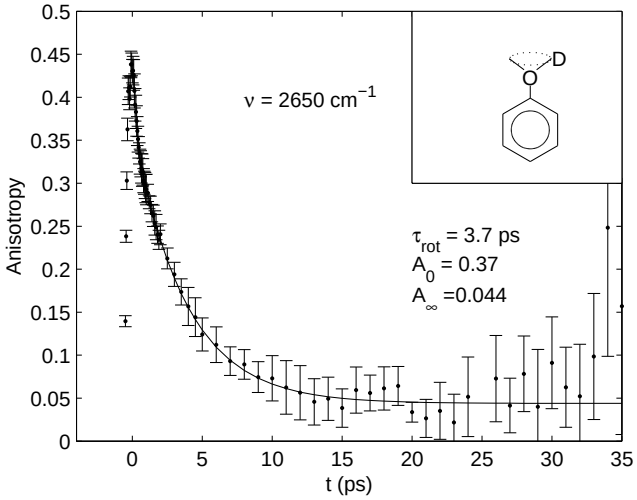

FIGURE 4.7. Anisotropy decay of phenol-d in chloroform at 2650 cm^{-1}. The solid line represents a fit to the data of the form $R = (A_0 - A_\infty)e^{-t/\tau_{\rm rot}} + A_\infty$. The inset illustrates the orientational dynamics that lead to the decay of the anisotropy.

modes.

EFFECT OF HYDROGEN BONDING ON REORIENTATION In order to obtain the reorientation time of the OD group of phenol in chloroform, we have measured the anisotropy of the transient absorption. In figure 4.7 the anisotropy is shown for the peak position of the bleach. By fitting this anisotropy to a single exponential we obtained a rotational correlation time of 3.7 ps. Interestingly, whereas the vibrational relaxation showed a strong frequency dependence for phenol in chloroform, the reorientation time is fairly frequency independent.

A point worth mentioning is that the anisotropy does not decay to zero as one would expect in the case of free rotational diffusion, but to a value of ~ 0.04. This non-zero end level can be explained by considering the two motions that play a role in the reorientation of the OD group: the first is the rotation of the OD group around the CO-bond axis, and the second is the rotation of the phenol molecule as a whole, which of course also contributes to the reorientation of the OD group. We assume that the first process occurs much faster than the second, so that on the time scale of our experiment, we essentially only observe the rotation of the OD group around the CO-bond axis (see inset figure 4.7). As this rotation restricts the reorientation of the OD group to a limited portion of the unit sphere, a non-zero anisotropy will be measured at long delays. The end level of the anisotropy is determined by the solid angle that can be covered by the OD group and therefore by the C-O-D angle.

This reasoning leads us towards attributing the reorientation time of 3.7 ps to the rotational motion of the OD-group around the CO bond. The fact that

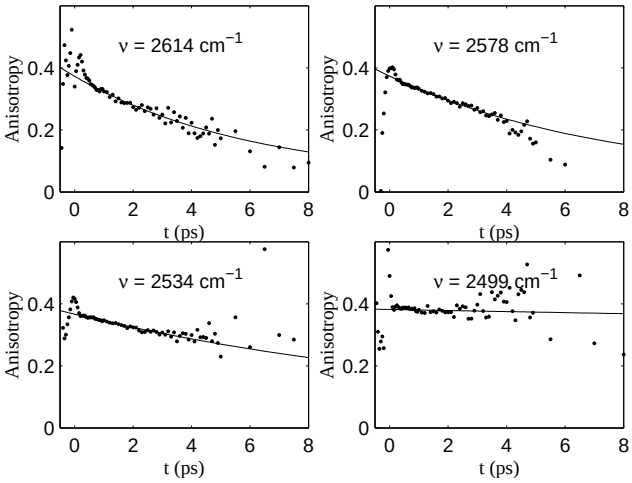

FIGURE 4.8. Anisotropy decay at different frequencies in the transient spectrum of phenol-*d* hydrogen-bonded to acetone. The solid curves are monoexponential fits with an end level of 0.04.

this time constant does not depend on frequency shows that the orientational mobility is negligibly affected by the weak hydrogen bond to chloroform. In principle the anisotropy should further decay to zero if we would measure up to longer delays, at which the molecular reorientation of phenol becomes important. Unfortunately, because of the finite relaxation time of the OD vibration, we were only able to accurately determine the anisotropy for delays up to 15 ps.

We compare these results with those obtained for phenol (strongly) hydrogen-bonded to acetone. Figure 4.8 shows the anisotropy decay of strongly hydrogen-bonded phenol at four distinct positions in the transient spectrum. Interestingly, while the lifetime showed no variation over the absorption band, we now see that the reorientation proceeds much faster on the blue side of the spectrum than on the red side. As the anisotropy decays more or less linearly over the range that we can measure, it is impossible to unambiguously fit these curves with monoexponentials including a non-zero end-level. In order to be able to assign a decay time to these curves, we have fitted them to monoexponentials with an end level that is the same as the one we found for phenol hydrogen-bonded to chloroform (0.04). The reasoning underlying this choice is that hydrogen bonding may affect the reorientation time of the OD group, but not the solid angle over which it can reorient, so that the final anisotropy should be the same.

Figure 4.9 shows the reorientation time as a function of probe wavelength for the entire probe range. On the blue side of the band the anisotropy decays with a time constant that is comparable to that of phenol hydrogen-bonded to chloroform (3 ps), suggesting that the rotation of the OD group is not hindered

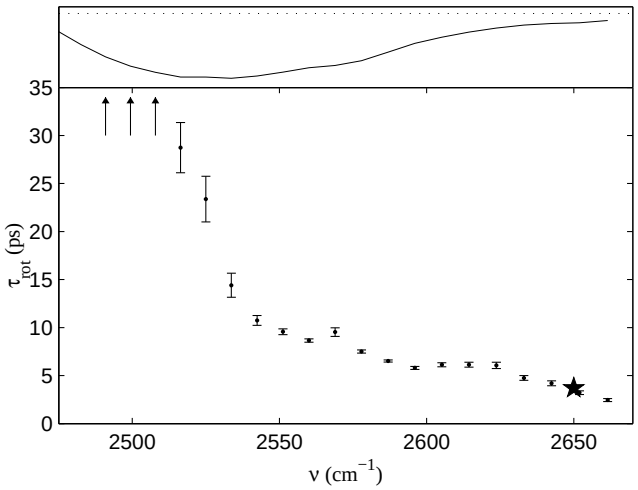

FIGURE 4.9. Reorientation time of the OD group of phenol-*d* hydrogen-bonded to acetone as a function of the probe wavelength ($\nu_{\mathrm{pump}} = 2525$ cm^{-1}). The arrows indicate reorientation times that greatly exceed 30 ps, but that could not be fitted accurately. The top panel shows the transient spectrum. The star corresponds to the reorientation time measurement for phenol-*d* in chloroform.

by the hydrogen bond for these molecules either. On the red side of the band however, the reorientation time increases dramatically to over 30 ps. For these complexes the decay of the anisotropy is likely to be determined by the reorientation of the phenol-acetone complexes as a whole and by the exchange with other species in the absorption band, involving the breaking and reformation of hydrogen bonds.

These results show that hydrogen bonds hinder the rotation of the donating hydroxyl group, and that the strongest hydrogen bonds are most effective at doing so. The fact that we were actually able to probe the orientational dynamics of unique conformations, implies that these conformations live for a relatively long time. The rate of interconversion must be slower than about 5 ps, for else we would not have observed different values of the anisotropy at this delay.

The time scales that have been identified in this paper can be placed in a broader perspective by making a comparison with the study by Nienhuys et al. on the reorientation of HDO molecules in liquid heavy water [77]. In this study HDO molecules were found to reorient with a time constant of 2.6 ps, which seems extremely rapid compared to the time constant of >30 ps observed for the strongly hydrogen-bonded OD group of phenol-*d*. This is particularly true considering that an HDO molecule is embedded in a *network* of hydrogen bonds, contrary to phenol that forms a complex with only a single acetone molecule. The paradox is resolved, when one realizes that the reorientation of water molecules is assisted by the rapid breaking and reformation of hydrogen

bonds that occurs in liquid water [56, 60]. It is more difficult to understand, however, that the reorientation of the OD group of phenol, when it is weakly hydrogen bonded to chloroform, proceeds slower (3.7 ps) than that of hydrogen-bonded HDO molecules (2.6 ps). A tentative explanation may be that the rotation of the OD group is considerably hindered by the phenyl ring, as gas phase studies and quantum chemical calculations indicate that the OD group lies preferentially in the plane of the phenyl ring [17], which implies the presence of a significant barrier for internal rotation around the CO-bond axis.

4.4 CONCLUSION

We studied the influence of hydrogen bonding on the vibrational and orientational dynamics of the OD group of phenol-*d*. Hydrogen bonding strongly affects the vibrational relaxation. The vibrational lifetime τ_{life} decreases with increasing hydrogen-bond strength: from 11 ps, for monomeric phenol molecules weakly hydrogen-bonded to chloroform, to a limiting value of ~ 1 ps for phenol molecules that are strongly hydrogen bonded to acetone. The orientational dynamics are measured by probing the anisotropy of the excitation of the OD-stretch vibration. For weakly hydrogen-bonded phenol molecules dissolved in chloroform, the anisotropy decays with a time constant of 3.7 ps to a non-zero value. This partial decay of the anisotropy results from the rotational motion of the OD group around the CO-bond axis. The molecular reorientation of phenol that would lead to a complete decay of the anisotropy takes place on a much slower time scale. The rotational motion of the OD group is observed to slow down with increasing hydrogen-bond strength, resulting in an increase of its time constant to values > 30 ps.

5 Orientational dynamics of HDO in liquid water

We use femtosecond mid-infrared pump-probe spectroscopy to study the orientational relaxation of HDO molecules dissolved in H_2O. We have measured the reorientation time constant of the OD vibration from 2430 cm^{-1} to 2600 cm^{-1}, and observe a value of 2.5 ps that shows no variation over this frequency interval. Our results are discussed in the context of previous experiments that have been performed on the complementary system of HDO dissolved in D_2O.

5.1 Introduction

The previous chapter dealt with the orientational dynamics of isolated hydrogen-bonded complexes. In this chapter we move on to a more complex system and study the motion of water molecules in the pure liquid. The complexity of liquid water arises because of the presence of an extended network of hydrogen bonds, so that it is no longer possible to speak of *isolated* hydrogen-bonded complexes. The polar environment provided by the hydrogen-bond network of water forms a medium in which many chemical processes can take place, both in living nature and in the laboratory. An important parameter in these reactions is the rate at which the hydrogen-bond network can adapt to accommodate a newly formed reaction product; ultimately, of course, this rate depends on how fast single water molecules are able to change their positions and orientations. Processes in which water reorientation plays a particularly important role include the solvation of proteins [7, 79] and proton-transfer reactions [1, 2].

The reorientation of HDO in heavy water (D_2O) was studied by Nienhuys et al. [77] In this study it was found that for delays up to 1.5 ps the reorientation of water molecules proceeds faster on the blue side of the spectrum than on the red side. For longer delays however, the reorientation time constant was observed to reach a frequency independent value of about 3 ps. The interpretation was as follows: the molecules absorbing on the blue side of the spectrum have weak hydrogen bonds and can therefore reorient faster than those absorbing on the red side. However, the hydrogen-bond length of a given water molecule fluctuates in time, and as a consequence so does its absorption frequency; this process is named spectral diffusion and was explained in section 1.3.2. Therefore, for times long with respect to the spectral diffusion timescale, the molecules lose memory of their initial frequency and a frequency-independent, average reorientation rate is observed.

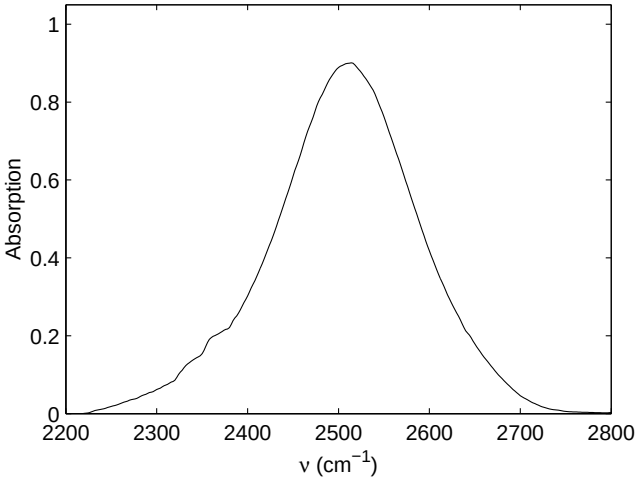

FIGURE 5.1. IR absorption spectrum of the sample used in our experiments. This is a solution of 10% HDO in H_2O. The background absorption due to H_2O has been subtracted from the spectrum. The sample thickness is $\sim$15 μm.

Steinel et al. studied water reorientation in the complementary system of HDO in H_2O and found different results for this system. Surprisingly, no frequency dependence whatsoever was observed in the reorientation time constant of the OD vibration [96]. Unfortunately, the frequency interval over which the orientational relaxation was studied was only 80 cm^{-1} around the center of the OD absorption band, which is rather limited considering the full width at half maximum (FWHM) of this band of 200 cm^{-1}. In view of the results of Nienhuys et al. it would be interesting to see whether the reorientation time constant (of HDO in H_2O) remains frequency independent when one probes further towards the blue, where those molecules reside that have very weak hydrogen bonds.

In this chapter we report on the measurement of the orientational relaxation time of HDO in H_2O over a frequency interval of 160 cm^{-1} and discuss these results in the light of the experiments on HDO in D_2O. As there are a number of points on which our findings differ from the results presented by Steinel et al., we will also compare our results to theirs.

5.2 EXPERIMENTAL

The sample studied was a 10% solution of HDO in H_2O in a static cell with an optical path length of approximately 15 μm. Such a thin sample is necessary in order to minimize the background absorption of H_2O, which absorbs weakly around 4 μm due to the presence of a combination band. The IR absorption spectrum of the sample is displayed in figure 5.1. The time-resolved measurements were performed using the setup described in chapter 2.

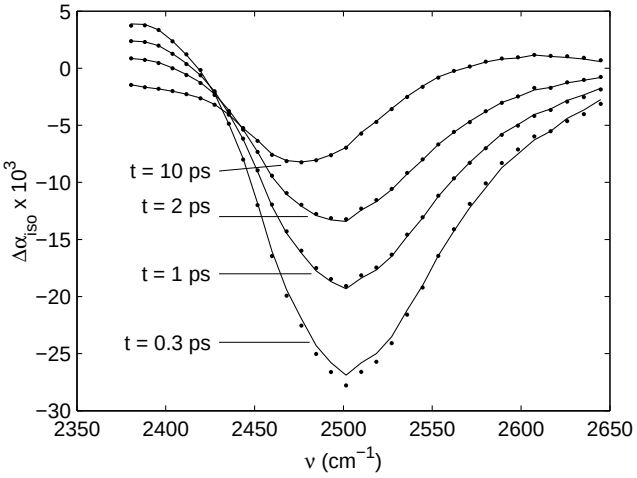

FIGURE 5.2. Transient spectra of HDO in H_2O at 0.3, 1, 2 and 10 ps (dots). The solid lines represent fits to a model that takes into account the effects of heating.

5.3 RESULTS

VIBRATIONAL RELAXATION Figure 5.2 displays the transient spectrum of HDO in H_2O for several pump-probe delays. At 0.3 ps the transient spectrum consists of a ground state bleach, centered around 2500 cm^{-1}, and an excited state absorption, of which we observe only the onset at the low-frequency side of the spectrum. The pump-probe spectrum decays with a time constant of about 2 ps, until an end level is reached at around 5 ps that shows no further decay on the timescale covered by our experiment ($\sim$500 ps).

The persistent absorption change that is observed at long delays is a consequence of the temperature increase caused by the absorption of the pump pulse, as was shown by Steinel et al. [96] and as was explained in section 1.3.3. With increasing temperature the OD-absorption band shifts to the blue, which leads to a bleach on the low-frequency side of the transient spectrum and an induced absorption on the high-frequency side. The diffusion of heat out of the focus occurs on a μs to ms timescale, which is outside the time window of our experiment.

It is clear that during the process of vibrational relaxation, which lasts a few picoseconds, the temperature of the sample will gradually rise. As such, the experimental transient spectrum contains two spectral components: a decaying spectrum representing the pure transient spectrum of the OD oscillator, and an ingrowing spectrum that is associated with the heating signal. It is important to realize that these two spectral components can have different anisotropies; it is only the anisotropy of the former component that reflects, through the

following relation (section 1.5.2),

$$R(t) = \frac{2}{5}C(t) = \frac{2}{5}\left\langle P_2(\vec{\mu}(0)\cdot\vec{\mu}(t))\right\rangle, \tag{5.1}$$

the orientational dynamics of the OD vibration. Therefore, it is important to subtract the time-dependent heating contribution from $\Delta\alpha_{\parallel}(\omega,t)$ and $\Delta\alpha_{\perp}(\omega,t)$ before using these signals to compute the anisotropy. In order to obtain the time-dependence of the heating signal, we have to consider the relaxation mechanism of the OD vibration.

Figure 5.3 displays the decay of the transient signal for three different frequencies in the spectrum. At 2635 cm^{-1} we observe a bleaching signal, whereas at 2388 cm^{-1} the signal has mainly the character of an induced absorption. Both signals decay to a non-zero end level, which is the effect of heating. In between these two frequencies, at 2436 cm^{-1}, a competition is observed between a decaying bleaching signal and an ingrowing heating signal, which at this frequency is incidentally also a bleach. This signal shows an initial decay, after which it turns over and exhibits a small, but discernible rise. The turnover indicates that the temperature rise takes place on a slightly slower timescale than the relaxation of the OD-stretching vibration. The simplest way to incorporate this effect into a relaxation model is by assuming that the energy of the OD-stretch vibration is not directly converted into heat but is first transferred to an intermediate level. Finally, the subsequent decay of the intermediate level leads to the thermal population of low-frequency modes (i.e. heating). This relaxation mechanism is characterized by two relaxation rates (k_1 and k_*) and is displayed in figure 5.4. The lifetimes (τ_1 and τ_*) of the two levels are defined as the reciprocal of the relaxation rates (k_1 and k_*).

EXPRESSION FOR THE TRANSIENT SIGNAL In the following we derive the expression for the pump-probe signal, as it follows from this relaxation mechanism. Subsequently the expression will be fit to the experimental data, which will allow us to obtain the values of the two relaxation time constants. The population dynamics of the excited molecules are described by the following three equations

$$\begin{aligned}
\frac{dN_1}{dt} &= -k_1 N_1, \\
\frac{dN_0^*}{dt} &= k_1 N_1 - k_* N_0^*, \\
\frac{dN_0'}{dt} &= k_* N_0^*,
\end{aligned} \tag{5.2}$$

where N_1, N_0^* and N_0' refer to the populations of the levels from figure 5.4. Successive integration leads to the following solutions for these differential equations

$$\begin{aligned}
N_1(t)/N_1(0) &= e^{-k_1 t}, \\
N_0^*(t)/N_1(0) &= \frac{k_1}{k_* - k_1}\left(e^{-k_1 t} - e^{-k_* t}\right), \\
N_0'(t)/N_1(0) &= \frac{k_1}{k_* - k_1}e^{-k_* t} - \frac{k_*}{k_* - k_1}e^{-k_1 t} + 1.
\end{aligned} \tag{5.3}$$

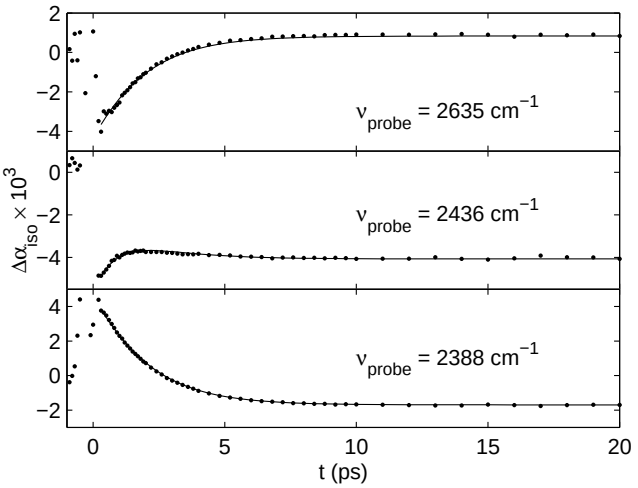

FIGURE 5.3. Delay scans at three different probe frequencies in the pump-probe spectrum.

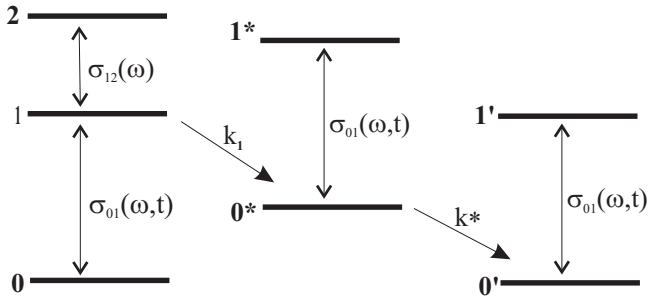

FIGURE 5.4. Schematic overview of the model that describes the dynamics of the excited HDO molecules. An excited HDO molecule decays from the $v = 1$ level to the $v = 0^*$ level with a relaxation rate k_1. The second step in the relaxation pathway is the decay of the $v = 0^*$ to the ground state with a rate k_*. The cross-sections of the $0 \rightarrow 1$, $0^* \rightarrow 1^*$ and $0' \rightarrow 1'$ transitions are identical and change as molecules decay to the ground state and energy is released into low-frequency modes. The cross-section of the $1 \rightarrow 2$ transition is taken to be time-independent.

As the excited molecules relax to the ground state, the sample is gradually heated, which leads to a shift of the cross-section spectrum $\sigma_{01}(\omega,t)$. We assume the change of $\sigma_{01}(\omega,t)$ to be proportional to the number of molecules that have decayed to the ground state (N_0')

$$\Delta\sigma_{01}(\omega,t) = \sigma_{01}(\omega,t) - \sigma_{01}(\omega,0) \propto N_0'(t). \tag{5.4}$$

The pump-probe signal is related to the three populations and to C, the total concentration of absorbing molecules,

$$\Delta\alpha(\omega,t) = C\Delta\sigma_{01}(\omega,t) + N_1(t)\sigma_{12}(\omega) + \left[-N_1(0) - N_1(t) + N_0^*(t) + N_0'(t)\right]\sigma_{01}(\omega,t). \tag{5.5}$$

By substituting for the populations and using eqn. 5.4 to eliminate $\sigma_{01}(\omega,t)$ we obtain

$$\Delta\alpha(\omega,t) = C\Delta\sigma_{01}(\omega,t)\left\{1 - \frac{N_1(0)}{C}e^{-k_1 t}\right\} + N_1(0)\left[\sigma_{12}(\omega) - 2\sigma_{01}(\omega,0)\right]e^{-k_1 t}. \tag{5.6}$$

As the fraction of excited molecules ($N_1(0)/C$) does in general not exceed a few percent we will ignore the term proportional to it. In order to find the proportionality constant between $\Delta\sigma_{01}(\omega,t)$ and $N_0'(t)$, we use the fact that for $t \to \infty$ this expression must converge to the end-level spectrum $\Delta\alpha_{\mathrm{end}}(\omega)$. Using this boundary condition and substituting for $N_0'(t)$ we arrive at the following expression for the pump-probe spectrum

$$\Delta\alpha(\omega,t) = \Delta\alpha_{\mathrm{end}}(\omega)\left\{\frac{k_1}{k_* - k_1}e^{-k_* t} - \frac{k_*}{k_* - k_1}e^{-k_1 t} + 1\right\} + N_1(0)\left[\sigma_{12}(\omega) - 2\sigma_{01}(\omega,0)\right]e^{-k_1 t}. \tag{5.7}$$

As expected this model leads to a transient spectrum consisting of two contributions: the pure pump-probe spectrum, $\sigma_{12}(\omega) - 2\sigma_{01}(\omega,0)$, which decays mono-exponentially with the lifetime of the OD vibration, and the end level, which grows in biexponentially.[a]

We have fit the experimental transient spectrum to this expression, treating the time-constants as global parameters and allowing the cross-sections to vary over the spectrum. The resulting fits are the solid lines that are depicted in

[a] In this derivation we have a used a method that differs from the one outlined in section 1.3.1. In particular we have incorporated the heating through a time-dependent spectrum $\sigma_{01}(\omega,t)$. In section 1.3.1 heating was described by a modified ground state. The difference between the two approaches is that in the present approach the heating signal is due to all molecules in the sample, whereas in the approach of section 1.3.1 it arises only due to the HDO molecules that have actually decayed. Of course, the present approach is closer to physical reality. However, both approaches lead to the same expression for the transient signal if, as we have done here, the term that is proportional to the excitation fraction is neglected. In the following chapters we will follow the approach from section 1.3.1, as it is conceptually simpler.

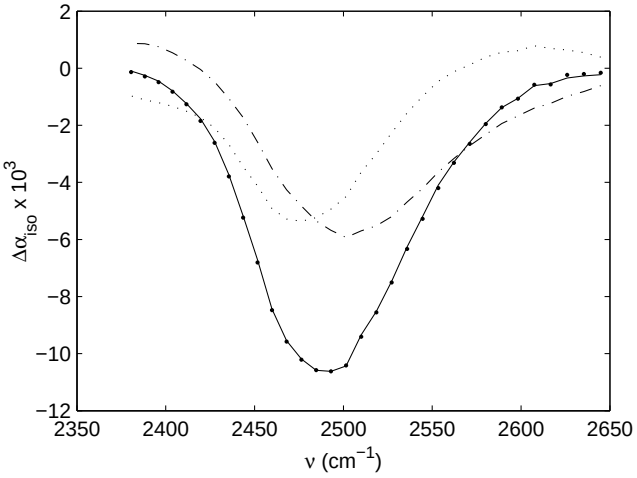

FIGURE 5.5. Decomposition of the pump-probe spectrum at 3 ps into its constituent spectral components. The dots represent the experimental pump-probe spectrum, the solid line is a fit to the model, the dotted line represents the heating component and the dashed line the pure pump-probe spectrum.

figure 5.2. The quality of the fits is excellent. Only at 0.3 ps a slight deviation is observed, the experimental spectrum having too high an intensity due to coherent coupling of the pump and probe pulses. A plot of the two spectral components constituting the transient spectrum at 3 ps is shown in figure 5.5. These two spectra are practically scaled copies of the experimental spectra at 0.3 and 10 ps. The lifetime of the OD vibration ($\tau_1 = 1/k_1$) as obtained from this fit is 1.8 ps and that of the intermediate level ($\tau_* = 1/k_*$) is 0.9 ps.

ANISOTROPY In order to calculate the anisotropy we have subtracted the spectral component corresponding to the heating effect (as obtained from the isotropic spectra) from both $\Delta\alpha_{\parallel}$ and $\Delta\alpha_{\perp}$. By following this procedure we have implicitly assumed that the heating is isotropic. The anisotropy thus obtained is shown in figure 5.6 for three different probe frequencies. As can be judged from the figure, the decay of the anisotropy does not depend on the probe wavelength. From the decay curve at the center frequency (2519 cm^{-1}) we obtained a reorientation time constant of 2.5 ± 0.1 ps and an initial value of the anisotropy of 0.32 ± 0.01. In figure 5.7 the dependence of the reorientation time on the probe wavelength is plotted, showing indeed no marked frequency dependence. We note that the reorientation time constant of 2.5 ps is very similar to the value observed in NMR experiments ($\sim$2 ps) [37, 39].

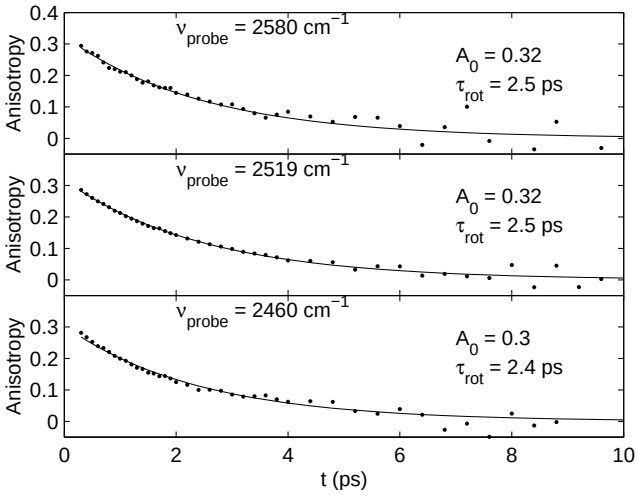

FIGURE 5.6. Anisotropy decay of the OD vibration of HDO in H_2O for three different probe frequencies. The solid lines represent fits to the data of the form $R = A_0 e^{-t/\tau_{\rm rot}}$.

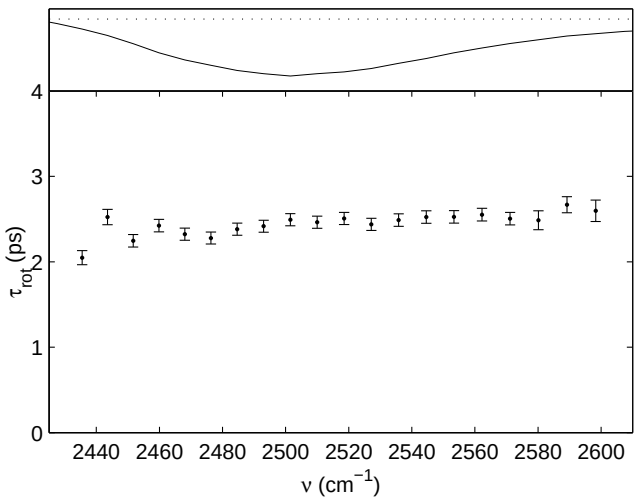

FIGURE 5.7. Reorientation time of the OD vibration of HDO in H_2O as a function of probe frequency. The top panel shows the transient spectrum.

5.4 Discussion

We begin the discussion of our results by comparing them to those obtained by Steinel et al. [96] These authors have reported a reorientation time of 1.53 ± 0.05 ps for the OD vibration, which is significantly shorter than the value of 2.5 ± 0.1 ps that we have measured. The difference in the two values is too large to be ascribed to a statistical fluctuation. In order to understand the source of the discrepancy we have carefully compared our measurements (figure 5.6) to the anisotropy decay curve presented by Steinel et al. An important difference between the two data sets concerns the noise characteristics. In figure 5.6 the noise is seen to increase exponentially with time, which makes the determination of the anisotropy impossible for delays larger than 10 ps. Such exponentially increasing noise is to be expected as it can be shown that the noise in the anisotropy is inversely proportional to the isotropic signal (which decays mono-exponentially with a time constant of 1.8 ps). The noise observed by Steinel et al., however, only increases up to a delay of 5 ps after which it remains more or less constant. Consequently these authors report the anisotropy up to a delay of 100 ps. The fact that Steinel et al. do not observe an exponentially increasing noise suggests that the isotropic signal used to construct the anisotropy did not decay to zero. In order to investigate if this may influence the anisotropy decay, we have added a small offset to our raw data (prior to computing the anisotropy) and found this to lead to a strong reduction of the noise at delays larger than 5 ps and to induce an apparent faster decay of the anisotropy. This observation may explain the discrepancy between the two reorientation time constants.

A second point of difference between our measurements and the abovementioned study concerns the vibrational relaxation of HDO, and in particular the time evolution of the spectral component that is associated with the heating signal. Steinel et al. refer to this component as the photoproduct spectrum. By subtracting the pure pump-probe spectrum (reduced in amplitude to account for vibrational relaxation) from the total signal, they have determined the amplitude and shape of the photoproduct spectrum as a function of time. Thus they show that the shape of this spectral component evolves in time until about 5 ps. They argue that this spectral evolution is caused by the equilibration of the hydrogen-bond network upon the release of the energy of the OD vibration into it.

The claim of such an evolving photoproduct spectrum is not supported by our measurements, which show that at all times the experimental spectrum can be excellently fit to a linear combination of two spectral components, suggesting that the decay of the intermediate level does result in a direct thermalization of the energy. In order to explain the spectral evolution observed by Steinel et al., we point out that the method chosen by these authors to determine the photoproduct spectrum leads to systematic errors that are larger at short delays than at large delays. At large delays the total signal is dominated by the photoproduct spectrum, and therefore even large errors in the amplitude of the subtracted pure pump-probe spectrum only lead to minor errors in the

shape of the photoproduct spectrum. However, at short delays the pure pump-probe signal makes up 90% of the total signal, so that even a small error in the amplitude of this component will lead to a large error in the photoproduct spectrum. This argument may explain the apparent time-dependence of the photoproduct spectrum as observed by these authors.

The reorientation time constant of the OD vibration of HDO in H_2O (2.5 ps) is somewhat smaller than that of the OH vibration of HDO in D_2O (3 ps) [21, 36, 77]. At first sight it may seem surprising that the orientational relaxation of the OD group proceeds faster than that of the OH group, as its moment of inertia is almost twice as large. However, one should realize that two regimes exist for the rotational motion of a water molecule, depending on the timescale on which the motion is observed [55, 70]. On short timescales the water molecule is in the librational regime, in which it performs hindered rotations. This motion is strongly affected by the moment of inertia of the water molecule. On longer timescales, however, the rate-limiting steps are the breaking of hydrogen-bonds and the collective reorganization of the hydrogen-bond network. This causes the rotational motion to become independent of the moment of inertia. The viscosity is the macroscopic parameter that reflects the collective solvent reorganization. The reorientation of large molecules is well described by the Debye-Stokes-Einstein relation, which relates the (first order) rotational correlation time (τ_1) of a molecule to the solvent viscosity (η),

$$\tau_1 = 4\pi\eta R^3/k_B T, \tag{5.8}$$

where R is the hydrodynamic radius of the reorienting molecule, k_B is Boltzmann's constant, and T is the absolute temperature. We cannot expect this relation, which treats the solvent as a continuum, to quantitatively predict the reorientation time of a water molecule. We can, however, consider the ratio of the reorientation times of HDO in H_2O and D_2O that is predicted by this equation. On the basis of the viscosities of H_2O and D_2O (0.9 mPa s and 1.1 mPa s, respectively), one expects a value of 0.8 for this ratio. This value is identical to the ratio of the reorientation times, which suggests that the orientational dynamics of the HDO molecule are determined by the collective reorganization of the solvent.

To conclude the discussion we return to our comparison of the HDO/H_2O and HDO/D_2O systems and remind the reader that the orientational dynamics of the two systems display very different frequency behaviors. As was mentioned in the introduction and was shown in a number of experimental and theoretical studies, the orientational relaxation of HDO in D_2O displays a marked frequency dependence [36, 55, 60, 77]. Initially the anisotropy decays faster on the blue side of the spectrum than on the red side, but after about 1.5 ps a frequency independent reorientation time is observed. For HDO in H_2O however, we observe the same reorientation time of 2.5 ps over the entire spectrum even when probing at the blue edge of the OD absorption band, around 2600 cm^{-1}.

This different behavior of the two systems cannot be explained from different rates of spectral diffusion in H_2O and D_2O. In their paper Steinel et al. offer an explanation for the frequency independence of the orientational relaxation of

HDO in H_2O [96]. They argue that reorientation is a process that requires the reorganization of the hydrogen-bond network. As this involves a great number of hydrogen bonds, the process does not depend explicitly on the hydrogen-bond strength of the molecule under observation. However, the question then still remains what the origin is of the observed frequency dependence in the HDO/D_2O system [55]. A clue may be provided by the fact that Nienhuys et al. pumped and probed the blue side of the spectrum [77], whereas Steinel et al. only varied the probe frequency [96], as we have done in the present study; it is therefore conceivable that the frequency of the pump plays an essential role.

5.5 Conclusion

We studied the vibrational and orientational dynamics of HDO molecules dissolved in H_2O by probing the anisotropy of the excitation of the OD vibration. The vibrational relaxation of the OD vibration of HDO was found to proceed in two steps. First the OD vibration decays to an intermediate level with a time constant of 1.8 ps, after which this level decays to the ground state with a time constant of 0.9 ps. The decay of this level is accompanied by a thermalization of the energy, which leads to a heating of the sample. The reorientation HDO molecules in H_2O was found to occur with a time constant of 2.5 ps and not to depend on the frequency at which the reorientation is probed.

6 Vibrational relaxation and orientational dynamics of HDO in heavy water

We use femtosecond mid-infrared pump-probe spectroscopy to compare the ultrafast dynamics of HDO dissolved in D_2O and H_2O. For both systems the vibrational energy relaxation proceeds through an intermediate state. The relaxation leads to heating of the sample, which is observed in the transient spectra. In order to obtain the correct anisotropy decay, the ingrowing heating signal is subtracted from the raw data. For the OD vibration this procedure works well. For the OH vibration, however, we find an additional effect that leads to a severe distortion of the anisotropy. We show that this effect can be explained by a faster reorientation of excited molecules during their relaxation as compared to unexcited molecules. We construct a model that includes this effect and is able to reproduce the experimental data. Using this model we show how the distorted anisotropy can be corrected.

6.1 Introduction

Femtosecond mid-infrared pump-probe spectroscopy is well suited for studying the fluctuations of the hydrogen-bond network of liquid water [21, 24, 36, 77, 96, 97]. As has been explained in the previous chapters, the method provides information about vibrational relaxation, spectral diffusion, and, if the experiment is done in a polarization-resolved way, about the rotational motion of water molecules. Unfortunately, the orientational dynamics of water molecules cannot be studied in the pure liquid because of the rapid Förster energy transfer between water molecules. Consequently, the results presented in the literature always refer to HDO molecules dissolved in either normal or heavy water. In both cases one studies the dynamics of a hydroxyl group (either OH or OD) that is embedded in a network of isotopically distinct hydroxyl groups.

Which of the two samples is best suited as a model for neat water (H_2O) depends on the point of view. If one argues that it is the vibration that matters, one will choose the OH-stretch vibration of HDO in D_2O. Alternatively, it can be argued that the HDO molecule only acts as a probe of the surrounding solvent, and under this assumption studying the OD vibration of HDO in H_2O seems more appropriate. There are also intrinsic properties at play, such as the lifetimes of the vibrations and the ratio of homogeneous to inhomogeneous broadening of the absorption band. As far as the lifetimes are concerned, the OD vibration is the better candidate as its lifetime is more than two times as long as that of the OH vibration. However, if one is interested in resolving

dynamical inhomogeneities, the OH vibration is more appropriate, as it is more strongly inhomogeneously broadened than the OD vibration [3, 98].

In this chapter we present mid-infrared pump-probe measurements on samples of HDO in both H_2O and D_2O. For HDO in D_2O we observe that vibrational relaxation leads to a non-isotropic orientational distribution of OH groups in the ground state. This effect has not been described previously and complicates the interpretation of anisotropy measurements. We construct a model and show that the effect can be understood from a temporary increase in mobility of OH groups directly following vibrational relaxation.

6.2 Experimental

The samples used for our experiments are 8% solutions of HDO in H_2O and D_2O. The mid-infrared pump-probe measurements are carried out in a static cell with an optical path length of approximately 25 μm.

6.3 Results

6.3.1 Vibrational relaxation

Figure 6.1 displays the transient spectra of the OD and OH-stretch vibrations of HDO at two distinct time delays: a delay immediately after excitation and a delay at which vibrational relaxation is complete. The spectra at short delays show a decreased absorption in the central part of the spectrum, due to bleaching of the $0 \rightarrow 1$ transition, and an increased absorption on the red side of the spectrum, caused by the absorption of the excited state, the spectrum of which is redshifted with respect to that of the ground state. At long delays we observe the persistent effects of heating which where extensively described in the previous chapter. Briefly: an increased temperature induces a blueshift and a decrease in cross section of the hydroxyl vibration, which leads to a bleaching on the low-frequency side of the spectrum and to an increased absorption on the high-frequency side.

In figure 6.2 we have plotted delay scans at three different frequencies in the transient spectrum of the OH-stretch vibration. Qualitatively the observed effects are similar to those described in the previous chapter for the OD vibration. At 3474 cm^{-1} the signal is dominated by a decaying bleach, whereas at 3189 cm^{-1} the signal consists of a decaying induced absorption. In between these two frequencies (3274 cm^{-1}) we observe a bleaching signal that shows an initial decay, after which it rises to reach a constant end level. The ingrowing part of this signal results from the temperature increase that follows as vibrational relaxation transfers the energy of the excited hydroxyl groups to low-frequency thermal modes in the sample. This ingrowing signal is also present at 3474 cm^{-1} and 3189 cm^{-1}, but we do not observe it as it is overshadowed by the bleaching and induced absorption. We see that the signal in figure 6.2b turns over, which indicates that the temperature rise takes place

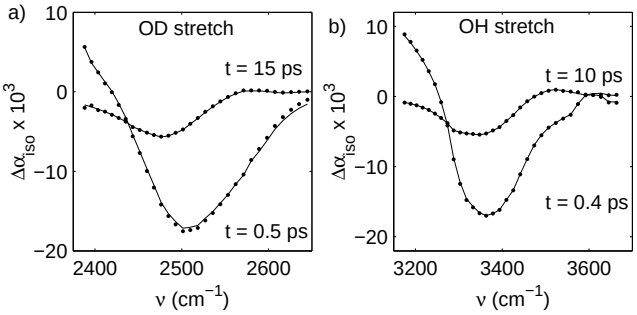

FIGURE 6.1. a) Transient spectrum of the OD vibration of HDO in H_2O (dots) directly after excitation (0.3 ps) and after vibrational relaxation (15 ps). b) Transient spectrum of the OH vibration of HDO in D_2O (dots) directly after excitation (0.3 ps) and after vibrational relaxation (10 ps). The solid lines are fits to the relaxation model that is described in the text.

on a slower timescale than the relaxation of the OH vibration. Since this is exactly the situation that applied for the OD vibration, we can use the same relaxation mechanism (fig. 5.4) to describe the relaxation of the OH vibration. In order to obtain the values of the two decay constants for the OH vibration, we have fit equation 5.7 to the pump-probe data of HDO in D_2O. We have only included delays larger than 0.4 ps in this fit, and we have used the same two time constants for all 32 frequencies in the transient spectrum. The solid lines in figures 6.1b and 6.2 show the resulting fit. As can be seen, the fit accurately reproduces the data. The lifetimes obtained are 0.7 ps for the excited state ($1/k_1$) and 0.6 ps for the intermediate level ($1/k_*$). If we compare these values with the results for the OD vibration ($1/k_1 = 1.8$ ps and $1/k_* = 0.9$ ps), we see that both the excited state and the intermediate state live considerably shorter in the relaxation of the OH vibration than in that of the OD vibration. The fact that our pump-probe data can be described by a linear combination of two time-independent spectral shapes shows that (beyond a delay of 0.4 ps) spectral diffusion plays an insignificant role in the measurements. This is a consequence of the large spectral width of the pump pulse, which almost covers the entire OH absorption band.

6.3.2 ANISOTROPIC DYNAMICS

THE EFFECT OF HEATING ON THE ANISOTROPY In the previous chapter (section 5.3) it was explained that the raw signals $\Delta\alpha_{||}$ and $\Delta\alpha_{\perp}$ should be corrected for the effects of heating before using them to compute the anisotropy. If the heating signal is very small compared to the total transient absorption, it may suffice to subtract the constant end level from the parallel and perpendicular signals, as has been done in previous studies [77]. If, however, the heating signal forms a significant portion of the total signal, it becomes important to subtract

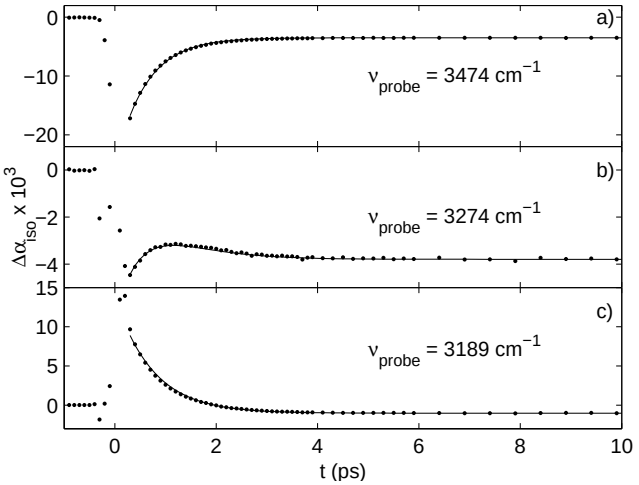

FIGURE 6.2. Delay curves at three frequencies in the transient spectrum of the OH vibration of HDO. The solid lines are fits to the relaxation model discussed in the text. a) At 3474 cm^{-1} the signal consists of a decaying bleach. b) At 3274 cm^{-1} a competition is observed between a decaying bleach and an ingrowing heating signal. c) At 3189 cm^{-1} the signal consist of a decaying induced absorption.

the *time-dependent* heating signal as it is obtained from the isotropic fit. To illustrate this let us compare the anisotropy decays of the OD vibration that are obtained by following these two correction procedures (figure 6.3a). Obviously the former procedure results in an apparent decay of the anisotropy that is too fast, demonstrating the need to account for the full time-dependent heating signal.

ANISOTROPY OF HDO IN D_2O AFTER RELAXATION OF THE OH VIBRATION We apply the correction procedure described above to obtain the anisotropy decay of the OH vibration. The result is shown in figure 6.3b. As the obtained anisotropy diverges to infinity, it is clear that this curve cannot represent the orientational dynamics of the OH vibration. Similar (anomalous) behavior is observed at other frequencies, as is shown in figure 6.4d. To illustrate the origin of these anomalies, this figure also shows the parallel and perpendicular signals from which the anisotropy decays were derived. Note that these signals have been corrected for the ingrowing heating signal.

Figures 6.5a and b contain the same data as figures 6.4a and b but have the y-axis more expanded to highlight the dynamics after $\sim$2 ps. For delays that are larger than about 3 ps the isotropic signal shows no further time evolution indicating that vibrational relaxation has been completed and that no excited molecules remain. However, when inspecting the parallel and perpendicular components, we notice a residual bleaching in the parallel signal and a residual induced absorption in the perpendicular signal. These residual signals

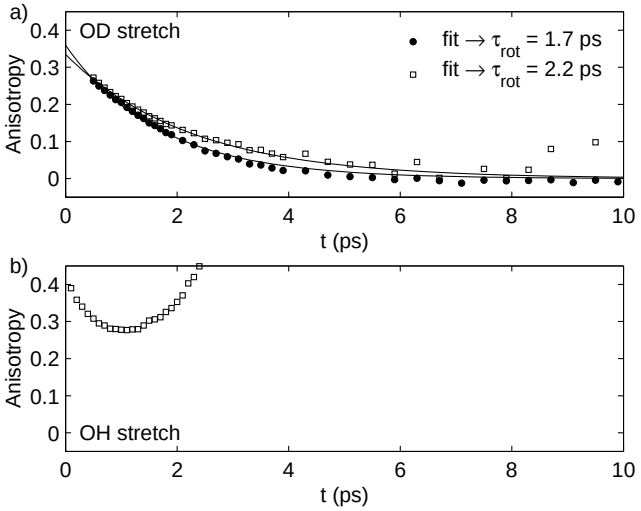

FIGURE 6.3. a) Anisotropy decay of HDO in H_2O at 2510 cm^{-1} constructed from raw data that was corrected for heating in two different ways. In the first method (solid circles) the constant end level is subtracted from the raw data. The second method (open squares) subtracts the time-dependent heating signal. The solid lines represent mono-exponential fits to the data points. The first method leads to a reorientation time of 1.7 ps, and the second method to a reorientation time of 2.2 ps. b) Anisotropy decay of HDO in D_2O at 3410 cm^{-1}. The raw data has been corrected for the ingrowing heating signal, but nevertheless a flawed anisotropy is obtained.

explain the observed divergences in the anisotropy. However, we are left with the question what the origin of these residual signals may be.

A striking aspect of the residual signals is that their sign does not depend on whether the original signal is a bleach (figure 6.4a) or an induced absorption (figure 6.4b). This is the case for the entire spectrum, as can be seen from figure 6.6 that shows the difference between the parallel and the perpendicular signals for a delay of 3 ps. A difference between the parallel and perpendicular signals, at delays at which there are no excited molecules, implies that the relaxation resulted in a distribution of ground state molecules that is anisotropic: after relaxation there are more OH groups aligned perpendicular to the pump than there are aligned parallel to it. Below we propose a mechanism that explains the creation of such an anisotropic distribution of ground state molecules.

PHYSICAL MECHANISM It is usually assumed that vibrational excitation of molecules does not affect their orientational dynamics. In this section we investigate the consequences of dropping this assumption. Let us first imagine an isotropic distribution of molecules out of which a subensemble is excited using linearly polarized light. Figure 6.7a shows a polar plot of the orientational

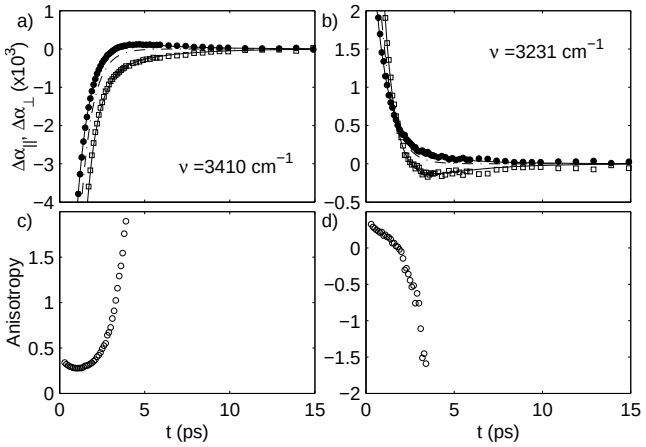

FIGURE 6.4. a,b) Parallel (open squares) and perpendicular signals (solid circles) for HDO in D_2O (after correction for heating) at 3410 cm^{-1} and 3231 cm^{-1}. The dashed line represents the isotropic signal. The solid lines are fits to the model that is described in the text. c,d) Anisotropy decays associated with the signals in a) and b).

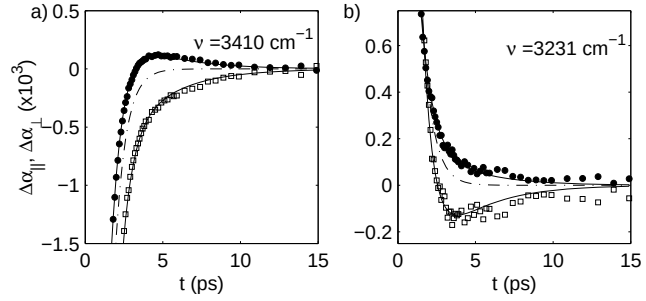

FIGURE 6.5. a,b) The same plots as those in figure 6.4a and b but with the y-axis expanded. The open squares represent the parallel signal, the solid circles represent the perpendicular signal, the dashed line is the isotropic signal, and the solid lines are fits to the model that is described in the text.

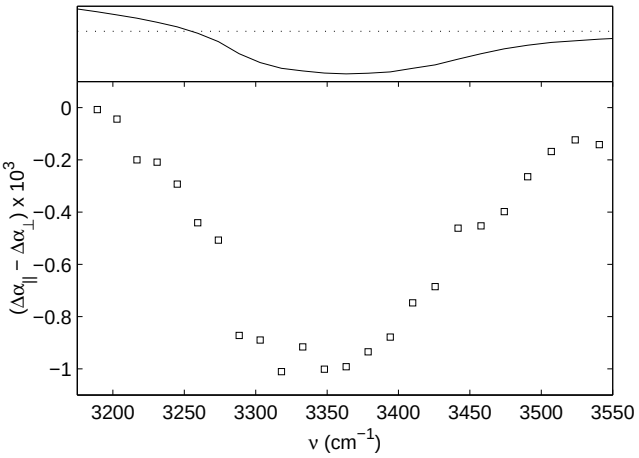

FIGURE 6.6. Difference between the parallel and perpendicular signals of the OH vibration at a delay of 3 ps. The top panel shows the transient spectrum at a delay of 0.3 ps. Apparently the parallel signal is lower than the perpendicular signal over the entire spectrum, even in the region of the transient spectrum that has the character of an induced absorption.

distribution of the excited molecules, immediately upon excitation. The plot follows a $\cos^2\theta$ distribution, where θ is the angle between the pump polarization and the molecular dipole moment. The excitation also leads to the formation of an 'orientational hole' in the distribution of ground state molecules, which is sketched in figure 6.7b. As the delay is increased, these distributions become more isotropic because of molecular reorientation. If the excited molecules reorient faster than the ground state molecules, the subensemble of (initially) excited molecules becomes more isotropic than the subensemble of molecules that had remained in the ground state (figure 6.7c and 6.7d). If these two distributions are added, we arrive at the distribution in figure 6.7e. This distribution has more molecules aligned perpendicular to the pump than parallel to it, which agrees with the experimental observation.

QUANTITATIVE DESCRIPTION In this section we provide a quantitative description of the mechanism that is described above. The isotropic signal (corrected for the heating signal) that follows from the relaxation scheme in figure 5.4 is given by

$$\Delta\alpha_{\rm iso}(\omega,t) = N_1(t)\sigma_{12}(\omega) + [-N_1(0) - N_1(t) + N_0^*(t) + N_0'(t)]\,\sigma_{01}(\omega), \quad (6.1)$$

where $\sigma_{01}(\omega)$ stands for the ground state spectrum and $\sigma_{12}(\omega)$ for the excited state spectrum. The expressions for the populations of the different levels can be found in section 5.3. In order to obtain the corresponding expressions for the parallel and perpendicular signals we start with the expressions that apply

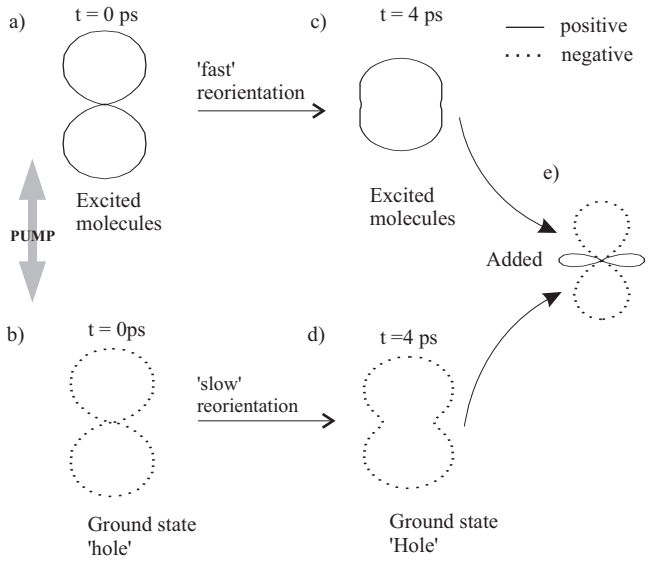

FIGURE 6.7. Illustration of the effect that leads to a bleach in the parallel signal and an induced absorption in the perpendicular signal, at a time delay for which vibrational relaxation is complete. The pump beam creates a $cos^2\theta$ distribution of excited molecules (a). At the same time an anisotropic 'hole' is created in the distribution of ground state molecules (b). After a few picoseconds the orientational distribution of initially excited molecules becomes more isotropic (c). The 'hole' in the distribution of ground state molecules also becomes more isotropic, however, the ground state molecules reorient more slowly than the excited molecules (d). Adding the two contributions results in a distribution with more molecules perpendicular to the pump than parallel to it (e).

for a single level

$$\Delta\alpha_{||}(t) = \Delta\alpha_{\rm iso}(t)(1+2R(t)), \tag{6.2}$$
$$\Delta\alpha_{\perp}(t) = \Delta\alpha_{\rm iso}(t)(1-R(t)). \tag{6.3}$$

These expressions were obtained by inverting the defining equations for $\Delta\alpha_{\rm iso}(t)$ and $R(t)$ (eqns. 1.48 and 1.64). The total signals can be written as the sum of such contributions

$$\begin{aligned}\Delta\alpha_{||}(\omega,t) = \; & \sigma_{12}(\omega)N_1(t)[1+2R_1(t)] \\ & -\sigma_{01}(\omega)N_1(0)[1+2R_0(t)] \\ & -\sigma_{01}(\omega)N_1(t)[1+2R_1(t)] \\ & +\sigma_{01}(\omega)N_0^*(t)[1+2R_0^*(t)] \\ & +\sigma_{01}(\omega)N_0'(t)[1+2R_0'(t)],\end{aligned} \tag{6.4}$$

$$\begin{aligned}\Delta\alpha_\perp(\omega,t) = \; & \sigma_{12}(\omega)N_1(t)[1-R_1(t)] \\ & -\sigma_{01}(\omega)N_1(0)[1-R_0(t)] \\ & -\sigma_{01}(\omega)N_1(t)[1-R_1(t)] \\ & +\sigma_{01}(\omega)N_0^*(t)[1-R_0^*(t)] \\ & +\sigma_{01}(\omega)N_0'(t)[1-R_0'(t)].\end{aligned} \tag{6.5}$$

In these expressions R_1, R_0, R_0^*, R_0' are the anisotropies of the levels.

At this point it is important to distinguish between the correlation function $C(t)$ of a level and the anisotropy $R(t)$ of the same level. $C_i(t)$ represents the correlation function that describes the orientational dynamics of a vibration (through Eq. 5.1) *while it is in level i*. $R_i(t)$, on the other hand, describes the dynamics of the anisotropy while taking into account the entire relaxation history before the system reached level i . An additional, minor point of difference is that the anisotropy $R_i(t)$ is normalized to 2/5 whereas the correlation function $C_i(t)$ is normalized to 1.

To illustrate the above, we consider a vibration that relaxes from level a to b, as is shown in figure 6.8a. For level a the anisotropy is proportional to the correlation function of the level. In order to calculate the anisotropy of level b however, one has to integrate over all possible relaxation histories of the molecule, as is illustrated in figure 6.8b. This gives us the following expressions

$$R_a(t) = \frac{2}{5}C_a(t), \tag{6.6}$$

$$R_b(t) = \frac{2}{5}\int_0^t C_a(t')C_b(t-t')P(a_{0\to t'}, b_{t'\to t})dt', \tag{6.7}$$

where $P(a_{0\to t'}, b_{t'\to t})dt'$ is the probability that the molecule is in level a from $t = 0$ to $t = t'$ and in level b from $t = t'$ to $t = t$. By performing successive integrations, the same method can be applied to more complex relaxation mechanisms. The required probability densities can usually be obtained in a straightforward manner from the relaxation mechanism. For example, in the above case the probability density is given by

$$P(a_{0\to t'}, b_{t'\to t}) = -\frac{1}{N_b(t)}\frac{dN_a(t')}{dt'}. \tag{6.8}$$

Using this method the anisotropies appearing in Eqs. 6.4 and 6.5 can be expressed in terms of the correlation functions of the individual levels, which are assumed to be of mono-exponential form,

$$C_0(t) = A_0 e^{-\kappa_0 t}, \tag{6.9}$$

$$C_1(t) = A_1 e^{-\kappa_1 t}, \tag{6.10}$$

$$C_0^*(t) = A_0^* e^{-\kappa_0^* t}, \tag{6.11}$$

$$C_0'(t) = A_0' e^{-\kappa_0' t}. \tag{6.12}$$

In these expressions $\kappa_0, \kappa_1, \kappa_0^*$ and κ_0' are the orientational correlation times of the states observed in the vibrational relaxation of the OH vibration. A_0, A_1, A_0^*

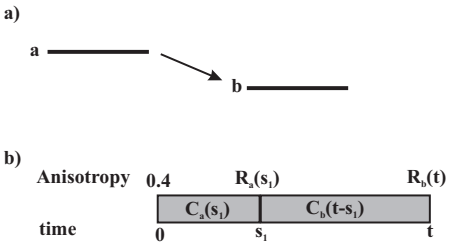

FIGURE 6.8. a) Relaxation scheme of a system that relaxes from level a to b. b) Integration scheme used to calculate the anisotropy of level b. Until $t = s_1$ the molecule is in level a and its correlation function decreases by a factor $C_a(s_1)$. From $t = s_1$ to t the molecule resides in level b and as a consequence its correlation function further decreases by a factor $C_b(t - s_1)$. In order to find the anisotropy of level b one must integrate over all possible times s_1 at which the molecule decays from level a to b.

and A_0' are the amplitudes of the correlation functions. There are two options for incorporating the increased mobility of excited molecules into the model. First, one can assume that the higher mobility is the consequence of a higher reorientation rate of one of the states from figure 5.4. This amounts to choosing one of the rate constants $\kappa_1, \kappa_0^*, \kappa_0'$ to be larger than κ_0. Alternatively, one may assume that when the OH vibration relaxes from one state in figure 5.4 to another, it passes through additional levels that have a very high mobility in combination with a short lifetime. As a consequence, these levels are not observed in the vibrational relaxation but do affect the orientational dynamics. This possibility is included by allowing A_0^* or A_0' to differ from 1. Finally we note that the initial value of the anisotropy can be tuned by allowing A_0 and A_1 to differ from 1.

Appendix 6.6.1 lists the expressions for the anisotropies, together with their derivation. By inserting these expressions into Eqs. 6.4 and 6.5 we obtain closed expressions for the parallel and perpendicular signals which can be compared to our experimental data.

COMPARISON WITH THE EXPERIMENTAL DATA Because of the large number of free parameters, one will not be able to unambiguously determine all parameters from fitting the model to the experimental data. Therefore, we will rather make it our aim to investigate what aspects of the model are essential for providing a good description of the measurements. We achieve this by constraining the majority of the parameters in the following way. We assume that the difference in reorientation rate between excited and ground molecules comes fully from an increase in mobility upon relaxing from the intermediate level to the ground state. Under this assumption the time constants $\kappa_0, \kappa_1, \kappa_0^*$ and κ_0' should be equal to each other. Subsequently, we choose A_0' as a fitting parameter and fix $A_0^* = 1$. In order to allow for an initial anisotropy that deviates from 0.4,

we include A_0 and A_1 as fitting parameters but constrain them to be equal to each other. Finally we use the values for k_1 and k_* that were obtained from the isotropic data. This leaves us with three independent fitting parameters.

We have used this procedure to simultaneously fit the parallel and perpendicular pump-probe signals at all frequencies in the transient spectrum. In order to avoid complications arising from the coherent coupling of the pump and probe pulses we have fit the data starting at a delay of 0.5 ps. The solid curves in figures 6.4 and 6.5 represent the resulting fit at two frequencies in the transient spectrum. These curves can be seen to describe the data very well. The fit leads to a reorientation time constant of 3 ps ($1/\kappa_0 = 1/\kappa_1 = 1/\kappa_0^* = 1/\kappa_0'$), an initial value of the anisotropy of 0.35 ($= 2/5A_0 = 2/5A_1$), and a value for A_0' of 0.86.

We have also performed a fit based on the assumption that the faster reorientation of excited molecules is the consequence of an intrinsically higher reorientation rate of the intermediate level. For this purpose κ_0^* was allowed to vary independently of the other three time constants, which were forced to be equal to each other. The following constraints were used for the amplitudes: $A_0^* = A_0' = 1$ and $A_0 = A_1$. This procedure is characterized by three independent parameters and leads to an equally good description of the data as the previous procedure. The following parameters are obtained: $1/\kappa_0 = 1/\kappa_1 = 1/\kappa_0'$ $= 3.2$ ps, $1/\kappa_0^* = 1.7$ ps and $2/5A_0 = 2/5A_1 = 0.35$.

From the above it is clear that the divergence in the anisotropy can be explained quantitatively by assuming that excited molecules reorient slightly faster at some stage during the relaxation than ground state molecules. The fact that both fits lead to a good agreement indicates that the description is not very sensitive to the exact mechanism that leads to this effect.

We can now attempt to correct the anisotropy decay for this effect. In this attempt we will use the former of the two fits, i.e. the case in which $R_0'(t)$ differs from $R_0(t)$. This description results in the correction terms $K_{||}(\omega, t)$ and $K_\perp(\omega, t)$ that are to be added to $\Delta\alpha_{||}(\omega, t)$ and $\Delta\alpha_\perp(\omega, t)$, respectively, and that are given by

$$K_{||}(t) = 2N_0'(t)\sigma_{01}(\omega)\left[R_0(t) - R_0'(t)\right], \tag{6.13}$$

$$K_\perp(t) = -N_0'(t)\sigma_{01}(\omega)\left[R_0(t) - R_0'(t)\right]. \tag{6.14}$$

Calculating the anisotropy based on the signals corrected in this way, we obtain the curve in figure 6.9. Fitting this curve to an exponential decay, we obtain a time constant of 2.4 ps, which is slightly shorter than the time constant of 3 ps obtained from the fit of the raw data.

We remark that the uncertainty in the extracted time constant is larger than one would expect on the basis of the spread in the data points from figure 6.9 alone. This is because the correction procedure itself introduces a substantial uncertainty as it relies on subtracting relatively large correction terms from the raw data. We estimate the overall uncertainty in the extracted time constant to be approximately 20%.

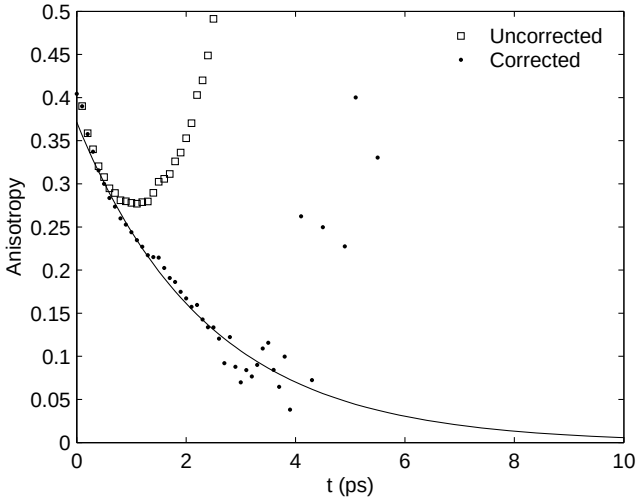

FIGURE 6.9. Anisotropy decay of HDO in D_2O at the maximum of the bleach ($\nu = 3410\ \mathrm{cm}^{-1}$). The correction procedure described in the text has been employed (dots). For comparison the uncorrected anisotropy is also shown (open squares). The solid line is a mono-exponential fit.

6.4 DISCUSSION

We have used two different approaches to incorporate the higher mobility of excited HDO molecules compared to ground state molecules into the relaxation model. There is a subtle difference in the physical mechanisms that underly these approaches. The first approach attributes the higher reorientation rate of excited molecules to an increased mobility upon relaxation from the intermediate level to the ground state. In this scenario, it seems likely that the relaxation of the intermediate level leads to the transient excitation of low-frequency, intermolecular vibrations [61,82], as it can be expected that such excitation increases the orientational mobility of the OH group. This implies that the intermediate level in the relaxation is a combination of intramolecular vibrations, the decay of which leads to the transient excitation of intermolecular vibrations, such as hydrogen-bond vibrations, D_2O librations and the HDO librations. In this scenario a likely candidate for the intermediate level is the overtone of the HDO bending vibration [22,61,68,84]. The second approach relates the higher mobility of excited molecules to a high intrinsic reorientation rate of the intermediate level. In this case the low-frequency modes mentioned above should themselves be viewed as the intermediate level. Whichever of these two mechanisms is the correct one, it is likely that the transient excitation of intermolecular vibrations plays a central role in explaining the increased mobility of excited molecules during their relaxation.

The effect described here can also be viewed as a local heating effect. In

this perspective vibrational relaxation leads to a brief but intense temperature jump in the immediate surroundings of the relaxed molecule, which in turn leads to an increase in its mobility. Adopting this viewpoint it is reasonable to assume that the effect is not restricted to hydrogen-bonded systems but occurs quite generally in systems undergoing vibrational relaxation. A necessary condition, however, is that the system is dilute because the magnitude of the effect decreases if the orientational dynamics of unexcited molecules are also affected by the relaxation.

We note that the faster reorientation of excited molecules compared to unexcited molecules, does not imply that HDO molecules reorient faster *while they are in the* $v = 1$ *state*. In a previous study the central region of the induced absorption was directly probed, and a slightly longer reorientation rate was observed for the $1 \rightarrow 2$ transition than for the $0 \rightarrow 1$ transition [77]. Our present results show that the lower orientational mobility of the $v = 1$ state is more than compensated by the increase in mobility that occurs after the molecule relaxes from the $v = 1$ state.

The higher mobility of excited HDO molecules relative to unexcited molecules has not been reported in previous studies of the orientational dynamics of HDO in D_2O [36, 70, 77]. One may suspect that in these studies the increase in the anisotropy was obscured by noise, since the noise in the anisotropy grows exponentially with delay time. Also, the concentration of HDO employed in these studies was lower ($\sim$0.5 %) than in the present study ($\sim$8%). This suggests that the HDO concentration may be a relevant parameter, and this would indicate that the effect described in this chapter is not a single-molecule effect. The increased mobility of HDO molecules upon relaxation may depend on the nearby presence of other excited HDO molecules. Further experiments at different concentrations and excitation levels are needed to settle this issue.

The divergence in the anisotropy that is observed for the OH-stretch vibration of HDO in D_2O is not observed for the OD-stretch vibration of HDO in H_2O. For the OH vibration the effect is so dramatic because of the short lifetime of the vibration compared to its reorientation time. As such, the mobility difference dominates the pump-probe signal at long delays. For the OD vibration this situation does not occur because the lifetime of the vibration (1.8 ps) is only slightly shorter than the reorientation time (2.5 ps). A second factor that diminishes the visibility of the effect for the OD vibration is that the amount of energy released upon relaxation is 30% less for this vibration than for the OH vibration due to its lower frequency. Finally, the OD vibration could possibly relax via a different mechanism than the OH vibration, and this mechanism may lead to a lower degree of excitation of the hydrogen-bond vibrations. As a consequence, the mobility of an HDO molecule may be less affected by the relaxation of the OD vibration than by the relaxation of the OH vibration.

We conclude the discussion of our results by pointing out a final consequence of the increased mobility of excited HDO molecules. The vibrational relaxation of the OH vibration of HDO in D_2O leads to a distribution of ground state molecules that has more OH groups aligned perpendicular to the pump than

parallel to it. In a system that is as highly coordinated as liquid water, such an anisotropic distribution can only exist if it is counterbalanced by an opposite anisotropy in the orientational distribution of the OD groups. The corollary of this statement is that vibrational relaxation results in an anisotropic isotope distribution: the H/D ratio of the hydroxyl groups pointing perpendicular to the pump polarization has increased at the expense of the H/D ratio of the hydroxyl groups pointing parallel to the pump polarization.

6.5 Conclusion

We studied the vibrational relaxation and orientational dynamics of HDO dissolved in D_2O and H_2O. The relaxation of both systems was modeled using a relaxation model with an intermediate level. After subtracting the heating signal that was obtained from the model, we could compute the anisotropy of the OD vibration. In the case of the OH vibration, however, this yielded a diverging anisotropy. We have shown that this anomalous behavior is caused by a faster reorientation of excited molecules during their relaxation. The increase in reorientation rate is likely to result from the transient excitation of hydrogen-bond stretching and bending vibrations. A consequence of the higher mobility of excited molecules is that vibrational relaxation ultimately leads to the creation of an anisotropic orientational distribution of the OH groups in the ground state. Because the orientational distribution of all hydroxyl groups (OH and OD) remains isotropic, this amounts to the creation of an anisotropy in the isotope distribution of the hydroxyl groups.

The increase in the reorientation rate of excited molecules during their relaxation can be expected to occur quite generally in pump-probe experiments. However the effect is only actually observed whenever the following three conditions are met: the bleaching of the fundamental transition is measured, the lifetime of the observed vibration is significantly shorter than its reorientation time, and the sample studied is not (isotopically) pure.

6.6 Appendix

6.6.1 Equations for the orientational dynamics

In this appendix we derive the expressions for the anisotropies that appear in Eqs. 6.4 and 6.5. The anisotropies $R_0(t)$ and $R_1(t)$ are proportional to the correlation functions

$$R_0(t) = 2/5 C_0(t), \tag{6.15}$$
$$R_1(t) = 2/5 C_1(t). \tag{6.16}$$

The anisotropies of the intermediate levels can be obtained by integrating over all possible relaxation histories, similar to the example of the two-level system

discussed in section 6.3.2,

$$R_0^*(s_2) = \frac{2}{5}\frac{\int_0^{s_2} ds_1 k_1 N_1(s_1) F(s_2 - s_1) C_1(s_1) C_0^*(s_2 - s_1)}{N_0^*(s_2)}, \quad (6.17)$$

$$R_0'(t) = \frac{\int_0^t ds_2 k_* N_0^*(s_2) R_0^*(s_2) C_0'(t - s_2)}{N_0'(t)}. \quad (6.18)$$

In these equations k_1, k_*, N_0, N_0^* and N_0' refer to the relaxation mechanism depicted in figure 5.4. $F(s_2 - s_1)$ in Eq. 6.17 represents the probability that a molecule that has decayed to the intermediate level at time s_1 is still in this level at time s_2. This probability is given by $e^{-k_*(s_2-s_1)}$. By carrying out the integrations and replacing the dummy variable s_2 by t we obtain the following expressions

$$R_0^*(t) = \frac{2}{5} A_1 A_0^* \frac{k_1 - k_*}{k_1 - k_* + \kappa_1 - \kappa_0^*} \frac{e^{-(k_1+\kappa_1)t} - e^{-(k_*+\kappa_0^*)t}}{e^{-k_1 t} - e^{-k_* t}}, \quad (6.19)$$

$$R_0'(t) = \frac{2}{5} A_1 A_0^* A_0' \frac{k_1}{k_1 - k_* + \kappa_1 - \kappa_0^*} \frac{N_1(0)}{N_0'(t)} \left\{ \frac{k_*}{k_1 + \kappa_1 - \kappa_0'} \left(e^{-(k_1+\kappa_1)t} - e^{-\kappa_0' t} \right) - \frac{k_*}{k_* + \kappa_0^* - \kappa_0'} \left(e^{-(k_*+\kappa_0^*)t} - e^{-\kappa_0' t} \right) \right\}. \quad (6.20)$$

8 Observation of immobilized water molecules around hydrophobic groups

We have used femtosecond mid-infrared spectroscopy to study the orientational mobility of water molecules in the hydration shells of hydrophobic groups. Our results show that hydrophobic groups are surrounded by a number of water molecules that display much slower orientational dynamics than the bulk liquid and that are therefore effectively immobilized. It turns out that each methyl group is surrounded by four immobilized water OH groups.

8.1 Introduction

Hydrophobic interactions play an important role in many biochemical processes [18, 42, 62, 75, 79, 95, 111]. The folding of globular proteins, the self-assembly of lipid membranes and the binding of drugs to proteins are examples of processes driven by these interactions. In essence one can describe the hydrophobic effect as the tendency of apolar groups to associate in aqueous solution, thereby minimizing the total hydrophobic surface that is exposed to water.

The hydrophobic effect is intricately linked to the particular manner in which apolar compounds are solvated by water. It is well known that the dissolution of these compounds in water is accompanied by an anomalously large increase in the heat capacity of the solution. In the 1940s Frank and Evans introduced a model to account for this observation: they proposed that the water molecules around hydrophobic groups form rigid, ice-like structures, which they coined icebergs [31]. According to this model the freeing of entropy associated with the transfer of water molecules from the solvation shell to the bulk forms the origin of the hydrophobic effect.

The iceberg model of hydrophobic hydration is founded on thermodynamic measurements, and, as such, the evidence for the molecular picture that it presents remains indirect. During the past decades many researchers have attempted to confirm the iceberg model using more direct, structural methods. Among these techniques are neutron diffraction, dielectric relaxation and nuclear magnetic resonance (NMR). Neutron diffraction experiments can provide direct structural information about a solution by measuring the water-water radial distribution function (RDF). In the presence of hydrophobic solutes this RDF shows little change, from which it is concluded that the structure

of the water around hydrophobic groups is identical to that of the bulk liquid [15, 105]. NMR and dielectric relaxation, however, come to another conclusion [40, 48, 50, 92, 108]. These methods take a different approach at probing the water structure: the orientational dynamics of water molecules are used as an indicator of the rigidity of the hydrogen-bond network. Both methods show that the *average* mobility of water molecules in solutions containing hydrophobic solutes is decreased. However, as these methods measure a response that is averaged over all water molecules, the techniques cannot distinguish between water molecules in the bulk liquid and in the apolar solvation shell. As a consequence no information exists on the difference in behavior of the water molecules: is there an iceberg consisting of a single, well-defined layer of water molecules, or are many molecules slightly affected in their dynamical behavior? Summarizing, the experiments do not provide a consistent picture of the effect of hydrophobic groups on the structural dynamics of water.

Here we report on the use of polarization-resolved mid-infrared pump-probe spectroscopy to study the rotational motion of water molecules in the solvation shells of apolar molecules. An essential advantage of this method is that it probes the dynamics of water molecules on a sub-picosecond time scale, which is shorter than the exchange time of water molecules in the bulk liquid and the solvation shell. As a result the method allows the separation of the response of the aqueous solvation shell from that of the bulk.

8.2 EXPERIMENTAL

We studied the mobility of HDO molecules in aqueous solutions of amphiphilic compounds; the HDO concentration used was 8%. We performed our experiments using four compounds that contain a varying number of hydrophobic groups (figure 8.1): tetramethylurea (TMU), trimethylamine-N-oxide (TMAO), the amino acid proline and N-methylacetamide (NMA). These solutes all have an extremely high solubility in water (>10 m) despite their considerable hydrophobic character.

8.3 RESULTS

Figure 8.2a shows a delay scan at the center of the OD absorption band (2500 cm^{-1}) for a 4-m solution of TMAO. At this frequency we observe the bleaching of the fundamental transition of the OD-stretching vibration. The signal decays with a time constant of $\sim$ 2 ps, which is typical for the vibrational energy relaxation of HDO in H_2O [85, 96]. At other solute concentrations a similar decay time is observed, which shows that the relaxation of the OD vibration is not affected by the solute. The offset in the signal is the effect of sample heating as was discussed in the previous chapters.

The raw data have been corrected for the effects of heating using the method that was outlined in chapter 5 and employed in the study of urea solutions (chapter 7). A small refinement was made to the method; a detailed description of

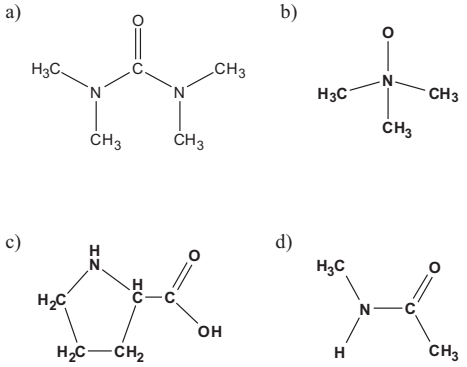

FIGURE 8.1. Molecular structure of the solutes used in the experiment. a) Tetramethylurea (TMU), b) Trimethylamine-N-oxide (TMAO), c) Proline and d) N-methylacetamide (NMA).

this refinement is provided in the next chapter. The solid line in figure 8.2 represents the fit to the relaxation model that is used for the correction procedure. From the fit we extract both the heating contribution to the signal (dashed line) and the bleaching of the excitation (dotted line). The latter contribution allows us to calculate the anisotropy of the excitation.

We have used the corrected signals to calculate the anisotropy. In figure 8.2b anisotropy decays are shown for TMAO solutions at four different concentrations. In all cases we observe a biexponential decay composed of a fast component ($\tau_{\rm rot}$) with a time constant $\leq$ 2.5 ps and a slow component with a time constant >10 ps. The fast component of ∼2.5 ps has also been observed in the reorientation of pure water, indicating that this component is to be associated with the reorientation of the bulk water molecules in the solution [85]. To determine the origin of the slow component we have varied the TMAO concentration. For each concentration we have fit the anisotropy to a mono-exponential decay with an offset ($R(t) = Ae^{-t/\tau_{\rm rot}} + B$); the offset represents the slow component, the time constant of which falls outside our experimentally accessible time range. In figure 8.3a the amplitude of the slow component is plotted as a function of the solute concentration. The amplitude is directly proportional to the fraction of immobilized OH groups, the maximum value of 0.4 representing 100% immobilization. We observe a linear dependency that flattens at very high concentrations. The linear relation indicates that the slow component is associated with the water molecules that are part of the solvation shell of the TMAO molecule. The long time constant ($\tau_{\rm rot} > 10$ ps) shows that these water molecules are strongly immobilized by TMAO. From the slope of the linear part of figure 8.3a we can calculate that the solvation shell of a TMAO molecule contains approximately 12 strongly immobilized OH groups.

As the TMAO molecule is amphiphilic we are faced with the question as to which part of the molecule is the cause of the immobilized water molecules: the

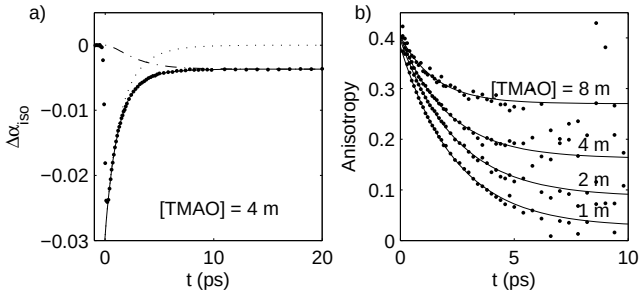

FIGURE 8.2. Time-resolved data for a 4-m solution of TMAO in isotopically diluted water. a) Delay scan taken at the center of the OD absorption band (2500 cm^{-1}). The solid, dashed and dotted lines represent the fit to the relaxation model, the heating contribution, and the true pump-probe contribution, respectively. b) Anisotropy decays of the OD vibration of HDO in H_2O at different TMAO concentrations. The solid lines represent fits to mono-exponential decays with an offset.

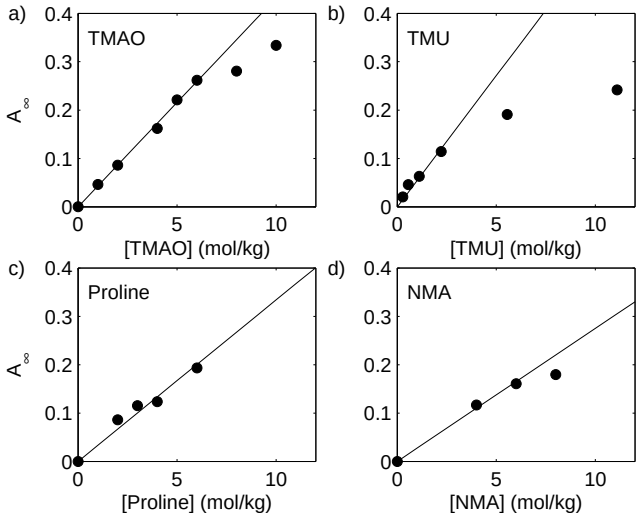

FIGURE 8.3. Long-time anisotropy of the OD vibration of HDO as a function of the concentration of the four different solutes: a) TMAO, b) TMU, c) Proline, and d) NMA. The uncertainty in the data points is 0.02.

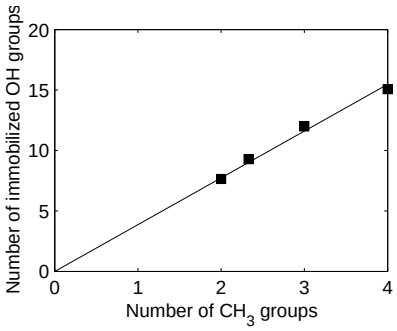

FIGURE 8.4. Number of immobilized water OH groups as a function of the equivalent number of CH_3 groups in the solute molecule.

hydrophilic NO group or the hydrophobic methyl groups? To investigate this issue we have varied the nature of the solute and repeated our measurements. We observe a similar pattern for each of the remaining solutes in figure 8.1. The anisotropy decays biexponentially with a fast component ($\sim$2.5 ps) and a slow component (>10 ps). At low concentrations the amplitude of the slow component scales linearly with the solute concentration (figures 8.3b-d). For each of the solutes in figure 8.1 we have determined the number of OH groups immobilized per solute molecule. We have summarized these results in figure 8.4, where the number of immobilized water molecules is plotted versus the equivalent number of CH_3 groups in the solute molecule. The observed linear relation unambiguously shows that the immobilized water molecules are part of the hydration shell around the *hydrophobic* methyl groups of the solutes. Apparently the *hydrophilic* groups of the solutes do not lead to the immobilization of water molecules. The slope of the graph in figure 8.4 has a value of 3.9, indicating that every methyl group is responsible for the immobilization of approximately 4 water OH groups. At high solute concentrations the curves in figure 8.3 flatten, which shows that for these concentrations fewer than 4 OH groups are immobilized per methyl group. This is explained by the fact that in these solutions part of the immobilized OH groups are shared by different solute molecules.

We now consider the physical mechanism that underlies the immobilization of water molecules in the vicinity of hydrophobic groups. One could presume that these immobilized molecules are connected by very strong hydrogen bonds, resembling the hydrogen bonds encountered in ice. However, as appealing as this notion may be, it cannot be correct. The fact that the addition of the hydrophobic solutes does not shift the OD-stretch vibration to the red indicates that the hydrogen bonds in the investigated solutions are of a strength comparable to those in pure water.

A number of molecular dynamics studies on liquid water have appeared in the past years. Sciortino et al. have shown that the relatively high orientational mobility of pure water is related to the presence of defects (i.e. five-coordinated

water molecules) in the tetrahedral hydrogen-bond network of liquid water [88]. They have suggested that the slowing down of water dynamics around hydrophobic groups is the consequence of a steric effect, which prevents the creation of five-coordinated water molecules around these groups. Recently, Laage and Hynes proposed a detailed mechanism for water reorientation involving five-coordinated water molecules [56]. In this mechanism the pathway for reorientation involves a rotating water molecule that concertedly breaks a hydrogen bond with an overcoordinated first-shell neighbor and reforms one with an undercoordinated second-shell neighbor. In another molecular dynamics study by Sharp et al. the effect of hydrophobic solutes on the structure of water was investigated [35]. These researchers observed that hydrophobic solutes tend to preferentially displace water molecules that overcoordinate a second water molecule, providing a rationale for why hydrophobic solutes lower the amount of network defects. These studies together with our results form compelling evidence for the notion that the immobilization of water molecules around a hydrophobic solute arises from a steric effect, in which the hydrophobic group prevents a fifth water molecule from approaching a tetrahedrally coordinated water molecule, and as such prevents the molecule to reorient.

The slowing down of the orientational dynamics of water in aqueous solutions of hydrophobic species was also observed in an NMR study, in which the reorientation of water was compared in aqueous solutions of urea and alkylated ureas [92]. For aqueous solutions of tetramethylurea the NMR measurements show a dramatic slowing down of the water reorientation as the tetramethylurea concentration is increased: at a TMU concentration of 2.5 m the *average* reorientation is slowed down by a factor of 2. In contrast, in aqueous urea the average reorientation time of the water molecules was observed to increase only negligibly with increasing urea concentration. This is in agreement with our results from chapter 7 which showed that urea does not affect the orientational dynamics of the majority of the water molecules. These findings support the results from the present chapter, which show that the methyl groups of tetramethylurea slow down the water reorientation.

It has been suggested by several researchers that two regimes can be distinguished as far as hydrophobic effects are concerned: the regime of a small hydrophobic solute and that of a large hydrophobic particle or a plane surface [18,99]. Small hydrophobic solutes can be accommodated by the hydrogen-bond network of water without breaking hydrogen bonds, whereas an extended hydrophobic surface can only be solvated if hydrogen bonds are sacrificed. The notion that the hydrogen-bond network of water does not have to be perturbed in order to solvate small hydrophobic particles corroborates the interpretation of our results.

It is interesting to compare the number of immobilized water molecules surrounding a methyl group with the size of its hydration sphere, as it follows from neutron diffraction. Neutron diffraction data on methanol solutions in water were reported by Soper and Finney [94]. By integrating the first peak in the carbon-oxygen radial distribution function, these authors find that the first solvation shell of the methyl group contains about 10 water molecules

(20 OH groups). Let us assume that the solvation structure of the methyl group of methanol is representative of that of a methyl group in general. Our experiments show that only 4 OH groups are immobilized per methyl group, which means that not all OH groups in the solvation shell of a methyl group have the same configuration. Apparently, approximately 80% of the OH groups in the hydration shell are in 'open' configurations that can be approached by new hydrogen-bonding partners and therefore show bulk-like dynamics. Only 20% of the OH groups in the hydration shell represent immobilized OH groups; these OH groups are in such close proximity to the methyl group that there is no space for the creation of network defects.

8.4 Conclusions

We conclude by returning to the iceberg model of Frank and Evans. Our results provide a molecular picture of these icebergs: they consist of four strongly immobilized water OH groups for every methyl group in solution. They are the consequence of a decrease in the configurational space available to water molecules around hydrophobic solutes. This notion also explains Frank and Evans' original observation of a decreased entropy upon the dissolution of hydrophobic compounds in water. The structure of the iceberg, however, is not the ordered structure observed in ice, but it rather resembles the disordered hydrogen-bond network of bulk water: the icebergs are ice-like from a dynamical perspective but water-like as far as structure is concerned. This provides an explanation for why hydrophobic icebergs were not previously observed using structural methods.

9 Strong slowing down of water reorientation in mixtures of water and tetramethylurea

We use mid-infrared pump-probe spectroscopy to study the ultrafast dynamics of HDO molecules in mixtures of tetramethylurea (TMU) and water. The composition of the studied solutions ranges from pure water to an equimolar mixture of water and TMU. We find that the vibrational relaxation of the OD-stretching vibration of HDO proceeds via an intermediate level in which the molecule is more strongly hydrogen bonded than in the ground state. As the TMU concentration is increased, the lifetime of the excited state and of the intermediate increase from 1.8 ps to 5.2 ps and from 0.7 ps to 2.2 ps, respectively. The orientational relaxation data indicate that the solutions contain two types of water molecules: bulk-like molecules that have the same reorientation time constant as in the pure liquid ($\tau_{\rm rot} = 2.5$ ps) and molecules that are strongly immobilized ($\tau_{\rm rot} > 10$ ps). The immobilized water molecules turn out to be involved in the solvation of the methyl groups of the tetramethylurea molecule. The fraction of immobilized water molecules grows with increasing TMU concentration, reaching a limiting value of 60% at very high concentrations.

9.1 Introduction

Concentrated mixtures of water and amphiphilic molecules can have interesting properties. For instance, in a neutron diffraction study it was shown that the structure of a methanol-water mixture (molar ratio 7:3) is not homogeneous on a molecular scale [23]. Instead, the mixing of the two components is incomplete and the water is present as hydrogen-bonded clusters in a methanol matrix. Here we study mixtures of an amphiphilic compound and water. As the amphiphilic compound, we use tetramethylurea (TMU), which has the advantage that it does not contain any hydroxyl groups that could overshadow the water response.

In this chapter we present measurements of the ultrafast dynamics of HDO molecules in mixtures of water and tetramethylurea (TMU) spanning the full concentration range: from pure water to nearly pure TMU. These experiments form an extension to the previous chapter, in which TMU concentrations up to 10 mol/kg were studied. The measurements shed light on the gradual breakdown of the hydrogen-bond network of water, as it occurs when moving from pure water, to water with impurities, and finally to an apolar matrix in which water itself is present as the impurity.

9.2 EXPERIMENTAL METHODS

Our samples consist of mixtures of TMU and water. Since we study mixtures over a wide composition range, we do not use the TMU concentration to specify the composition, but we rather use the symbol w, which represents the number of TMU molecules present in the solution per water molecule,

$$w = \frac{[\mathrm{TMU}]}{[\mathrm{H_2O}]}. \tag{9.1}$$

To the water we have added 4% of heavy water (D_2O), and as a consequence 8% of the water is present as HDO molecules. The low HDO concentration ensures that no resonant intermolecular energy transfer occurs between different HDO molecules. The thickness of our samples varies between 25 μm and 200 μm and is chosen such that an optical density of $\sim$1 is obtained. The sample cell consists of two CaF_2 windows held apart by a teflon spacer of appropriate thickness.

9.3 RESULTS AND INTERPRETATION

9.3.1 LINEAR SPECTRA

Figure 9.1 displays the linear spectra of HDO in pure H_2O and in two solutions of TMU. The water-TMU background was subtracted from these spectra, so that they only display the absorption due to the HDO molecules. The frequency region shown corresponds to the absorption by the OD-stretching vibration. A blueshift of the band is observed with increasing TMU concentration, which is indicative of a decrease of the average hydrogen-bond strength in the network of water molecules [71]. However, we note that very high concentrations are needed to cause a significant weakening of the hydrogen-bond network: for the solution with $w = 0.2$, corresponding to only five water molecules per TMU molecule, only a small shift is observed. Apparently the hydrogen-bond network of water can accommodate the TMU molecules without being significantly perturbed. A considerable weakening of the hydrogen bonds only occurs for concentrations that are so high that they prevent the formation of a connected network of water molecules.

9.3.2 ISOTROPIC TRANSIENT SPECTRA

Figure 9.2 shows transient spectra for a TMU solution with $w = 0.1$. At short delays (0.5 ps and 2 ps) we observe a transient spectrum that is typical of the OD vibration of HDO: a decreased absorption around 2500 cm^{-1} due to the bleaching of the fundamental transition, and an induced absorption for frequencies $<$2430 cm^{-1} caused by the excited vibrational state. The spectrum at 20 ps is the temperature-difference spectrum, the characteristics of which have been described extensively in chapter 5.

In figure 9.3 we have plotted delay scans for different frequencies in the transient spectrum of figure 9.2. The top and bottom panel show a bleach

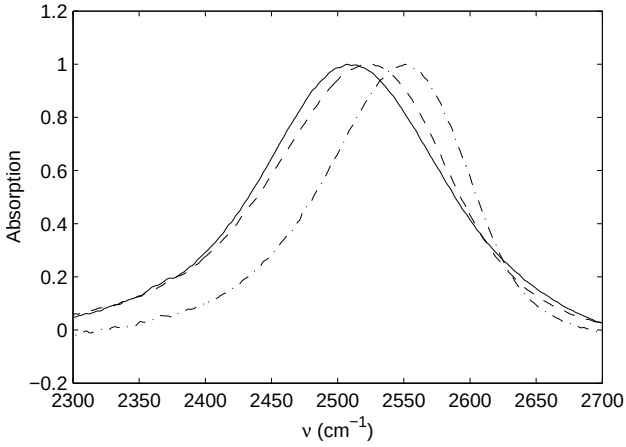

FIGURE 9.1. Linear spectra of HDO in H_2O with different amounts of added tetramethylurea. The spectra are corrected for the H_2O and TMU background so that only the absorbtion due to the HDO molecule is visible. The solid line refers to the spectrum corresponding to $w = 0$ (HDO in H_2O), the dashed line to $w = 0.2$ and the dashed-dotted line to $w = 1$.

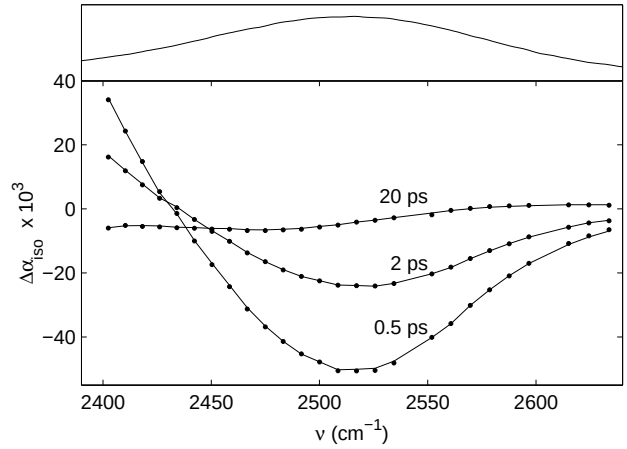

FIGURE 9.2. Transient spectra (dots) of a solution of TMU in HDO/H_2O corresponding to $w = 0.1$ at delays of 0.5, 2 and 20 ps. The solid line represents a fit to the relaxation model described in the text. The top panel shows the linear spectrum.

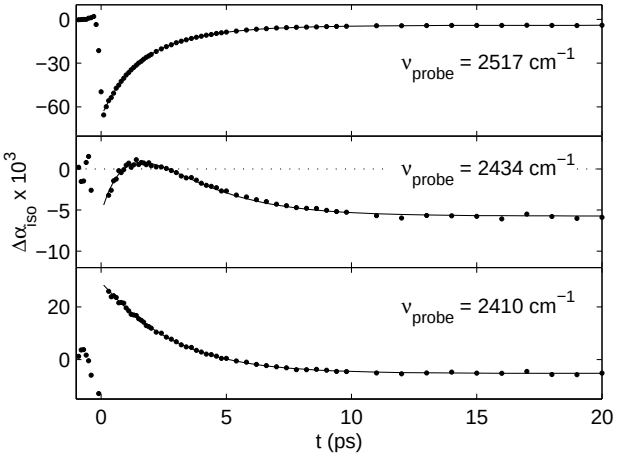

FIGURE 9.3. Delay scans for a TMU solution corresponding to $w = 0.1$ at different probe frequencies. The dots represent the experimental data points and the solid line is the fit to the relaxation model described in the text.

and an induced absorption, respectively, that decay on a ∼2 ps timescale. The middle panel shows a delay scan at an intermediate frequency that displays more complicated behavior. Here a competition is observed between a decaying bleach and an ingrowing heating signal, which is a bleach at this frequency. The fact that the signal turns over indicates that the heating is delayed with respect to the relaxation of the OD vibration, as has been described in chapter 5 when discussing the relaxation of HDO in pure water. However, this explanation does not yet account for one aspect of the considered signal: the fact that the signal rises temporarily above zero: an induced absorption cannot arise from the sum of two contributions that both have the character of a bleach. We shall return to this issue when discussing the relaxation mechanism of the OD vibration.

In order to describe the time-dependence of the transient spectra of HDO in solutions of TMU, we turn to the mechanism that was used in chapter 5 for the relaxation of HDO in pure water. Here we will use a slightly modified version of this mechanism, which is presented in figure 9.4. The first step in the relaxation is the decay of the excited OD vibration to an intermediate level. This transfer occurs with a rate constant k_1 $(1/\tau_1)$. Subsequently the intermediate level decays to the ground state (with a rate constant $k_* = 1/\tau_*$), which is accompanied by thermalization of the vibrational energy. This leads to a temperature rise and its effects are incorporated into the model by attributing a different spectrum to the heated ground state (0') than to the ground state (0). A difference as compared to the mechanism from chapter 5 is that a distinct spectrum is also assigned to the intermediate level. The spectra of the three states are denoted by the symbols σ_{01}, σ_{12}, σ^*_{01} and σ'_{01}.

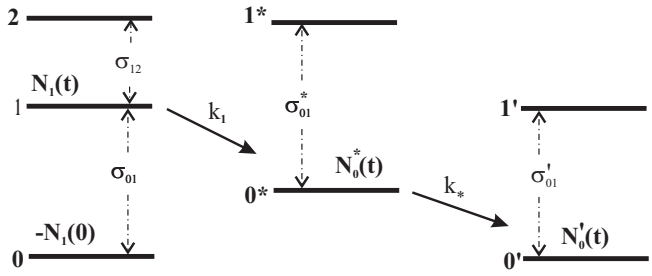

FIGURE 9.4. Model used to describe the relaxation of the OD vibration of the HDO molecule in aqueous TMU solutions. The excited state first decays to an intermediate state that has a different spectrum than the ground state. The subsequent decay of this level leads to thermalization of the vibrational energy and, as such, to heating of the sample.

The absorption change that follows from this relaxation model is given by

$$\begin{aligned}\Delta\alpha(\omega,t) &= N_1(t)\sigma_{12}(\omega) - [N_1(0)+N_1(t)]\,\sigma_{01}(\omega) + \\ &\quad N_0^*(t)\sigma_{01}^*(\omega) + N_0'(t)\sigma_{01}'(\omega), \\ &= N_1(t)\sigma_{12}(\omega) + \\ &\quad [-N_1(0) - N_1(t) + N_0^*(t) + N_0'(t)]\,\sigma_{01}(\omega) + \\ &\quad \Delta\sigma_{01}'(\omega)N_0'(t) + \Delta\sigma_{01}^*(\omega)N_0^*(t). \end{aligned} \tag{9.2}$$

where $\Delta\sigma_{01}' = \sigma_{01}' - \sigma_{01}$ and $\Delta\sigma_{01}^* = \sigma_{01}^* - \sigma_{01}$. The expressions for the populations are the same as in chapter 5 (section 5.3). By substituting for these populations we arrive at the following expression

$$\begin{aligned}\Delta\alpha(\omega,t)/N_1(0) &= \{\sigma_{12}(\omega) - 2\sigma_{01}(\omega)\}\,e^{-k_1 t} + \\ &\quad \Delta\sigma_{01}'(\omega)\left\{\frac{k_1}{k_* - k_1}e^{-k_* t} - \frac{k_*}{k_* - k_1}e^{-k_1 t} + 1\right\} + \\ &\quad \Delta\sigma_{01}^*(\omega)\frac{k_1}{k_* - k_1}\left(e^{-k_1 t} - e^{-k_* t}\right). \end{aligned} \tag{9.3}$$

This expression consists of three terms. The first term represents the combined bleaching of the fundamental transition and induced absorption of the excited state; the second term represents the ingrowing heating signal; finally, the last term is a correction for the fact that the intermediate state may have a spectrum that is different from that of the ground state. In chapter 5 this term was neglected because it was assumed that $\Delta\sigma_{01}^* = 0$.

For each TMU solution a fit of equation 9.3 to the time-dependent transient spectrum has been performed. Hereby the frequency-dependent cross-sections, $\sigma_{12}(\omega) - 2\sigma_{01}(\omega)$, $\Delta\sigma_{01}'(\omega)$ and $\Delta\sigma_{01}^*(\omega)$, were allowed to vary freely. Thus each time-dependent transient spectrum is characterized by three cross-section spectra and two rate constants (k_1 and k_*). In figures 9.2 and 9.3 the solid lines

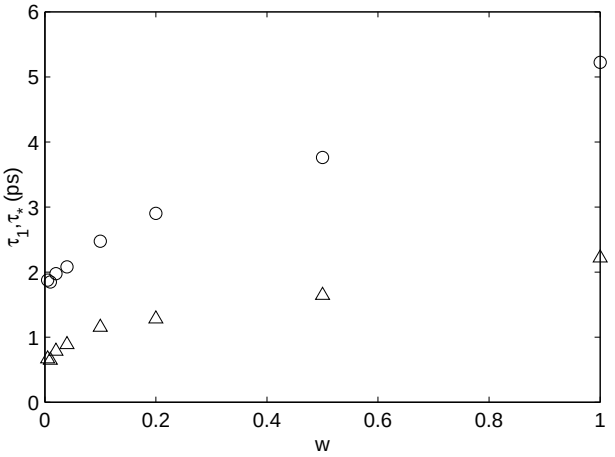

FIGURE 9.5. Relaxation times of the OD vibration of HDO as a function of the composition of the solution. The circles represent τ_1 and the triangles τ_*.

show the resulting fit for the $w = 0.1$ solution. It can be seen that this relaxation model provides an excellent description of the data. For the other solutions the fits are of similar quality, indicating that the relaxation mechanism does not change as the composition of the solution is varied. The two relaxation time constants, however, do vary, and they both increase as the TMU concentration is increased (figure 9.5); τ_1 increases from 1.8 ps to 5.2 ps and τ_* increases from 0.7 ps to 2.2 ps. This finding reflects the slowing down of the vibrational relaxation of the HDO molecule upon truncation of the hydrogen-bond network of water.

From the fit we obtain the time-dependent populations of the three levels in the relaxation. We have plotted these populations in figure 9.6 for the $w = 0.1$ solution. We recognize the mono-exponentially decaying excited state and the heated ground state that grows in biexponentially. The intermediate state starts with no population at $t = 0$, becomes populated up to a maximum, and subsequently tracks the decay of the excited state. The population dynamics are qualitatively similar for the other solutions.

Apart from the populations the fits also provide us with the spectral shapes that correspond to these three populations. We have plotted these spectral components in figure 9.7 for three TMU solutions. The spectral shape corresponding to the excited state population resembles the transient spectrum at short delay, as is to be expected from the fact that at these delays only the excited state is populated. Similarly, the spectrum of the heated ground state is identical to the transient spectrum at long delays. For the intermediate state, however, we observe a spectrum that cannot be inferred directly from the data. The spectral shape of $\Delta\sigma^*_{01}$ shows that at all frequencies the intermediate state has an increased absorption in comparison to the ground state. As far as the

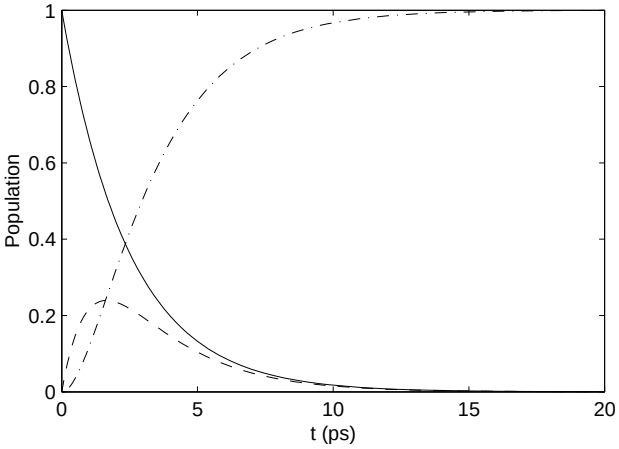

FIGURE 9.6. Populations of the three states in the relaxation model for the TMU solution with $w = 0.1$. The solid line is the excited state population, the dashed line the intermediate state population, and the dashed-dotted line represents the population of the heated ground state.

heating spectrum is concerned, we note that its amplitude decreases relative to that of the two other spectra as the TMU concentration is increased. This is explained by the fact that the sample thickness was increased upon increasing the TMU concentration, in order to maintain the same optical density by HDO. Since the pump energy is thus spread over a larger volume, the resulting temperature jump decreases in magnitude.

In chapter 5 the spectrum of the intermediate state was assumed to be the same as that of the ground state. Indeed, we find that at low TMU concentrations the transient spectra of the TMU solutions can very well be fit using only the first two terms in equation 9.3. At high TMU concentrations, however, this is no longer possible. The reason why two spectral components suffice at low concentrations is that the heating signal can to some extent compensate for the spectral component associated with the intermediate state. At high TMU concentrations the heating signal decreases in amplitude, so that it can no longer play this role. The increased absorption of the intermediate level also explains the overshoot to positive values observed in the delay scan in the middle panel of figure 9.3. In fact, the overshoot unambiguously proves the necessity of introducing the intermediate-state spectrum into the relaxation model, and it rules out the possibility that the spectrum is merely a fitting artifact.

We would like to stress that the increased absorption of the intermediate state is likely to be a general feature of the relaxation pathway of the HDO molecule, which is independent of the solvent (be it pure H_2O or aqueous TMU). The effect of the intermediate state is only more clearly observed for samples in which the HDO molecules are effectively diluted, so that the thermal effect

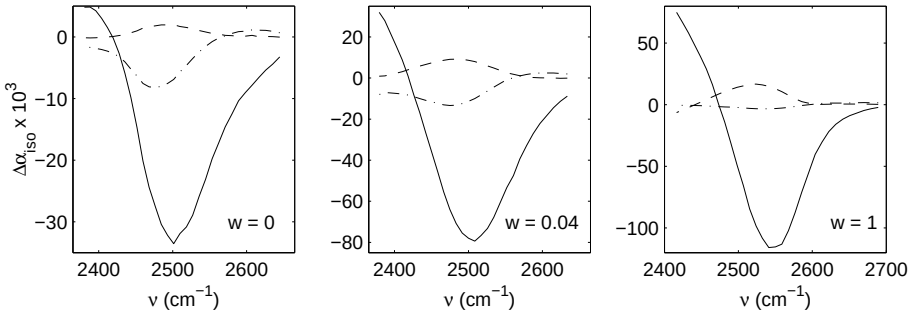

FIGURE 9.7. Decomposition of the transient spectra of TMU-solutions with $w = 0$, $w = 0.04$ and $w = 1$ into the three spectral shapes that follow from the relaxation model. The solid line represents the ground state bleach and excited state absorption. The dashed line is the spectrum of the intermediate state, and the dashed-dotted line corresponds to the heating spectrum.

is diminished. The reason that it is difficult to observe the effect for HDO in pure H_2O is that one cannot use thick samples because of the relatively strong background absorption at $\sim$2500 cm^{-1} of the H_2O solvent.

9.3.3 ANISOTROPY DYNAMICS

Using the results from the fit, we have corrected the raw data for the ingrowing heating, and we have used the corrected signals to calculate the anisotropy. In figure 9.8 we have plotted the anisotropy decays for a few TMU solutions of different composition. The probe frequencies correspond to the peak position of the bleach. We observe biexponential decays with a fast decay time of $\sim$2.5 ps and a slow component that cannot be fully resolved but that has a time constant >10 ps. The fast time constant does not show any significant variation with solution composition (figure 9.9a); a slight increase is only observed for the most concentrated solution. The value of 2.5 ps for this time constant is identical to the reorientation time of HDO in pure water (chapter 5). In figure 9.9b we have plotted the amplitude of the slow component versus the solution composition. We observe a strong variation of the amplitude that is linear at low concentrations ($w < 0.05$) and flattens at high concentrations. The data at low concentrations is identical to the data that was presented in the previous chapter.

As was explained in chapter 8, these observations indicate that in TMU solutions a partitioning of water molecules occurs into two fractions. One fraction is composed of bulk-like water molecules that display the same orientational dynamics as in the pure liquid; the other fraction consists of water molecules that are strongly immobilized, in the sense that they display much slower orientational dynamics than the bulk water molecules. Here we observe that this partitioning persists over the entire concentration range. In chapter 8 it was shown

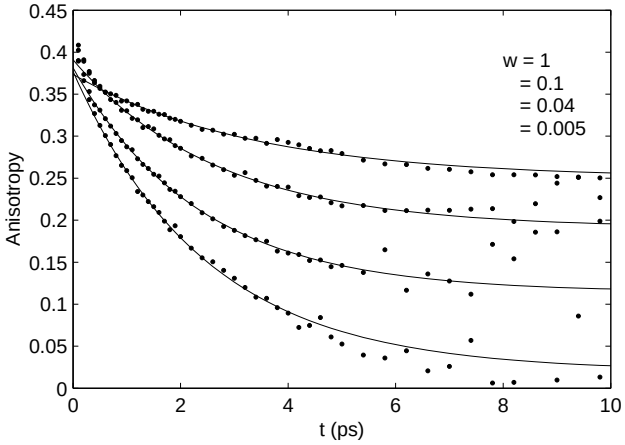

FIGURE 9.8. Anisotropy decay of the OD vibration of HDO in TMU solutions of varying composition. For every solution the probe frequency corresponds to the maximum of the bleach.

that the immobilized water molecules are to be associated with the solvation shell of a TMU molecule. Consequently, the upper limit for the reorientation time of these immobilized water molecules is given by the reorientation time of the TMU solute. From the slope of the linear part of the graph in figure 9.9b we calculate that every TMU molecule is responsible for the immobilization of 15 ± 2 water OH groups, which amounts to 4 OH groups per TMU methyl group. At high concentrations the solvation shells of different TMU molecules overlap, which explains the deviation from linear behavior observed at these concentrations. At very high concentrations saturation is observed at a value of the anisotropy of 0.25, from which we conclude that 60% of all water molecules are immobilized in these solutions.

In figure 9.10 we compare the anisotropy decay on the red side of the spectrum with that on the blue side for two solutions: one with a low TMU concentration and one with a high concentration. For the low TMU concentration we see practically no difference between the anisotropy decays on the red and blue side of the spectrum. This observation is in agreement with the results for HDO in pure water from chapter 5, which showed no dependence of the anisotropy decay on the probe wavelength. For the concentrated solution corresponding to $w = 1$, however, we observe that the anisotropy decays faster on the blue side of the spectrum than on the red side. This spectral dependence of the anisotropy reflects the heterogeneity in the local environments of water molecules, that apparently occurs in highly concentrated solutions of TMU.

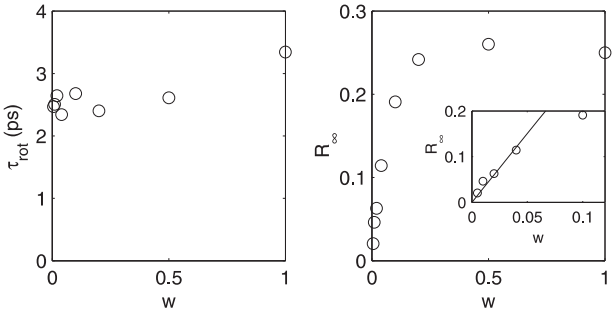

FIGURE 9.9. a) Time constant of the fast component in the anisotropy decay of the OD vibration of HDO as a function of the composition of the solution. The probe frequencies correspond to the center of the absorption bands. b) Amplitude of the slow component in the anisotropy decay as a function of the composition of the solution (same probe frequencies as above). The inset shows the same graph with the x-axis expanded. The solid line represents a linear fit to the first four points.

9.4 DISCUSSION

We have shown that the relaxation of the OD vibration of HDO proceeds through an intermediate level that has an increased absorption relative to the ground state. It is reasonable to assume that the intermediate state is a state in which a low-frequency mode is excited and that this excitation affects the frequency and cross-section of the ground-state spectrum of the OD vibration via an anharmonic interaction. The spectral shape of $\Delta\sigma_{01}^{*}$ shows an increased absorption in the center and on the red side of the spectrum. A possible explanation for this observation could be that the vibrational relaxation of the OD vibration leads to the excitation of the hydrogen-bond stretching vibration. The excitation of this low-frequency vibration results in a broadening of the hydrogen-bond length distribution. Because the cross-section of the OD vibration increases strongly when the hydrogen-bond strength increases (and therefore when moving to the low-frequency side of the spectrum), this broadening will primarily lead to an increase in the spectral intensity on the red side of the spectrum.

The results of the anisotropy measurements point to the presence of strongly immobilized water molecules in the solvation shell of the TMU solute. In the previous chapter it was explained that this immobilization is to be attributed to the hydrophobic methyl groups. Water reorientation occurs through a mechanism that involves the concerted breaking of a hydrogen bond and its reformation with a new partner [56]. For this to occur a water molecule has to adopt a temporary fivefold coordination, which can be interpreted as the formation of a defect in the tetrahedral hydrogen-bond network of water. It is the formation of these network defects that constitutes the rate-limiting step in water reorientation. Bulky methyl groups prevent the formation of such defects in their

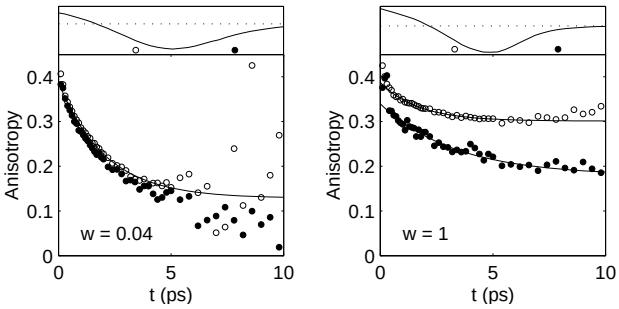

FIGURE 9.10. Dependence of the anisotropy decay on the probe frequency for TMU solutions with $w = 0.04$ (a) and $w = 1$ (b). The solid lines are fits of monoexponentials with an offset. The top panels display the transient spectra, below which the probe frequencies are marked using the symbols from the lower panel.

vicinity and, as such, they slow down water reorientation. A dramatic illustration of the immobilizing action of methyl groups is provided by comparing the present results to the results from chapter 7 on aqueous urea. In chapter 7 it was shown that water reorientation remained essentially unaffected by the presence of extremely high concentrations of urea (up to 12 mol/kg). Only one water OH group per urea molecule was slowed down in its reorientation. When the polar NH groups of urea are substituted by methyl groups, however, the molecule TMU is obtained, which immobilizes no less than 15 water OH groups.

At high TMU concentrations the anisotropy becomes dependent on the probe frequency, decaying faster on the blue side of the spectrum than on the red side (figure 9.10b). This observation points to the existence of structures in the hydrogen-bond network that are relatively long-lived and do not interconvert on a 10 ps timescale. Below we investigate the nature of these structures.

At high TMU concentrations the amplitude of the slow component in the anisotropy displays an asymptotic behavior as a function of the TMU concentration. The fact that the limiting value is practically reached at a composition of $w = 0.2$ suggests that beyond this concentration the average environment of a water molecule no longer changes with increasing TMU concentration. A priori one can envision two possibilities for the structure of these solutions, which contain an excess volume of TMU: either the water is present as isolated water molecules, hydrogen bonded to TMU, or it is present as clusters of water molecules. Let us consider the first possibility and see whether it can explain the observed anisotropy dynamics. Water molecules that are present as isolated molecules are likely to have one OH group that is hydrogen bonded to TMU and another that is dangling in a hydrophobic environment. In this situation the slow component in the reorientation would be the consequence of the hydrogen-bonded OH groups and the fast component would be caused by the unbound OH groups. However, since a carbonyl group can only bind two water molecules, it is difficult to understand how this behavior can already

set in at a composition of $w = 0.2$, corresponding to five water molecules per TMU molecule. Therefore, the option that the water is present as water clusters seems more plausible. This structure accounts for the fact that the environment of a water molecule remains the same beyond a certain TMU concentration. Moreover, molecular dynamics simulations have shown that water indeed forms clusters in hydrophobic cavities [106]. The immobilization of water molecules in these clusters is likely to proceed through a mechanism that resembles the mechanism in dilute TMU solutions. That is, the immobilized OH groups are located in the vicinity of the methyl groups and cannot be approached by a new hydrogen-bonding partner; water molecules in the interior of the cluster are responsible for the fast reorientation because of their ability to become fivefold coordinated [56]. However, there is another type of OH group that we need to consider. Due to the finite size of a cluster not all water molecules can form four hydrogen bonds, so that there will also be unbound OH groups, which are mobile. We conclude that at high TMU concentration the mobile OH fraction contains both hydrogen bonded OH groups and unbound OH groups. The unbound OH groups absorb on the blue side of the spectrum; as a consequence the mobile fraction is largest in this frequency region, resulting in a lower end level in the anisotropy (figure 9.10b).

9.5 Conclusions

We studied the vibrational relaxation and orientational dynamics of HDO molecules in aqueous solutions of tetramethylurea (TMU), the composition of which varied from pure water to an equimolar mixture of water and TMU. The vibrational relaxation of the OD vibration of HDO was found to proceed via an intermediate level in which the HDO molecule is more strongly hydrogen bonded than in the ground state. This aspect of the intermediate level is likely to also apply for HDO in pure water, but it was not previously observed because the effect was always obscured by a strong heating signal. When increasing the TMU concentration the lifetimes of the excited state and of the intermediate state increase from 1.8 ps to 5.2 ps and 0.7 ps to 2.2 ps, respectively.

By studying the orientational dynamics we discovered that the water molecules in these solutions are partitioned into two fractions: one fraction displays bulk-like dynamics and reorients with the same time constant as in the bulk liquid ($\tau_{\mathrm{rot}} = 2.5$ ps); the other fraction is immobilized and displays much slower orientational dynamics ($\tau_{\mathrm{rot}} > 10$ ps). The immobilized fraction turns out to be part of the hydrophobic hydration shell of the TMU molecule, and we found that at low concentrations every TMU molecule immobilizes 15 ± 2 water OH groups. The immobilization of water molecules is the consequence of a steric effect in which the methyl groups hinder the formation of network defects in the hydrogen-bond network of water; since these network defects are known to catalyze the reorientation of water molecules, their absence explains the observed immobilization. At high TMU concentrations the structure of the solution becomes heterogeneous with the water molecules present in the form of clusters in the TMU matrix.

7 The effect of urea on the structural dynamics of water

We use polarization-resolved mid-infrared pump-probe spectroscopy to study the effect of urea on the structure and dynamics of water. Surprisingly, we find that even at high concentrations of urea (8 M) the orientational dynamics of most water molecules are the same as in pure liquid water, showing that urea has a negligible effect on the hydrogen-bond dynamics of these molecules. However, a small fraction of the water molecules (approximately one water hydroxyl group per urea molecule) turn out to be strongly immobilized by urea, displaying orientational dynamics that are over 6 times slower than in bulk water. A likely explanation is that these water molecules are tightly associated with urea, forming specific urea-water complexes. We provide a discussion of these results in the light of the protein denaturing ability of aqueous urea.

7.1 Introduction

Solutions of urea in water display a number of interesting properties: hydrocarbons dissolve more readily in them than in pure water, and concentrated solutions can be used to denature proteins in a reversible way. The wish to understand these properties has triggered a great deal of research regarding the structure of aqueous solutions of urea [4,8,9,28,44,45,47,50,51,92,93,107,109]. An important question that is encountered throughout the literature is to what extent the hydrogen-bond network of water is perturbed by the incorporation of a urea molecule, as one of the models explaining protein denaturation by urea is built on the assumption that urea strongly alters the hydrogen-bond structure of water [32]. The urea-water system has been studied using a variety of experimental and theoretical techniques, all of which shed light on a different aspect of the system. Linear infrared and Raman spectroscopies can provide structural information about the hydrogen-bond network, but they depend on simulations to unravel the effect of intermolecular interactions on spectral band shapes [89]. Neutron diffraction experiments produce atom-atom radial distribution functions, and, as such, form more direct methods to obtain structural information [93]. A different class of experimental techniques probes the hydrogen-bond network by observing the *dynamics* of water molecules. A stiffening of the network is revealed by the slowing down of the water dynamics, whereas faster dynamics are indicative of the weakening of the network. Among these methods are dielectric relaxation [50], nuclear magnetic resonance (NMR) [92], and optical Kerr effect (OKE) spectroscopy [45]. Dielectric relaxation and OKE provide dynamical information down to the picosecond timescale

but probe the response of the solution as a whole, making it difficult to separate the water response from the urea response. NMR experiments selectively probe the dynamics of water, but determine a time-averaged response, so that water molecules in the urea solvation shell cannot be distinguished from molecules in the bulk. As a result, it is not yet clear to what extent the hydrogen-bond structure of water is changed by the addition of urea.

Here we report on the use of mid-infrared pump-probe spectroscopy [70, 85, 96] to study the effect of urea on the hydrogen-bond network of water. This technique selectively probes the dynamics of water molecules on a picosecond timescale. On this timescale there is no exchange between water molecules inside the urea solvation shell and the bulk, and the method therefore has the potential to distinguish between these two water species.

7.2 EXPERIMENTAL

We used the orientational mobility of HDO molecules dissolved in H_2O (8%) to probe the local rigidity of the hydrogen-bond network of urea-water mixtures of different proportions. The orientational mobility of HDO was measured through polarization resolved pump-probe spectroscopy of the OD-stretching vibration. The samples used for our experiments are 8% solutions of HDO in H_2O to which up to 8 M of urea has been added. The mid-infrared pump-probe measurements are carried out in a static cell with an optical path length of approximately 25 μm.

The ND-stretching vibration of urea (ND is formed from NH by isotopic exchange with isotopically labeled water) absorbs in the same wavelength region as the OD-stretch vibration. Its contribution to the pump-probe signal at delays larger than 1 ps, however, is negligible because of a number of factors: the ND-vibration is present at a lower concentration than the OD vibration, its cross-section (which enters quadratically in the pump-probe signal) is approximately twice as small, and, most importantly, its lifetime is much shorter than that of the OD-vibration ($\sim$0.7 ps vs 1.8 ps).

7.3 RESULTS

Figure 1 shows transient spectra of the OD-stretching vibration of HDO in a 4 m solution of urea. The transient spectra are plotted for a pump-probe delay of 0.6 ps and 20 ps. At 0.6 ps the bleaching of the fundamental transition is observed around 2500 cm^{-1}. For frequencies below 2410 cm^{-1} there is an induced absorption due to the absorption of the excited state. At 20 ps vibrational relaxation is complete, and we observe the effects of heating. In order to correct for these effects we follow the approach that was outlined in chapter 5. We have fit the two-step relaxation model from chapter 5 to the data in figure 7.1 (solid lines); this yields a lifetime of the OD vibration of 1.8 ± 0.1 ps and of the intermediate state of 1.0 ± 0.1 ps. In figure 7.2a we present the absorption change as a function of delay for a probe frequency of 2500 cm^{-1}. The fit allows

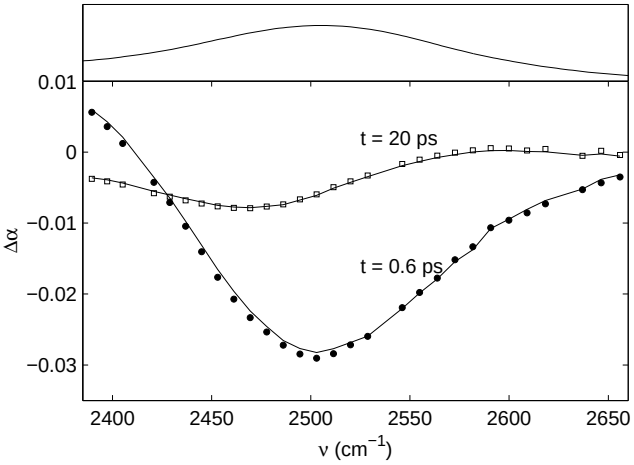

FIGURE 7.1. Transient spectra of HDO in a 4 m solution of urea in water. The spectra are plotted for a pump-probe delay of 0.6 ps and of 20 ps. The solid lines represent fits to the two-step relaxation model described in the text. The top panel shows the linear infrared spectrum.

us to separate the two contributions to the signal: the decaying bleach of the OD-vibration (dotted line) and the ingrowing heating signal (dashed line). We used the same model to analyze the transient spectra of the other urea solutions. Figure 7.2b shows that the two time constants do not vary with the urea concentration, indicating that urea has a negligible effect on the vibrational relaxation of water.

The parallel and perpendicular pump-probe signals were corrected for the ingrowing heating, and the corrected signals were used to compute the anisotropy. Figures 7.3a and b show the resulting anisotropies at the maximum of the bleach for two urea concentrations. No significant dependence of the anisotropy on the probe wavelength was observed. The two curves can be well described by mono-exponential decays with a non-zero end level. This points to the presence of a fast and a slow process in the reorientation of the water molecules. The decay time constant of the fast process is plotted as a function of urea concentration in figure 7.4a. This time constant does not vary significantly with concentration and has a value of roughly 2.5 ps. The slow component has a time constant that is larger than 15 ps. Information about the origin of these two components can be obtained from the concentration dependence of their amplitudes. In order to extract the amplitudes of the two components we have simultaneously fit all anisotropy curves to biexponentials. These biexponentials had the same two decay time constants for all anisotropy curves, and only the relative amplitudes of the components were allowed to vary. This yielded the fits that are shown as solid lines in figures 7.3a and b. The two time constants had values of 2.5 ± 0.1 ps and >15 ps. In figure 7.4b the relative amplitudes of the two

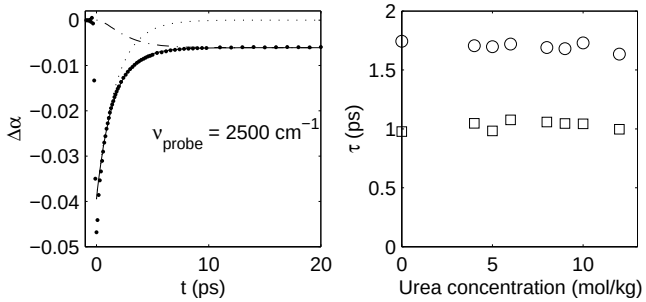

FIGURE 7.2. a) Delay scan at 2500 cm^{-1} of the transient spectrum of HDO in a 4 m solution of urea in water. The solid line is the fit to the relaxation model from chapter 5. The fit consists of two contributions: the bleaching of the OD vibration (dotted line) and the ingrowing heating signal (dashed line). b) Lifetimes the OD vibration (circles) and of the intermediate state (squares) as a function of the urea concentration.

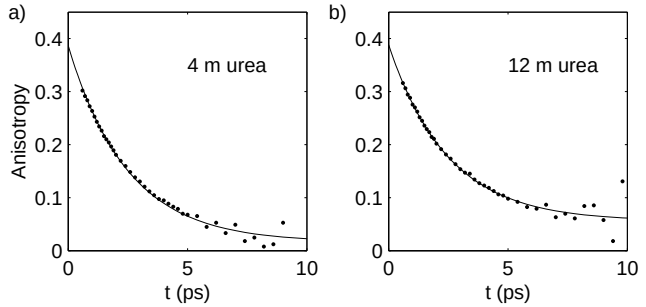

FIGURE 7.3. Anisotropy decay at the maximum of the bleach (2500 cm^{-1}) for a 4 m solution of urea in water (a) and for a 12 m solution.

components are shown. The fraction of the slow component increases linearly with urea concentration.

These results indicate that water in a urea-water mixture forms a two-component system. The majority of the water molecules reorient with a time constant of 2.5 ps, which is identical to the value that was determined for bulk water (chapter 5). Apparently these water molecules show bulk-like dynamics and are not affected by the urea molecules. A small fraction of the water molecules, however, display remarkably slower orientational dynamics and are strongly immobilized by the addition of urea. This fraction grows linearly with the urea concentration.

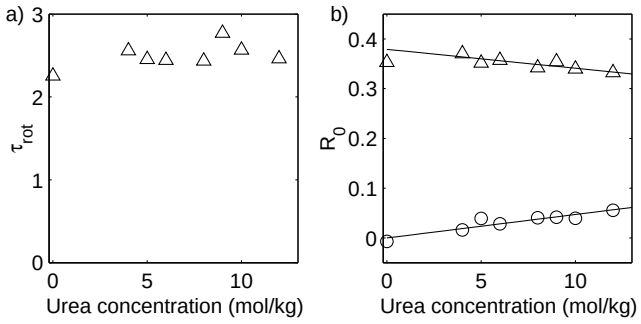

FIGURE 7.4. a) Reorientation time (fast component) as a function of urea concentration. b) Amplitudes of the slow component (circles) and the fast component (triangles) in the reorientation of HDO as a function of urea concentration. The solid lines are linear fits.

7.4 DISCUSSION

Previous work on the urea-water system has produced results that remain inconclusive as to the exact effect of urea on the orientational dynamics of water. Dielectric relaxation on 1 and 2 M solutions of urea has indicated a slight slowing down of the water dynamics [50]. However, the origin of the effect has remained unclear as the data could be reproduced by both a model that assumes a spread in the reorientation times of water and one that assumes a bimodal distribution, corresponding to bulk and solvation shell water molecules. Two molecular dynamics studies have reported reorientation times for the urea-water system. Idrissi et al. have simulated the dynamics of water at high urea mole fractions ($\sim$11 M), and they report a slowing down of the reorientation of water by an order of magnitude [46]. Astrand et al., on the other hand, have simulated 2-M solutions, and they have found a slight decrease in the reorientation rate of only the solvation shell water molecules [4]. Finally NMR experiments reveal no significant effect of urea on the orientational dynamics of water up to concentrations of 10 M [92].

Here we have used HDO as a fast and local probe of the water dynamics, and we find unambiguous proof for the existence of two types of water molecules: bulk-like water molecules and strongly immobilized water molecules. The fact that the majority of the water molecules are unaffected by the presence of urea, even at a concentration of 12 m ($\sim$8 M), is surprising. At such a high concentration all water molecules are essentially part of the solvation shell of a urea molecule, which consists of 5 to 7 water molecules, as is known from molecular dynamics simulations [51]. Given the fact that this number is higher than the average number of water molecules available per urea molecule (4-5), some water molecules may even be part of two solvation shells. The structure of the hydrogen-bond network of a 12 m solution will roughly consist of water molecules that are hydrogen-bonded to one urea molecule and three water

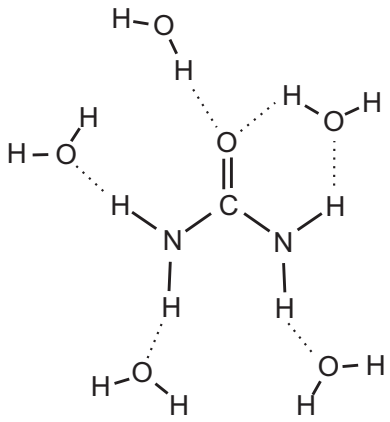

FIGURE 7.5. Possible solvation structure of the urea molecule that could explain the experimental results. One of the water molecules in the solvation shell shares two hydrogen bonds with urea.

molecules. A priori one would expect this to result in a severe distortion of the tetrahedral structure of bulk water. The reorientation time of 2.5 ps, however, indicates that the water structure around urea is, in essence, undistorted. A possible explanation for this can be found in the way urea fits in the hydrogen-bond network of liquid water [93]. Urea has the right size to substitute for a water dimer in the hydrogen-bond network. Apparently, urea can reform the six hydrogen bonds that existed between the water dimer and the neighboring water molecules, so that no significant network rearrangements are needed to solvate urea.

Our pump-probe measurements provide strong evidence that a small fraction of the water molecules are strongly immobilized by urea. From the mole fractions of urea and water we estimate that about one water hydroxyl group per urea molecule is immobilized ($\tau_{\mathrm{rot}} > 15$ ps). It is likely that these molecules are strongly associated with urea and form specific urea-water complexes. Quantum chemical calculations demonstrate that a water molecule has exactly the right size to engage in two simultaneous hydrogen bonds with urea: one hydrogen bond is donated to the carbonyl oxygen of urea and another hydrogen bond is accepted from the cis-hydrogen [63]. Such a doubly hydrogen-bonded water molecule is expected to reside in the hydration shell of urea for a relatively long time, and is thus likely to cause the slow component observed in the anisotropy. As an illustration figure 7.5 shows a possible solvation structure of urea, which would explain the experimental results.

Finally, we would like to discuss the possible role of urea in protein denaturation. The explanations for protein denaturation that are found in the literature follow two distinct viewpoints, which can be traced back to two models from the 1960s. The first viewpoint assumes that urea acts on a protein indirectly, by modifying the hydrogen-bond structure of water and thus per-

turbing water-mediated hydrophobic interactions [32]. The second viewpoint is based on a direct mechanism in which urea cooperates with water in the solvation of amino-acid residues [52, 89, 90, 100]. In this picture urea can either solvate the hydrophobic amino-acid residues or bind to the protein backbone. As our experiments show that urea has a negligible effect on the hydrogen-bond structure of water, we can rule out the first (i.e. the indirect) mechanism as an explanation for protein denaturation by aqueous urea, and we are left with the hypothesis that urea is effective in solvating the amino-acid residues of a protein.

7.5 CONCLUSIONS

We have presented measurements of the orientational dynamics of water molecules in mixtures of water and urea. We observed that even high concentrations of urea do not alter the reorientation time of the majority of the water molecules. From this we conclude that urea does not change the strength of the hydrogen-bond interactions between water molecules. A small fraction of the water molecules is, however, strongly immobilized by urea. A likely explanation is that these water molecules are engaged in specific urea-water complexes, in which two hydrogen bonds are shared by water and urea.

Bibliography

[1] K. Ando and J. T. Hynes. Molecular mechanism of HCl acid ionization in water: Ab initio potential energy surfaces and monte carlo simulations. *J. Phys. Chem. B*, 101:10464–10478, 1997.

[2] K. Ando and J. T. Hynes. Molecular mechanism of HF acid ionization in water: An electronic structure-monte carlo study. *J. Phys. Chem. A*, 103:10398–10408, 1999.

[3] J. B. Asbury, T. Steinel, K. Kwak, S. A. Corcelli, C. P. Lawrence, J. L. Skinner, and M. D. Fayer. Dynamics of water probed with vibrational echo correlation spectroscopy. *J. Chem. Phys.*, 121:12431–12446, 2004.

[4] P. O. Astrand, A. Wallqvist, and G. Karlstrom. Molecular dynamics simulations of 2 m aqueous urea solutions. *J. Phys. Chem.*, 98:8224–8233, 1994.

[5] M. V. Athawale, J. S. Dordick, and S. Garde. Osmolyte trimethylamine-N-oxide does not affect the strength of hydrophobic interactions: Origin of osmolyte compatibility. *Biophysical Journal*, 89:858–866, 2005.

[6] P. W. Atkins. *Physical Chemistry*. Oxford University Press, Oxford, 1994.

[7] B. Bagchi. Water dynamics in the hydration layer around proteins and micelles. *Chem. Rev.*, 105:3197–3219, 2005.

[8] G. Barone, E. Rizzo, and V. Vitigliano. Opposite effect of urea and some of its derivatives on water structure. *J. Phys. Chem.*, 74:2230–2232, 1970.

[9] D. V. Beauregard and R. E. Barret. Ultrasonics and water structure in urea solutions. *J. Chem. Phys.*, 49:5241–5244, 1968.

[10] B. J. Bennion and V. Daggett. Counteraction of urea-induced protein denaturation by trimethylamine N-oxide: A chemical chaperone at atomic resolution. *Proc. Natl. Acad. Sci. U.S.A*, 101:6433–6438, 2004.

[11] B. J. Berne and R. Pecora. *Dynamic Light Scattering, With Applications to Chemistry, Biology and Physics*. Dover Publications, Mineola, 2000.

[12] M. Bonn, M. J. P. Brugmans, A. W. Kleyn, and R. A. Van Santen. Fast energy delocalization upon vibrational relaxation of a deuterated zeolite surface hydroxyl. *J. Chem. Phys.*, 102:2181–2186, 1995.

[13] Robert W. Boyd. *Nonlinear Optics*. Elsevier, 2003.

[14] B. H. Bransden and C. J. Joachain. *Introduction to Quantum Mechanics*. Addison Wesley Longman Limited, 1989.

[15] P. Buchanan, N. Aldiwan, A. K. Soper, J. L. Creek, and C. A. Koh. Decreased structure on dissolving methane in water. *Chem. Phys. Lett.*, 415:89–93, 2005.

[16] P. N. Butcher and D. Cotter. *The Elements of Nonlinear Optics*. Cambridge University Press, 1990.

[17] B. J. C. Cabral, R. G. B. Fonseca, and J. A. M. Simões. Density-functional and density-functional reaction field calculations of the molecular properties of phenol. *Chem. Phys. Lett.*, 258:436–444, 1996.

[18] D. Chandler. Interfaces and the driving force of hydrophobic assembly. *Nature*, 437:640–647, 2005.

[19] E.S. Courtenay, M. W. Capp, C. F. Anderson, and M. T. Record. Vapor pressure osmometry studies of osmolyte-protein interactions: Implications for the action of osmoprotectants in vivo and for the interpretation of "osmotic stress" experiments in vitro. *Biochemistry*, 39:4455–4471, 2000.

[20] M. L. Cowan, B. D. Bruner, N. Huse, J. R. Dwyer, B Chugh, E. T. J. Nibbering, T. Elsaesser, and R. J. D. Miller. Ultrafast memory loss and energy redistribution in the hydrogen bond network of liquid H2O. *Nature*, 434:199–202, 2005.

[21] D. Cringus, S. Yeremenko, M. S. Pshenichnikov, and D. A. Wiersma. Hydrogen bonding and vibrational energy relaxation in water-acetonitrile mixtures. *J. Phys. Chem. B*, 108(29):10376–10387, 2004.

[22] J. C. Deak, S. T. Rhea, L. K. Iwaki, and D. D. Dlott. Vibrational energy relaxation and spectral diffusion in water and deuterated water. *J. Phys. Chem. A*, 104:4866–4875, 2000.

[23] S. Dixit, J. Crain, W. C. K. Poon, J. L. Finney, and A. K. Soper. Molecular segregation observed in a concentrated alcohol-water solution. *Nature*, 416:829–832, 2002.

[24] J. D. Eaves, J. J. Loparo, C. J. Fecko, S. T. Roberts, A. Tokmakoff, and P. L. Geissler. Hydrogen bonds in liquid water are broken only fleetingly. *Proc. Natl. Acad. Sci. U.S.A*, 102:13019–13022, 2005.

[25] D. Eisenberg and W. Kauzmann. *The Structure and Properties of Water*. Oxford University Press, New York, 1969.

[26] T. Elsaesser and H. J. Bakker (Eds.). *Ultrafast Hydrogen Bonding Dynamics and Proton Transfer Processes in the Condensed Phase*. Kluwer, Dordrecht, 2002.

[27] C. J. Fecko, J. D. Eaves, J. J. Loparo, A. Tokmakoff, and P. L. Geissler. Ultrafast hydrogen-bond dynamics in the infrared spectroscopy of water. *Science*, 301:1698–1701, 2003.

[28] E. G. Finer, F. Franks, and M. J. Tait. Nuclear magnetic resonance studies of aqueous urea solutions. *J. Am. Chem. Soc.*, 94:4424–4429, 1972.

[29] T. Förster. Transfer mechanisms of electronic excitation. *Discuss. Faraday Soc.*, 27:7–17, 1959.

[30] Grant R. Fowles. *Introduction to Modern Optics*. Dover Publications, 1975.

[31] H. S. Frank and M. W. Evans. Free volume and entropy in condensed systems III. entropy in binary liquid mixtures; partial molal entropy in dilute solutions; structure and thermodynamics in aqueous electrolytes. *J. Chem. Phys.*, 13:507–532, 1945.

[32] H. S. Frank and F. Franks. Structural approach to the solvent power of water for hydrocarbons; urea as a structure breaker. *J. Chem. Phys.*, 48:4746–4757, 1968.

[33] K. J. Gaffney, P. H. Davis, I. R. Piletic, N. E. Levinger, and M. A. Fayer. Hydrogen bond dissociation and reformation in methanol oligomers following hydroxyl stretch relaxation. *J. Phys. Chem. A*, 106:12012–12023, 2002.

[34] G. M. Gale, G. Gallot, F. Hache, N. Lascoux, S. Bratos, and J-Cl. Leicknam. Femtosecond dynamics of hydrogen bonds in liquid water: A real time study. *Phys. Rev. Lett.*, 82:1068–1071, 1999.

[35] K. R. Gallagher and K. A. Sharp. A new angle on heat capacity changes in hydrophobic solvation. *J. Am. Chem. Soc.*, 125:9853–9860, 2003.

[36] G. Gallot, S. Bratos, S. Pommeret, N. Lascoux, J. C. Leicknam, M. Kozinski, W. Amir, and G. M. Gale. Coupling between molecular rotations and OH $\cdots$ O motions in liquid water: Theory and experiment. *J. Chem. Phys.*, 117(24):11301–11309, 2002.

[37] B. C. Godralla and M. D. Zeidler. Molecular dynamics in the system water-dimethylsulphoxide a n.m.r. relaxation study. *Mol. Phys.*, 59:817–828, 1986.

[38] W. T. Grubbs, T. P. Dougherty, and E. J. Heilweil. Vibrational energy dynamics of hydrogen-bonded pyrrole complexes. *J. Phys. Chem.*, 99:10716–10722, 1995.

[39] E. H. Hardy, A. Zygar, M. D. Zeidler, M. Holz, and F. D. Sacher. Isotope effect on the translational and rotational motion in liquid water and ammonia. *J. Chem. Phys.*, 114:3174–3181, 2001.

[40] R. Haselmaier, M. Holz, W. Marbach, and H. Weingartner. Water dynamics near a dissolved noble gas. first direct experimental evidence for a retardation effect. *J. Phys. Chem.*, 99:2243–2246, 1995.

[41] G. Herzberg. *Molecular Spectra and Molecular Structure, II Infrared and Raman Spectra of Polyatomic Molecules*. Lancaster Press, Lancaster, 1945.

[42] G. Hummer, S. Garde, A. E. Garcia, A. Pohorille, and L. R. Pratt. An information theory model of hydrophobic interactions. *Proc. Natl. Acad. Sci. U.S.A*, 93:8951–8955, 1996.

[43] N. Huse, K. Heyne, J. Dreyer, E. T. J. Nibbering, and T. Elsaesser. Vibrational mulitlevel quantum coherence due to anharmonic couplings in intermolecular hydrogen bonds. *Phys. Rev. Lett.*, 91:197401, 2003.

[44] A. Idrissi. Molecular structure and dynamics of liquids: Aqueous urea solutions. *Spectrochimica Acta Part A*, 61:1–17, 2005.

[45] A. Idrissi, P. Bartolini, M. Ricci, and R. Righini. Time resolved optical kerr effect analysis of urea-water system. *J. Chem. Phys.*, 114:6774–6780, 2001.

[46] A. Idrissi, F. Sokolic, and A. Perera. A molecular dynamics study of the urea/water mixture. *J. Chem. Phys.*, 112:9479–9488, 2000.

[47] T. Ishida, P. J. Rossky, and E. W. Castner. A theoretical investigation of the shape and hydration properties of aqueous urea: Evidence for nonplanar urea geometry. *J. Phys. Chem. B*, 108:17583–17590, 2004.

[48] Y. Ishihara, S. Okouchi, and H. Uedaira. Dynamics of hydration of alcohols and diols in aqueous solutions. *J. Chem. Soc., Faraday Trans.*, 93:3337–3342, 1997.

[49] S. Ishiuchi, M. Fujii, T. W. Robinson, B. J. Miller, and H. G. Kjaergaard. Vibrational overtone spectroscopy of phenol and its deuterated isotopomers. *J. Phys. Chem. A*, 110:7345–7354, 2006.

[50] U. Kaatze, H. Gerke, and R. Pottel. Dielectric relaxation in aqueous solutions of urea and some of its derivatives. *J. Phys. Chem.*, 90:5464–5469, 1986.

[51] B. Kallies. Coupling of solvent and solute dynamics - molecular dynamics simulations of aqueous urea solutions with different intramolecular potentials. *Phys. Chem. Chem. Phys.*, 4:86–95, 2002.

[52] G. C. Kreschek and H. A. Scheraga. *J. Phys. Chem.*, 69:1704–1706, 1965.

[53] M. F. Kropman, H.-K. Nienhuys, and H. J. Bakker. Real-time measurement of the orientational dynamics of aqueous solvation shells in bulk liquid water. *Phys. Rev. Lett.*, 88:077601, 2002.

[54] R. Kubo, M. Toda, and N. Hashitsume. *Statistical Thermodynamics II, Nonequilibrium Statistical Mechanics*. Springer-Verlag, 1992.

[55] D. Laage and J. T. Hynes. Do more strongly hydrogen-bonded water molecules reorient more slowly? *Chem. Phys. Lett.*, 433:80–85, 2006.

[56] D. Laage and J. T. Hynes. A molecular jump mechanism of water reorientation. *Science*, 311:832–835, 2006.

[57] R. Laenen, C. Rauscher, and A. Lauberau. Dynamics of local substructures in water observed by ultrafast infrared hole burning. *Phys. Rev. Lett.*, 80:2622–2625, 1998.

[58] J. R. Lakowicz. *Principles of Fluorescence Spectroscopy*. Kluwer Academic, New York, 2000.

[59] C. P. Lawrence and J. L. Skinner. Vibrational spectroscopy of HOD in liquid D_2O. II. infrared line shapes and vibrational stokes shift. *J. Chem. Phys.*, 117:8847–8854, 2002.

[60] C. P. Lawrence and J. L. Skinner. Vibrational spectroscopy of HOD in liquid D_2O. III. spectral diffusion, and hydrogen-bonding and rotational dynamics. *J. Chem. Phys.*, 118(1):264–272, 2003.

[61] C. P. Lawrence and J. L. Skinner. Vibrational spectroscopy of HOD in liquid D_2O. VI. intramolecular and intermolecular vibrational energy flow. *J. Chem. Phys.*, 119:1623–1633, 2003.

[62] B. Lee and G. Graziano. A two-state model of hydrophobic hydration that produces compensating enthalpy and entropy changes. *J. Am. Chem. Soc.*, 118:5163–5168, 1996.

[63] C. Lee, E. A. Stahlberg, and G. Fitzgerald. Chemical structure of urea in water. *J. Phys. Chem.*, 99:17737–17741, 1995.

[64] A. L. Lehninger, D. L. Nelson, and M. M. Cox. *Principles of Biochemistry*. Worth Publishers Inc., 1993.

[65] U. Liddel and E. D. Becker. Infra-red spectroscopic studies of hydrogen bonding in methanol, ethanol, and t-butanol. *Spectrochimica Acta*, 10:70–84, 1957.

[66] M. Lim and R. M. Hochstrasser. Unusual vibrational dynamics of the acetic acid dimer. *J. Chem. Phys.*, 115:7629–7643, 2001.

[67] T. Y. Lin and S. N. Timasheff. Why do some organisms use a urea-methylamine mixture as osmolyte - thermodynamic compensation of urea and trimethylamine N-oxide interactions with protein. *Biochemistry*, 33:12695–12701, 1994.

[68] J. Lindner, P. Vohringer, M. S. Pshenichnikov, D. Cringus, D. A. Wiersma, and M. Mostovoy. Vibrational relaxation of pure liquid water. *Chem. Phys. Lett.*, 421:329–333, 2006.

[69] A. J. Lock and H. J. Bakker. Temperature dependence of vibrational relaxation in liquid H_2O. *J. Chem. Phys.*, 117(4):1708–1713, 2002.

[70] J. J. Loparo, C. J. Fecko, J. D. Eaves, S. T. Roberts, and A. Tokmakoff. Reorientational and configurational fluctuations in water observed on molecular length scales. *Phys. Rev. B*, 70:180201, 2004.

[71] W. Mikenda. Stretching frequency versus bond distance correlation of O-D(H)...Y (Y = N, O, S, Se, Cl, Br, I) hydrogen bonds in solid hydrates. *J. Mol. Struct.*, 147:1–15, 1986.

[72] K. B. Moller, R. Rey, and J. T. Hynes. Hydrogen bond dynamics in water and ultrafast infrared spectroscopy: A theoretical study. *J. Phys. Chem. A*, 108:1275–1289, 2004.

[73] J. Morgan and B. E. Warren. X-ray analysis of the structure of water. *J. Chem. Phys.*, 6:666–673, 1938.

[74] Shaul Mukamel. *Principles of Nonlinear Optical Spectroscopy.* Oxford University Press, 1995.

[75] K. P. Murphy, P. L. Privalov, and S. J. Gill. Common features of protein unfolding and dissolution of hydrophobic compounds. *Science*, 247:559–561, 1990.

[76] E. T. J. Nibbering and T. Elsaesser. Ultrafast vibrational dynamics of hydrogen bonds in the condensed phase. *Chem. Rev.*, 104:1887–1914, 2004.

[77] H.-K. Nienhuys, R. A. Van Santen, and H. J. Bakker. Orientational relaxation of liquid water molecules as an activated process. *J. Chem. Phys.*, 112:8487–8494, 2000.

[78] A. Novak. Hydrogen bonding in solids. correlation of spectroscopic and crystallographic data. *Struct. Bond.*, 18:177–216, 1974.

[79] S. K. Pal and A. H. Zewail. Dynamics of water in biological recognition. *Chem. Rev.*, 104:2099–2123, 2004.

[80] V. A. Parsegian, R. P. Rand, and D. C. Rau. Osmotic stress, crowding, preferential hydration, and binding: A comparison of perspectives. *Proc. Natl. Acad. Sci. U.S.A*, 97:3987–3992, 2000.

[81] G. C. Pimentel and A. L. McClellan. *The Hydrogen Bond.* Freeman, San Fransisco, 1960.

[82] R. Rey and J. T. Hynes. Vibrational energy relaxation of HOD in liquid D_2O. *J. Chem. Phys.*, 104:2356–2368, 1996.

[83] R. Rey, K. B. Moller, and J. T. Hynes. Hydrogen bond dynamics in water and ultrafast infrared spectroscopy. *J. Phys. Chem. A*, 106:11993–11996, 2002.

[84] R. Rey, K. B. Moller, and J. T. Hynes. Ultrafast vibrational population dynamics of water and related systems: A theoretical perspective. *Chem. Rev.*, 104:1915–1928, 2004.

[85] Y. L. A. Rezus and H. J. Bakker. On the orientational relaxation of HDO in liquid water. *J. Chem. Phys.*, 123:114502, 2005.

[86] G. D. Rose, P. J. Fleming, J. R. Banavar, and A. Maritan. A backbone-based theory of protein folding. *Proc. Natl. Acad. Sci. U.S.A*, 103:16623–16633, 2006.

[87] J. A. Schellman. Protein stability in mixed solvents: A balance of contact interaction and excluded volume. *Biophysical Journal*, 85:108–125, 2003.

[88] F. Sciortino, A. Geiger, and H. E. Stanley. Effect of defects on molecular mobility in liquid water. *Nature*, 354:218–221, 1991.

[89] K. A. Sharp, B. Madan, E. Manas, and J.M. Vanderkooi. Water structure changes induced by hydrophobic and polar solutes revealed by simulations and infrared spectroscopy. *J. Chem. Phys.*, 114:1791–1796, 2001.

[90] J. A. Shellman. *C. R. Trav. Lab Carlsberg*, 29:223–229, 1955.

[91] Y. R. Shen. *The Principles of Nonlinear Optics*. John Wiley & Sons, Inc., 1984.

[92] A. Shimizu, K. Fumino, K. Yukiyasu, and Y. Taniguchi. NMR studies on dynamic behavior of water molecule in aqueous denaturant solutions at 25 degrees C: Effects of guanidine hydrochloride, urea and alkylated ureas. *J. Mol. Liq.*, 85:269–278, 2000.

[93] A. K. Soper, E. W. Castner, and A. Luzar. Impact of urea on water structure: A clue to its properties as a denaturant? *Biophysical Chemistry*, 105:649–666, 2003.

[94] A. K. Soper and J. L. Finney. Hydration of methanol in aqueous solution. *Phys. Rev. Lett.*, 71:4346–4349, 1993.

[95] N. T. Southall, K. A. Dill, and A. D. J. Haymet. A view of the hydrophobic effect. *J. Phys. Chem. B*, 106:521–533, 2002.

[96] T. Steinel, J. B. Asbury, J. Zheng, and M. D. Fayer. Watching hydrogen bonds break: A transient absorption study of water. *J. Phys. Chem. A*, 108:10957 –10964, 2004.

[97] J. Stenger, D. Madsen, P. Hamm, E. T. J. Nibbering, and T. Elsaesser. Ultrafast vibrational dephasing of liquid water. *Phys. Rev. Lett.*, 87:027401, 2001.

[98] J. Stenger, D. Madsen, P. Hamm, E. T. J. Nibbering, and T. Elsaesser. A photon echo peak shift study of liquid water. *J. Phys. Chem. A*, 106:2341–2350, 2002.

[99] F. H. Stillinger. Structure in aqueous solutions of nonpolar solutes from the standpoint of scaled-particle theory. *J. Solution Chem.*, 2:141–158, 1973.

[100] R. H. Stokes. *Aust. J. Chem.*, 20:2087–2100, 1967.

[101] T. O. Street, D. W. Bolen, and G. D. Rose. A molecular mechanism for osmolyte-induced protein stability. *Proc. Natl. Acad. Sci. U.S.A*, 103:13997–14002, 2006.

[102] L. Stryer. *Biochemistry.* W. H. Freeman and Co., New York, 1988.

[103] S. N. Timasheff. Protein-solvent preferential interactions, protein hydration, and the modulation of biochemical reactions by solvent components. *Proc. Natl. Acad. Sci. U.S.A*, 99:9721–9726, 2002.

[104] A. Tokmakoff. Introductory quantum mechanics II.
http://ocw.mit.edu/OcwWeb/Chemistry/, Spring 2005.

[105] J. Turner and A. K. Soper. The effect of apolar solutes on water structure: Alcohols and tetraalkylammonium ions. *J. Chem. Phys.*, 101:6116–6125, 1994.

[106] S. Vaitheeswaran, H. Yin, J. C. Rasaiah, and G. Hummer. Water clusters in nonpolar cavities. *Proc. Natl. Acad. Sci. U.S.A*, 101:17002–17005, 2004.

[107] F. Vanzi, B. Madan, and K. Sharp. Effect of the protein denaturants urea and guanidinium on water structure: A structural and thermodynamic study. *J. Am. Chem. Soc.*, 120:10748–10753, 1998.

[108] W. Wachter, R. Buchner, and G. Hefter. Hydration of tetraphenylphosphonium and tetraphenylborate ions by dielectric relaxation spectroscopy. *J. Phys. Chem. B*, 110:5147–5154, 2006.

[109] G. E. Walrafen. Raman spectral studies of the effects of urea and sucrose on water structure. *J. Chem. Phys.*, 44:3726–3727, 1966.

[110] A. J. Wang and D. W. Bolen. A naturally occurring protective system in urea-rich cells: Mechanism of osmolyte protection of proteins against urea denaturation. *Biochemistry*, 36:9101–9108, 1997.

[111] B. Widom, P. Bhimalapuram, and K. Koga. The hydrophobic effect. *Phys. Chem. Chem. Phys.*, 5:3085–3093, 2003.

[112] S. Woutersen and H. J. Bakker. Resonant intermolecular transfer of vibrational energy in liquid water. *Nature*, 402:507–509, 1999.

[113] S. Woutersen, U. Emmerichs, and H. J. Bakker. Femtosecond mid-IR pump-probe spectroscopy of liquid water: Evidence for a two-component structure. *Science*, 278:658–660, 1997.

[114] P. H. Yancey, M. E. Clark, S. C. Hand, R. D. Bowlus, and G. N. Somero. Living with water stress: Evolution of osmolyte systems. *Science*, 217:1214–1222, 1982.

[115] Amnon Yariv and Pochi Yeh. *Optical Waves in Crystals*. John Wiley & Sons, 1984.

[116] Q. Zou, B. J. Bennion, V. Daggett, and K. P. Murphy. The molecular mechanism of stabilization of proteins by TMAO and its ability to counteract the effects of urea. *J. Am. Chem. Soc.*, 124:1192–1202, 2002.

[117] Q. Zou, S. M. Habermann-Rottinghaus, and K. P. Murphy. Urea effects on protein stability: Hydrogen bonding and the hydrophobic effect. *Proteins: Structure, Function and Genetics*, 31:107–115, 1998.

Summary

The hydrogen bond is a structural element that is encountered everywhere in living nature: for instance, it holds together the two strands of DNA; it is responsible for the formation of α-helices and β-sheets in proteins; and, it leads to the strong attraction between water molecules in the liquid phase. In this thesis we describe spectroscopic experiments that probe the ultrafast motion of hydrogen-bonded molecules; in most of the experiments the investigated molecules are water molecules. The experimental technique we use is polarization-resolved femtosecond mid-infrared pump-probe spectroscopy. This technique employs two ultrashort laser pulses (i.e. $\sim$100 fs): an intense pump pulse to excite the vibrations of a significant fraction of the molecules in the sample; and a weak delayed probe pulse that monitors the state of the system after excitation. By performing the experiment with a combination of different pump and probe polarizations, one can obtain information about the rotational motion of the vibrationally excited molecules.

As a first experiment we studied the dynamics of hydrogen-bonded complexes of phenol-*d* and acetone which were dissolved in chloroform. We probed the OD vibration of phenol and found its lifetime to be strongly affected by hydrogen bonding: it varies from 11 ps, for phenol molecules that are weakly hydrogen bonded to the solvent, to 1 ps, for phenol that is strongly hydrogen bonded to acetone. The hydrogen bond also affects the orientational motion of the OD group. For monomeric phenol molecules the reorientation time is 3.7 ps; when phenol is strongly hydrogen-bonded to acetone, the reorientation time increases dramatically, to >30 ps, indicating that the reorientation is severely hindered by the hydrogen bond.

Water reorientation cannot be studied in the (isotopically) pure liquid because of a number of experimental complications. The approach is therefore to monitor the orientational dynamics of partly deuterated water molecules (HDO) that are introduced at low concentration into either normal water (H_2O) or heavy water (D_2O). In the former system one probes the dynamics of the OD vibration, while in the latter system the OH vibration is probed. The vibrational relaxation of the two systems is qualitatively similar: the energy of the OH/OD-stretching vibration is first transferred to an intermediate state; the second step in the relaxation is the decay of this level, which is accompanied by the thermalization of the vibrational energy. For HDO in H_2O the lifetime of the OD vibration is 1.8 ps and that of the intermediate state is 0.9 ps. For the OH vibration the respective values are 0.7 ps and 0.6 ps. The relatively long lifetime of the OD vibration makes this vibration particularly well suited to probe the orientational dynamics of water. The reorientation time of HDO molecules in H_2O is 2.5 ps. This time constant is independent of the probe

frequency.

For HDO in heavy water (D_2O) we identified a process that can affect the measured anisotropy decay. It turns out that the relaxation of the OH vibration leads to a temporary increase in the rotational mobility of the HDO molecule. If this effect is left uncorrected, it can severely distort the measured anisotropy. To avoid any complications, we have used the OD-stretching vibration of the HDO/H_2O system for the remaining experiments, in which we investigated the effects of added solutes on the orientational dynamics of water.

Concentrated aqueous solutions of urea are potent protein denaturants; the physical mechanism underlying this process, however, has not yet been elucidated. There are essentially two viewpoints: the first states that urea modifies the structure of water, which in turn leads to protein denaturation (indirect mechanism); the second viewpoint presumes the existence of direct interactions between urea and protein functional groups. To shed light on this issue, we studied the orientational dynamics of water molecules in aqueous solutions of urea. Surprisingly, we observed that even very high concentrations of urea (up to 8 M) do not affect the reorientation time constant of the majority of the water molecules (τ_{rot}= 2.5 ps). An explanation for this observation may be that urea fits well into the hydrogen-bond network of water as it can form up to eight hydrogen bonds with water. A small part of the water molecules, however, were strongly slowed down in their orientational dynamics (τ_{rot} >10 ps). These water molecules are likely to be bound to urea by two hydrogen bonds. As for protein denaturation our results point in the direction of the direct mechanism since urea does not seem to modify the structure of water.

In a next experiment we restricted the hydrogen-bonding capabilities of urea. For this purpose a derivative of urea, tetramethylurea (TMU), was used, in which the polar NH groups are substituted by hydrophobic methyl groups. We found that, unlike urea, TMU has a dramatic effect on the orientational dynamics of the water molecules. The water molecules in a TMU solution are partitioned into two fractions. One fraction displays the same orientational dynamics as pure water (τ_{rot} = 2.5 ps). The other fraction, on the other hand, is strongly immobilized and displays much slower orientational dynamics (τ_{rot} >10 ps). This partitioning persists for mixtures that contain an excess volume fraction of TMU. The water in these mixtures is probably present as clusters, and up to 60% of all water molecules are immobilized. At low concentrations the immobilized water fraction increases linearly with the TMU concentration, showing that the immobilized water molecules are part of the TMU solvation shell. For every TMU molecule there are 15±2 immobilized water molecules. The methyl groups are the groups that cause the immobilization, as was confirmed by repeating the experiment with solutes containing a different number of methyl groups. We observed a linear scaling between the number of immobilized water OH groups and the number of methyl groups in the solute: every methyl group is responsible for the immobilization of approximately 4 water OH groups.

The immobilization of water by hydrophobic groups can be understood by considering the recently published reorientation mechanism of liquid water [56]. According to this mechanism, water reorientation proceeds through the for-

mation of bifurcated hydrogen bonds, which provide a low-energy route for reorientation. For a bifurcated hydrogen bond to form, a water molecule must, however, temporarily attain a fivefold coordination. This suggests that water immobilization in the vicinity of apolar groups results from a steric effect, in which the hydrophobic group prevents a new water molecule from approaching a tetrahedrally coordinated water molecule, thereby hampering reorientation.

The experiments described here shed new light on an old theory regarding the solvation of hydrophobic compounds by water. According to this theory from the 1940s, due to Henry Frank and Marjorie Evans, apolar chemical groups are surrounded by an ice-like layer of water molecules; this layer is named an iceberg. Our experiments provide a molecular picture of these icebergs, showing that they consist of four immobilized water OH groups per methyl group. The hydrogen-bonding structure of the immobilized water molecules, however, resembles that of liquid water; the strong hydrogen bonds encountered in real ice are absent.

Certain small organic molecules, named osmolytes, can affect the structure and stability of proteins. We found that the stabilizing osmolyte trimethylamine-N-oxide (TMAO) exhibits the unique property of speeding up the orientational dynamics of the mobile water fraction. This is probably due to the poor fitting of TMAO in the hydrogen-bond network of water. We further observed a non-additive effect of TMAO and N-methylacetamide (NMA) on the orientational dynamics of the mobile water fraction; NMA is a molecule often used as a model for the protein backbone. The observed non-additivity provides insight into the mechanism by which TMAO stabilizes the folded conformation of proteins. TMAO appears to modify the hydrogen-bonding structure of water in such a way that solvation of the protein backbone becomes energetically unfavorable, thereby providing a driving force for proteins to fold.

Samenvatting

Water en leven zijn onlosmakelijk met elkaar verbonden. De talrijke biochemische reacties die ons in leven houden voltrekken zich alleen in water: van de verbranding van glucose tot aan de replicatie van DNA. Bij deze processen is een actieve rol weggelegd voor water. Watermoleculen nemen bijvoorbeeld de energie op die vrijkomt bij chemische reacties en voeren deze efficiënt weg. Ook kunnen reactieproducten gestabiliseerd worden door specifieke wisselwerkingen met watermoleculen. Om dit soort processen beter te begrijpen is het van belang te weten hoe watermoleculen in de vloeistoffase bewegen. Deze bewegingen blijken zich onvoorstelbaar snel te voltrekken, op tijdschalen van een miljoenste van een miljoenste van een seconde. Hoe weten we dit eigenlijk? Wat voor experimentele technieken zijn nodig om dit soort snelle bewegingen te meten? En als we dan precies kunnen meten hoe snel watermoleculen draaien, welke vragen kunnen we hiermee beantwoorden? Over dit soort zaken gaat het onderzoek dat ik in dit proefschrift heb beschreven.

Scherp in beeld Het bestuderen van bewegende watermoleculen is te vergelijken met het fotograferen van een race-auto: de auto komt alleen scherp in beeld als de sluitertijd kort is. De bewegingen van watermoleculen zijn echter zo snel dat een gewone sluiter niet volstaat. Om de watermoleculen toch scherp te krijgen gebruiken we ultrakorte laserpulsen. Deze duren slechts een tiende picoseconde. Een picoseconde is een miljoenste van een miljoenste van een seconde (10^{-12} s). Tijdens de korte 'belichtingstijd' van een tiende picoseconde hebben de watermoleculen praktisch geen tijd om te bewegen.

Figuur 1 toont een schets van onze experimentele opstelling. De techniek die we gebruiken staat bekend als pomp-probe spectroscopie. Het principe achter deze techniek is eenvoudig. Er zijn twee infrarode lichtpulsen: een pomp- en een probepuls. De pomppuls brengt eerst de watermoleculen in trilling. Vervolgens kijken we met de probepuls hoe de trillingen uitdoven en de aangeslagen watermoleculen terugkeren naar hun evenwichtstoestand. Uit deze metingen is af te leiden hoe snel de watermoleculen draaien.

De relaxatie van de watermoleculen (d.w.z. het uitdoven van de trillingen) duurt enkele picoseconden. Om deze relaxatie te kunnen volgen moet het tijdsverschil tussen de pomp- en de probepuls van dezelfde orde van grootte zijn. Zo'n onvoorstelbaar kort tijdsverschil realiseren we door gebruik te maken van de lichtsnelheid. De probepuls is in feite een zwakke reflectie van de pomppuls

en kan worden vertraagd door het licht langs een omweg te sturen. Omdat de lichtsnelheid driehonderd duizend kilometer per uur bedraagt, moeten we voor een vertraging van 1 ps het probelicht 0.3 mm omleiden. De meting wordt herhaald voor een serie tijdsvertragingen tussen de pomp- en probepuls. Zo kunnen we als het ware een filmpje reconstrueren van bewegende watermoleculen. Terug naar de vergelijking met de race-auto. Je zou kunnen zeggen dat we na ieder rondje om de racebaan een foto nemen. Hierbij laten we de tijd tussen het moment dat de startlijn gepasseerd wordt en het moment dat de foto genomen wordt steeds iets toenemen. Wanneer we alle foto's achter elkaar leggen kunnen we ons een idee vormen van de beweging van de race-auto, ook al zijn de afzonderlijke foto's statische opnames.

HALFZWAAR WATER Het experiment is eigenlijk iets ingewikkelder dan hierboven werd geschetst. De samples die wij bestuderen bestaan uit water (H_2O) waaraan een paar procent zwaar water (D_2O) is toegevoegd. Hierdoor ontstaan 'halfzware' watermoleculen (HDO). Deze HDO moleculen bevatten één gewoon waterstofatoom (H) en één zwaar waterstofatoom (D). Chemisch zijn HDO moleculen identiek aan gewone watermoleculen, maar ze hebben het voordeel dat hun rotaties met ultrasnelle spectroscopie gevolgd kunnen worden.

Figuur 2a toont het infrarood absorptiespectrum van ons sample. Infrarood licht heeft de juiste frequentie om de vibraties van moleculen aan te slaan. We zien in het spectrum een aantal pieken. Deze corresponderen allemaal met welgedefinieerde vibraties van de H_2O en HDO moleculen. In ons experiment zoomen we in op de piek die specifiek is voor HDO moleculen: de resonantie bij 2500 cm^{-1}. Deze is toe te schrijven aan de vibratie van de OD groep van het HDO molecuul.

De golflengte van de pomppuls is precies afgestemd op deze resonantie. Absorptie van de pomppuls door het sample leidt er dan ook toe dat de OD vibratie aangeslagen wordt. Met de probepuls kunnen we deze vibrerende HDO moleculen detecteren. Dit is te danken aan het feit dat de aangeslagen HDO moleculen licht van een lagere frequentie absorberen (rond 2300 cm^{-1}) dan niet aangeslagen HDO moleculen (figuur 2b). Het spectrum van het geëxciteerde sample vertoont hierdoor een extra piek. De absorptieverandering die optreedt na excitatie (we noemen dit het pomp-probe signaal) is evenredig met het aantal aangeslagen HDO moleculen. Door deze absoptieverandering te meten als functie van de tijd tussen de pomp- en de probepuls kunnen we de levensduur van de OD vibratie bepalen (figuur 2c). Deze levensduur blijkt slechts 1.8 ps te bedragen.

TRILLINGSRICHTING Om tenslotte de rotatie bewegingen van de HDO moleculen te kunnen volgen moeten we nog één element toevoegen aan het experiment. Dit is de trillingsrichting, ofwel polarisatie, van de twee lichtpulsen.

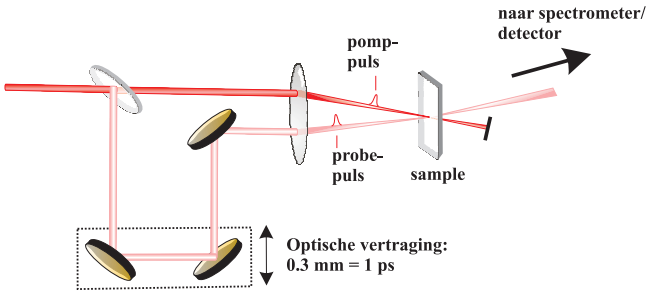

FIGUUR 1. Pomp-probe opstelling. Het licht is hier weergegeven als bundels, maar in feite is er sprake van lichtpulsen.

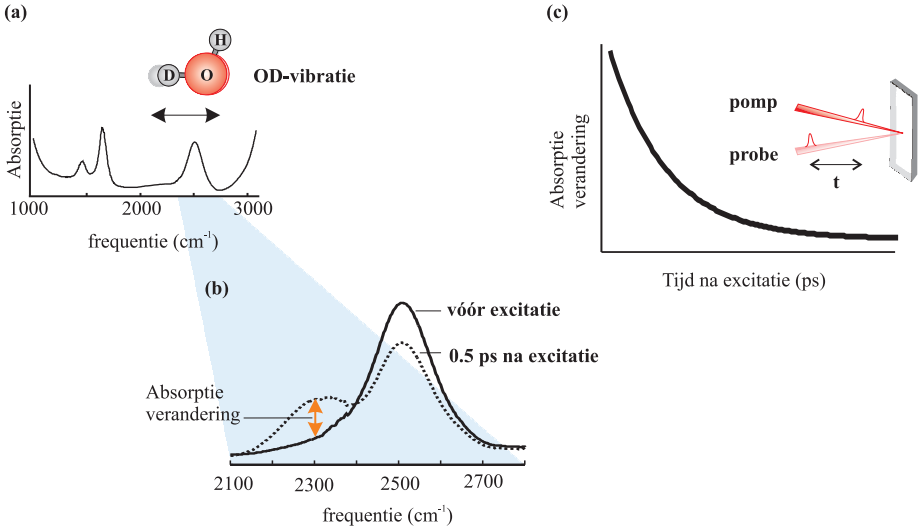

FIGUUR 2. (a) Het infrarood spectrum van HDO vertoont een resonantie bij 2500 cm^{-1} als gevolg van de vibratie van de OD-groep van het molecuul. (b) Aangeslagen HDO moleculen kunnen we waarnemen in het spectrum doordat deze moleculen een lagere resonantiefrequentie hebben dan moleculen in de niet aangeslagen toestand. (c) Door de absorptieverandering bij 2300 cm^{-1} te meten als functie van de tijd tussen de twee pulsen kunnen we de levensduur van de OD-vibratie bepalen.

De grootte van het pomp-probe signaal hangt namelijk af van de relatieve polarisaties van de pomp- en probepuls. Juist uit deze afhankelijkheid kunnen we afleiden hoe snel HDO moleculen bewegen. Het mechanisme dat hierachter schuilgaat wordt uitgelegd in figuur 3. De kans om een OD groep aan te slaan is het grootst als deze in de richting van de pomppolarisatie ligt; OD groepen die loodrecht op deze richting staan kunnen niet worden aangeslagen. Het gevolg hiervan is dat de populatie van aangeslagen OD groepen een voorkeursrichting heeft. Deze OD groepen wijzen min of meer in de richting van de pomppolarisatie (figuur 3a). Voor de absorptie van het probelicht door *aangeslagen* HDO moleculen geldt eenzelfde principe: de sterkste absorptie van probelicht treedt op wanneer de probe gepolariseerd is in de richting waarlangs de meeste aangeslagen OD groepen liggen. Het resultaat hiervan is dat het pomp-probe signaal op zijn sterkst is als de pomp- en probepuls parallel gepolariseerd zijn, terwijl het op zijn zwakst is wanneer de polarisaties onderling loodrecht zijn (figuur 3b).

De aangeslagen HDO moleculen bewegen echter en verliezen zo geleidelijk hun voorkeursrichting. Hierdoor gaan de twee signalen in figuur 3b steeds meer op elkaar lijken wanneer de tijd tussen de pomp- en de probepuls toeneemt. De snelheid waarmee dit gebeurt is afhankelijk van de karakteristieke bewegingstijd (reoriëntatietijd) van de HDO moleculen. Dit biedt ons een manier om deze reoriëntatietijd bepalen. We voeren het experiment namelijk tweemaal uit, éénmaal met parallelle en éénmaal met loodrechte pomp- en probepolarisaties. Daarbij kijken we naar het (relatieve) verschil tussen de twee metingen. Dit is de anisotropie en de snelheid waarmee deze grootheid vervalt vertelt ons hoe snel HDO moleculen roteren. De vervalsconstante van de anisotropie geeft rechtstreeks de reoriëntatietijd van de HDO moleculen. Met deze methode hebben we kunnen bepalen dat watermoleculen (eigenlijk zijn dit HDO moleculen) een reoriëntatietijd hebben van 2.5 ps.

IJSBERGEN De hierboven beschreven experimentele techniek heeft centraal gestaan tijdens mijn promotie. Om je een indruk te geven van de toepasbaarheid van deze techniek, beschrijf ik hieronder één van de onderzoeken die ik heb uitgevoerd. Dat onderzoek gaat over water en olie. Iedereen weet dat water en olie niet mengen. Wat minder bekend is, is dat dit verschijnsel ten grondslag ligt aan tal van biologische processen, waaronder de vorming van celmembranen, het vouwen van eiwitten en de werking van bepaalde medicijnen. Bij al deze processen speelt de wisselwerking tussen water en olieachtige moleculen (ook wel hydrofobe of apolaire moleculen genaamd) een belangrijke rol. Een essentiële vraag hierbij is hoe watermoleculen zich gedragen in de buurt van een hydrofoob molecuul.

Er bestaat al zo'n zestig jaar onenigheid over de structuur van water rond opgeloste apolaire moleculen. Een inmiddels beroemde theorie uit de jaren veertig van de vorige eeuw van de Amerikaanse onderzoekers Henry Frank en Marjorie Evans stelt dat apolaire moleculen omringd worden door een ijsachtige

laag van watermoleculen. Frank en Evans gaven de ijsachtige laag de tot de verbeelding sprekende naam 'ijsberg'. Echter, experimenten zoals infrarood spectroscopie en neutronendiffractie laten een volstrekt ander beeld zien. Volgens deze experimenten merkt het water namelijk helemaal niets van een hydrofoob molecuul: de structuur valt niet te onderscheiden van die van zuiver water en lijkt al helemaal niet op die van ijs!

IMMOBIEL WATER Wat is er nu echt aan de hand met de watermoleculen rondom opgeloste apolaire moleculen? Om dit uit te zoeken hebben we de reoriëntatie van watermoleculen in dit soort oplossingen bestudeerd. Het idee hierachter is dat, indien hydrofobe ijsbergen werkelijk bestaan, dit van invloed moet zijn op de beweeglijkheid van de watermoleculen. Immers, in gewoon water kunnen watermoleculen heel snel bewegen terwijl ze in ijs vrijwel stilstaan.

Voor het experiment hebben we samples gebruikt bestaande uit water (met HDO!) waarin stoffen met een gedeeltelijk hydrofoob karakter waren opgelost. De structuurformules van de gebruikte moleculen zijn weergegeven in figuur 4a. Deze vier moleculen bevatten naast hydrofobe methylgroepen (CH_3-groepen) ook hydrofiele, d.w.z. waterminnende groepen, omdat ze anders nauwelijks in water zouden oplossen. Dit soort moleculen met zowel hydrofobe als hydrofiele groepen worden amfifiel genoemd.

De reoriëntatie van de watermoleculen in deze oplossingen hebben we bepaald volgens de methode die hierboven voor puur water werd beschreven. Uit de metingen volgt dat er twee soorten watermoleculen in de oplossingen voorkomen (figuur 4b): watermoleculen die snel reoriënteren – de reoriëntatietijd is gelijk aan de waarde in zuiver water (2.5 ps) – en 'immobiele' watermoleculen, die veel trager reoriënteren (reoriëntatietijd langer dan 10 ps). De aanwezigheid van traag bewegende watermoleculen doet denken aan de hierboven genoemde ijsbergen.

We blijven nu nog met één vraag: is de waargenomen immobilisatie werkelijk het gevolg van de hydrofobe groepen? Of zouden de hydrofiele groepen ook een rol spelen? Om deze vraag te beantwoorden hebben we voor elk van de stoffen uit figuur 4a het aantal watermoleculen bepaald dat per amfifiel molecuul geïmmobiliseerd wordt. Dit aantal blijkt precies te schalen met het aantal methylgroepen in het amfifiele molecuul (figuur 4c)! Dit bewijst dat de immobilisatie van de watermoleculen echt het gevolg is van de hydrofobe groepen. Het bijzondere aan onze techniek is dat we het precieze aantal geïmmobiliseerde watermoleculen kunnen bepalen: rondom iedere methylgroep bevinden zich ongeveer twee immobiele watermoleculen.

OPEN STRUCTUUR Onze experimenten laten zien dat apolaire moleculen omringd worden door een aantal langzaam bewegende watermoleculen. Je zou kunnen zeggen dat dit de ijsachtige laag is die voorspeld werd door Frank en Evans. Maar hoe zit het met al die andere experimenten, die zeggen dat de structuur van het omringende water helemaal niet ijsachtig is? De sleutel blijkt

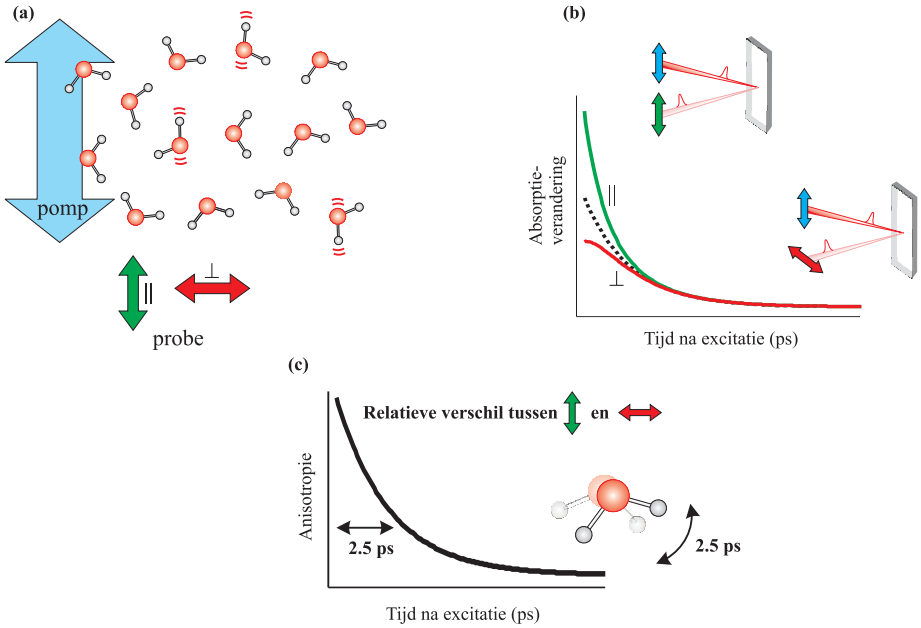

FIGUUR 3. (a) De pomp puls slaat voornamelijk HDO moleculen aan waarvan de OD groep in de richting van de pomp polarisatie ligt (blauwe pijl). (b) Hierdoor is het signaal bij parallelle polarisaties (groene lijn) aanvankelijk groter dan bij loodrechte polarisaties van de pulsen (rode lijn). (c) De anisotropie is het relatieve verschil tussen de twee signalen. Het verval van deze grootheid komt door de rotatie van de watermoleculen.

te liggen in de bijzondere structuur van vloeibaar water. Water is namelijk geen normale vloeistof waarin de moleculen dicht op elkaar gepakt zitten, maar bestaat uit een open netwerk van watermoleculen, bij elkaar gehouden door waterstofbruggen. Dit netwerk bevat relatief veel holtes. Opgeloste hydrofobe moleculen gaan bij voorkeur in deze holtes zitten. Hierbij verstoren ze de structuur van waterstofbruggen van het water niet. Wel hebben watermoleculen in de buurt van zo'n opgevulde holte minder ruimte om te draaien, wat de langzame reoriëntatie van deze watermoleculen verklaart. Het gaat dus uiteindelijk allemaal om het verschil tussen structuur en dynamica: hydrofobe ijsbergen hebben de trage dynamica van ijs maar de waterstofbrugstructuur van vloeibaar water.

CONCLUSIE Ik heb hier een korte schets proberen te geven van het onderzoek waar dit proefschrift over gaat. De experimenten over water en olie vormen hier een belangrijk deel van. De resultaten van deze experimenten zijn niet alleen vanuit fysisch oogpunt interessant. De afstoting die heerst tussen water

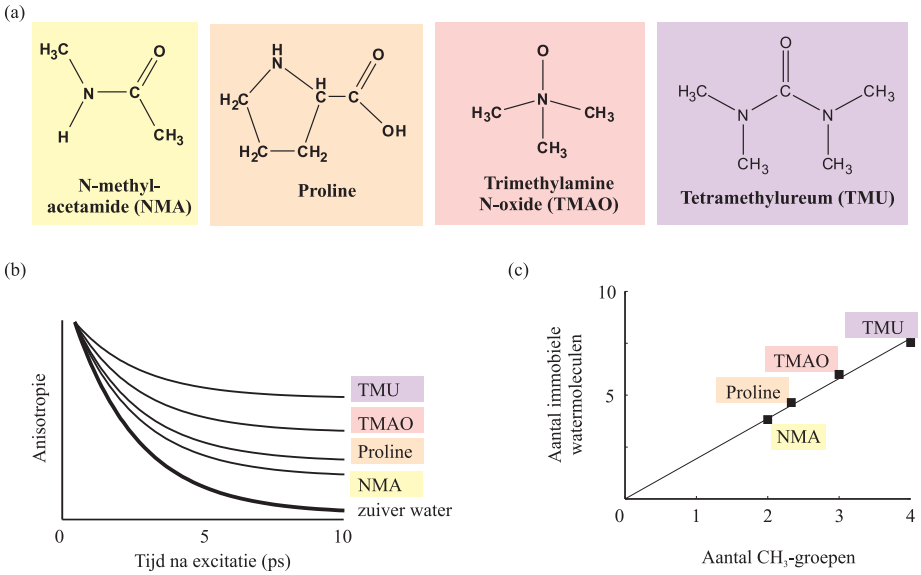

FIGUUR 4. (a) Structuurformules van de amfifiele moleculen die in het experiment gebruikt zijn. (b) We hebben het anisotropieverval van watermoleculen bepaald in een viertal oplossingen van dezelfde concentratie (5 mol per liter). In zuiver water is de reoriëntatietijd van watermoleculen 2.5 ps zoals op te maken is uit het feit dat dit de tijdsconstante is waarmee de anisotropie vervalt. In de vier oplossingen komen twee soorten watermoleculen voor: snel draaiende moleculen en langzaam draaiende moleculen. De langzaam roterende moleculen zorgen ervoor dat de anisotropie slechts gedeeltelijk vervalt tot een plateau. De hoogte van het plateau geeft het percentage immobiele watermoleculen. (c) Aantal immobiele watermoleculen per amfifiel molecuul uitgezet tegen het aantal methylgroepen in het molecuul. Proline bevat geen methylgroepen. Om het molecuul toch een plaats te geven in de grafiek hebben we gekeken naar het aantal CH-groepen. Dit zijn er 7 wat zou overeenkomen met 2.3 methylgroepen.

en olie drijft namelijk tal van biologische processen, waaronder het vouwen van eiwitten en andere biomoleculen. Begrip van de moleculaire oorsprong van deze afstoting kan daarom inzicht bieden in de manier waarop water de ruimtelijke vorm van eiwitten en DNA bepaalt.

Dankwoord

Tot slot wil ik de mensen bedanken die belangrijk zijn geweest bij de totstandkoming van dit proefschrift. Allereerst is dit natuurlijk mijn promotor Huib die mij vijf jaar lang heeft begeleid en het al die tijd met mij heeft weten uit te houden. Onze wetenschappelijke discussies waren altijd vurig; soms zelfs zo fel dat de buren de deuren moesten sluiten. In ieder geval heb ik veel van deze discussies geleerd en kijk ik met plezier terug op onze samenwerking.

Bij experimenteel onderzoek is goede technische ondersteuning onmisbaar. In bijzonder ben ik Hinco, onze groepstechnicus, dankbaar voor zijn betrokkenheid en hulp. Hinco had vaak aan een half woord genoeg om mijn technische problemen te doorgronden en deze vervolgens op adequate wijze op te lossen. Ook Rob en Henk wil ik bedanken voor hun technische ondersteuning.

Mijn groepsgenoten bedank ik voor de vriendschappelijke sfeer op AMOLF en daarbuiten. In vijf jaar tijd zijn dit er een heel aantal geweest: Frederik, Michel, Arjan, Joop, Dorte, Anne Willem, Adriaan, Bradley, Olaf, Sander, Pavel, Sergiy, Mathijs, Rutger, Lukasz, Han-Kwang, Klaas-Jan, Jocelyn, Nuria en Christian. Voor de goede sfeer ben ik ook de leden van de Bonn groep dankbaar. Dorte is degene die mij, aan het begin van mijn promotie, met veel geduld heeft ingewerkt en de geheimen van de pomp-probe spectroscopie heeft bijgebracht. Ik ben haar daarvoor veel dank verschuldigd. Rutger en Adriaan bedank ik voor het kritisch doorlezen van hoofdstuk 2. Met mijn kamergenoten Rutger en Lukasz, die altijd in waren voor een grap, heb ik vele hilarische momenten beleefd. Rutger is een meester in het maken van illustraties en ik bedank hem voor zijn hulp bij het maken van veel van de figuren uit dit proefschrift. Han-Kwang heeft geholpen bij de opmaak van dit proefschrift, bedankt daarvoor.

Het begin van mijn promotie betekende voor mij ook verhuizen naar een nieuwe stad: Amsterdam. Dat ik hier zo snel mijn draai gevonden heb, heb ik ondermeer te danken aan de vele vrienden die ik heb gemaakt bij turnvereniging Olympia.

Ik eindig dicht bij huis en bedank Pierre, Bernadette, mijn ouders en mijn lieve vriendin Elsje voor hun steun door de jaren heen.